

STUDY OF NUCLEAR STRUCTURE NEAR SHELL CLOSURE

By
SANGEETA DAS
PHYS05201504004

Saha Institute of Nuclear Physics, Kolkata

A thesis submitted to the
Board of Studies in Physical Sciences
In partial fulfilment of requirements
for the Degree of
DOCTOR OF PHILOSOPHY
of
HOMI BHABHA NATIONAL INSTITUTE

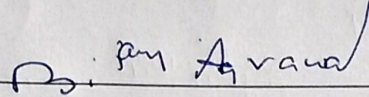


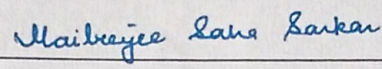
November, 2020

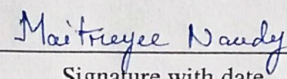
Homi Bhabha National Institute

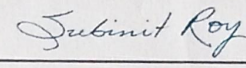
Recommendations of the Viva Voce Committee

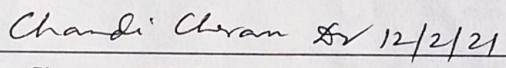
As members of the Viva Voce Committee, we certify that we have read the dissertation prepared by **Sangeeta Das** entitled "**Study of nuclear structure near shell closure**" and recommend that it may be accepted as fulfilling the thesis requirement for the award of Degree of Doctor of Philosophy.

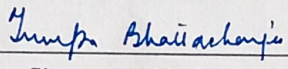
Prof. Bijay Agrawal  12.02.2021
Chairman Signature with date

Prof. Maitreyee Saha Sarkar  12/2/2021
Guide/Convener Signature with date

Prof. Maitreyee Nandy  12.02.2021
Co-guide Signature with date

Prof. Subinit Roy  12.02.2021
Member 1 Signature with date

Prof. Chandi Charan Dey  12/2/21
Member 2 Signature with date

Dr. Tumpa Bhattacharjee  12/02/2021
Member 3 Signature with date

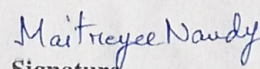
Dr. S. Muralithar  12/2/2021
External examiner Signature with date

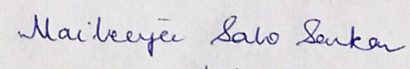
Final approval and acceptance of this thesis are contingent upon the candidate's submission of the final copies of the thesis to HBNI.

I/We hereby certify that I/we have read this thesis prepared under my/our direction and recommend that it may be accepted as fulfilling the thesis requirement.

Date: 12.02.2021

Place: Kolkata


Signature
Co-guide


Signature
Guide 12/02/2021

STATEMENT BY AUTHOR

This dissertation has been submitted in partial fulfillment of requirements for an advanced degree at Homi Bhabha National Institute (HBNI) and is deposited in the Library to be made available to borrowers under rules of the HBNI.

Brief quotations from this dissertation are allowable without special permission, provided that accurate acknowledgement of the source is made. Requests for permission for extended quotation from or reproduction of this manuscript in whole or in part may be granted by the Competent Authority of HBNI when in his or her judgement, the proposed use of the material is in the interests of scholarship. In all other instances, however, permission must be obtained from the author.

Sangeeta Das

.....
Sangeeta Das

DECLARATION

I hereby declare that the investigation presented in the thesis has been carried out by me. The work is original and has not been submitted earlier as a whole or in part for a degree/diploma at this or any other Institution / University.

Sangeeta Das
.....
Sangeeta Das

List of Publications

Journal

Published

1. “Study of radioactivity built-up and decay with singles time-stamped data”, S. Das, A. De, B. Dey, S. Sharma, A. Adhikari, S.S. Alam, A. Gupta, Y. Sapkota, A. Das, A. Saha, D. Pramanik, T. Bhattacharjee, A. Bisoi, S. Sarkar and M. Saha Sarkar, *Journal of Instrumentation*, **2019**, *14*, T09006.
2. “Decay spectroscopy of $^{117,118}\text{Sn}$ ”, Sangeeta Das, Anik Adhikari, S.S. Alam, Sathi Sharma, Suman Aich, Arkabrata Gupta, Y. Sapkota, Ananya Das, A. Saha, S. K. Dey, Dibyadyuti Pramanik, Abhijit Bisoi, Indrani Ray, Tumpa Bhattacharjee, C. C. Dey, S. Sarkar, M. Saha Sarkar, *Nuclear Physics A*, **2021**, *1006*, 122079.

Communicated

1. “Cross-shell excitation in doubly magic ^{132}Sn and its nearest neighbours”, Sangeeta Das and M. Saha Sarkar, [arXiv:2005.09411\[19-05-2020\]](https://arxiv.org/abs/2005.09411).

Others

1. “Lifetimes and transition probabilities for the low-lying states in ^{131}I and ^{132}Xe ”, S. Alam, T. Bhattacharjee, D. Banerjee, A. Saha, S. Das, M. Saha Sarkar, S. Sarkar, *Phys. Rev. C* **2018**, *99*, 014306, 1-11.

Conferences

Related to thesis

1. “Investigation of nuclear structure below the ^{132}Sn core”, S. Das, A. Bisoi, S. Sarkar, M. Saha Sarkar, *Proc. DAE-BRNS Symp. Nucl. Phys. (India)* **2015**, *60*, 108-109.
2. “Performance of low cost photodiodes in nuclear spectroscopy”, S. Das, A. Chakraborty, A. Mondal, A. Datta, S. Saha, D. Biswas, J. Panja, C. Marick, A. Mitra, S. Chatterjee, M. Saha Sarkar, *Proc. DAE-BRNS Symp. Nucl. Phys. (India)* **2015**, *60*, 978-979.
3. “Silicon PIN Diode for detection of electrons, alphas, X-rays and gamma rays”, S. Das, A. Chakraborty, A. Mondal, K. Shaw, A. Sur, S. Das, R. Laha, A. Das, J. Panja, C. Marick, A. Mitra, S. Chatterjee, M. Saha Sarkar, *Proc. DAE-BRNS Symp. Nucl. Phys. (India)* **2015**, *60*, 976-977.

4. “Shell-model studies of nuclei around $A \approx 130$ ”, S. Das, A. Bisoi, S. Sarkar, M. Saha Sarkar, Proc. DAE-BRNS Symp. Nucl. Phys. (India) **2016**, 61, 228-229.
5. “Isomers in $^{117,118}\text{Sn}$ and role of neutron $1h_{11/2}$ orbit”, S. Das, S. Sharma, S. S. Alam, A. Gupta, A. Adhikari, A. Das, A. Saha, S. K. Dey, D. Pramanik, A. Bisoi, T. Bhattacharjee, C. C. Dey, S. Sarkar, M. Saha Sarkar, Proc. DAE-BRNS Symp. Nucl. Phys. (India) **2017**, 62, 84-85.
6. “Decay spectroscopy of ^{118m}Sb ”, S. Sharma, S. Das, S. S. Alam, A. Gupta, A. Adhikari, A. Das, A. Saha, D. Pramanik, A. Bisoi, I. Ray, T. Bhattacharjee, S. Sarkar, M. Saha Sarkar, Proc. DAE-BRNS Symp. Nucl. Phys. (India) **2017**, 62, 200-201.
7. “Lifetime measurement of $3/2_1^+$ state of ^{117}Sn ”, S. Das, S. Aich, A. Adhikari, S. S. Alam, S. Sharma, B. Dey, A. Gupta, Y. Sapkota, A. Das, A. Saha, S.K. Dey, D. Pramanik, D. Banerjee, T. Bhattacharjee, C. C. Dey, A. Bisoi, S. Sarkar, M. Saha Sarkar, Proc. DAE-BRNS Symp. Nucl. Phys. (India) **2018**, 63, 270-271.
8. “Singles time stamped data in In-beam spectroscopy”, S. Das, A. De , B. Dey, S. Sharma, A. Adhikari, S. S. Alam, A. Gupta, Y. Sapkota, A. Das, A. Saha, D. Pramanik, D. Banerjee, T. Bhattacharjee, A. Bisoi, S. Sarkar, M. Saha Sarkar, Proc. DAE-BRNS Symp. Nucl. Phys. (India) **2018**, 63, 1144-1145.
9. “Shell model study of ^{118}Sn with excitations across $N=82$ shell gap”, S. Das, M. Saha Sarkar, Proc. DAE-BRNS Symp. Nucl. Phys. (India) **2019**, 64, 70-71.
10. “Estimation of Relative Cross-Sections from Activation Analysis”, K. Pradhan, S. Das, S. Sharma, D. Chattopadhyay, I. Ray, M. Saha Sarkar, Proc. DAE-BRNS Symp. Nucl. Phys. (India) **2019**, 64, 198-199.
11. “Coincidence Study between internal conversion electrons and γ -rays in ^{152}Eu ”, S. Das, S. Sharma, S. De, M. Saha Sarkar, (Proc. DAE-BRNS Symp. Nucl. Phys. (India) **2019**, 64, 988-989.

Others

1. “Spectroscopy of low lying states of $^{132,134}\text{Xe}$ from beta Decay”, R. Banik, S. Bhattacharyya, S. Bhattacharya, D. Banerjee, S.K. Das, R. Guin, G. Mukherjee, S. Das, T. Bhattacharjee, A. Choudhury, P. Das, A. Saha, Proc. DAE-BRNS Symp. Nucl. Phys. (India) **2016**, 61, 76-77.
2. “Characterization of NaI (Tl) Sum Spectrometer and its utilization”, M. Saha Sarkar, A. Gupta, S. Das, S. Datta, T. Mitra, I. Ray, Y. Sapkota, J. Panja, S. Chatterjee, A. Mitra, Proc. DAE-BRNS Symp. Nucl. Phys. (India) **2016**, 61, 1022-1023.

3. "Proton induced reactions of ^{27}Al at low energies", S. Sharma, A. Gupta, S. Das, A. Adhikari, Y. Sapkota, A. Das, R. Paul, D. Pramanik, A. Bisoi, S. Sarkar, M. Saha Sarkar, Proc. DAE-BRNS Symp. Nucl. Phys. (India) **2017**, 62, 280-281.
4. "Lifetime measurement of low lying states of ^{27}Si ", S. Sharma, S. Das, A. De, R. Gupta, A. Gupta, A. Adhikari, A. Das, Y. Sapkota, A. Saha, S. S. Alam, S. Bhattacharya, R. Banik, S. Nandi, S. Das, S. Samanta, S. Chatterjee, S. Bhattacharyya, B. Dey, D. Pramanik, A. Bisoi, T. Bhattacharjee, M. Nandy, S. Sarkar, M. Saha Sarkar, Proc. DAE-BRNS Symp. Nucl. Phys. (India) **2018**, 63, 320-321.
5. "Life-time Measurement of levels in $^{160-162}\text{Dy}$ nuclei", A. Adhikari, S. Das, S.S. Alam, D. Pramanik, S. Sharma, Y. Sapkota, A. Gupta, A. Das, A. Saha, D. Banerjee, T. Bhattacharjee, A. Bisoi, M. Saha Sarkar, S. Sarkar, Proc. DAE-BRNS Symp. Nucl. Phys. (India) **2018**, 63, 338-339.
6. "Spectroscopy of $^{160,161}\text{Ho}$ ", A. Adhikari, D. Pramanik, S. Das, A. Gupta, Y. Sapkota, A. Das, S. Sharma, A. De, A. Saha, S. S. Alam, S. Das, S. Samanta, S. Chatterjee, S. Bhattacharya, R. Banik, S. Nandi, R. Raut, S.S. Ghugre, S. Bhattacharyya, G. Mukherjee, T. Bhattacharjee, A. Bisoi, M. Saha Sarkar, S. Sarkar, Proc. DAE-BRNS Symp. Nucl. Phys. (India) **2018**, 63, 332-333.
7. "Study of nuclear structure in ^{125}I ", S. S. Alam, D. Banerjee, T. Bhattacharjee, A. Saha, S. W. Raja, S. Das, A. Adhikari, A. De, A. Gupta, A. Das, Y. Sapkota, S. Sharma, S. Dey Chaudhuri, D. Pramanik, A. Bisoi, M. Saha Sarkar, S. Sarkar, Proc. DAE-BRNS Symp. Nucl. Phys. (India) **2018**, 63, 356-357.
8. "Preparation and Characterization of Implanted Targets of ^{16}O and ^{24}Mg for Nuclear Astrophysics experiments", A. Gupta, D. Devi Ksh., G R Umapathy, S. Ojha, S. Sharma, S. Das, A. Parihari, Md. M. Shaikh, A. Bisoi, S. Sarkar, M. Saha Sarkar, Proc. DAE-BRNS Symp. Nucl. Phys. (India) **2018**, 63, 1076-1077.
9. "Measurement of gamma radiation background in a low energy accelerator facility", S. Sharma, S. Das, A. De, S. Ray, P. Das, H. Rattan, M. Saha Sarkar, Proc. DAE-BRNS Symp. Nucl. Phys. (India) **2018**, 63, 1090-1091.
10. "VECC-INGA: An exploration of nuclear structure with light ions", S. Bhattacharya, R. Banik, S. Nandi, Sajad Ali, S. Chatterjee, S. Das, S. Samanta, K. Basu, A. Choudhury, A. Adhikari, S. S. Alam, Shabir Dar, B. Das, S. Das, A. Dhal, A. Mondal, K. Mondal, P. Mukhopadhyay, H. Pai, P. Ray, A. Saha, I. Shaik, C. Bhattacharya, G. Mukherjee, R. Raut, S. S. Ghugre, A. Goswami, S. Bhattacharyya, Proc. DAE-BRNS Symp. Nucl. Phys. (India) **2018**, 63,

1156-1157.

11. “Study of $^{24}\text{Mg}(p,\gamma)^{25}\text{Al}$ resonance reaction at lab energy $E = 223$ keV”, A. Gupta, S. Sharma, S. Das, A. Adhikari, A. Mondal, M. Roy Chowdhury, C. D Bagdia, L. Trivedi, V. Nanal, A. Bisoi, M. Saha Sarkar, S. Sarkar, Proc. DAE-BRNS Symp. Nucl. Phys. (India) **2019**, 64, 984-985.
12. “Study of $^{14}\text{N}(p,\gamma)^{15}\text{O}$ resonance reaction at $E_{lab}^p = 278$ keV, S. Sharma, A. Gupta, S. Das, M. Roy Chowdhury, A. Mandal, A. Bisoi, V. Nanal, L.C. Tribedi, S. Sarkar, M. Saha Sarkar, EPJ Web of Conferences **2020**, 227, 02011, 1-4.

Sangeeta Das
.....
Sangeeta Das

Dedicated to my loving Family...

'Ma', 'Baba', 'Dada', 'Boudi', 'chotto Ittu'

ACKNOWLEDGEMENTS

This academic venture could not be accomplished without the help of many people. I would like to express my gratitude to each and every person, whom I came across during the last five years.

First of all, I would like to express my sincere gratitude to my supervisor Prof. Maitreyee Saha Sarkar for providing the necessary support and fruitful suggestions throughout the period. I am thankful to her for her constant motivation and positive outlook in every scenario. Her critical assessment, profound knowledge and enthusiasm have helped me to sharpen my abilities in all aspects.

I am thankful to my co-supervisor Prof. Maitreyee Nandy for help and support during this journey. I would like to acknowledge all the members of the Doctoral Committee for assessing my research work and providing useful suggestions to shape my work. I take this opportunity to thank all the members of Nuclear Physics Division, SINP for their help and support. I also want to acknowledge Prof. Sukalayan Chattopadhyay for support.

Many thanks to Prof. Sukhendusekhar Sarkar (IEST) and to Prof. Ranjan Bhowmik (IEST) for developing interest of Nuclear physics in me during M.Sc days. I am grateful to Prof. Sarkar for making me familiar with the beautiful world of nuclear physics.

I would like to thank Dr. Tumpa Bhattacharyya (VECC) for providing the support during the experiments which are crucially related to my doctoral

study. The fruitful discussion-sessions with her on the experimental procedures and data analysis have helped me a lot to progress in the experimental arena. Special thanks due to Dr. Debasish Banerjee for helping in the irradiation experiments.

I grab this chance to thank Prof. Satyajit Saha, Prof. Chandicharan Dey and Prof. Subinit Roy for allowing me to use their radioactive sources, detectors, other experimental tools, which are inseparable parts of my study. My sincere gratitude to Prof. Supratic Chakroborty and Dr. Debaleen Biswas for the help in the photodiode project. Special thanks to Ms. Dibyashree Choudhury, CSD, for providing help in the preparation of target.

I want to thank specially Mrs. Jonaki Panja and Mr. Chandranath Marick for the invaluable scientific help in my photodiode project. I would also acknowledge Mr. Sujib Chatterjee and Mr. Pradipta Das for their constant help during the experiments. A big thank goes to Mr. Pradip Barua for helping in all sort of problems always. Special thanks due to Mr. Suraj Karan for his technical help in laboratory.

Sincere thanks to my seniors AbhijitDa, DibyadyutiDi, BalaramDa, IndraniDi, SudattaDi, AnisurDa, SubhenduDa for their valuable suggestions. I am extremely thankful to SafikulDa, Anik, Sathi for their support during different stages of my work. I must acknowledge our experiment group members, Arka, Yajnya, Ananya, ArunabhaDa for their help during the experiments. My sincere thanks to Mr. Arkojyoti De and Mr. Suman Aich for

their help in my work. I must thank all the summer project students (Arghya Chakraborty, Anshuman Mondal, Kushal Shaw, Ankan Sur, Satadal Das, Arya Datta, Sourayadeep Saha, Shruti De, Rajrupa Mondal), who helped me a lot in the photodiode project. I would like to convey thanks to my PMSc. batch-mates, especially to Arpita. I thank all the members of 3304, Sajad, Prithwijita, Piyasi, Ashok, Dipali, Tanmay, Saikat, Lalit and Amrita for making this journey enjoyable.

Words will never be enough to acknowledge the support from 'Baba', 'Ma', 'Dada' and 'Boudi'. Thank you for being the best family I could ever ask for. Boundless love to my 'chotto ittu' for brightening up my life. My sincere gratitude to Late Sabita Maji, my 'Masi' for teaching me and getting me interested in academics. My warmest appreciation goes to Sourav for the immense patience, encouragement, timely advice and support through these years. I take this opportunity to thank my friends, Suchetana, Zaineb, Tiyasa, Anindita, Saswati for their love and support.

I sincerely apologise for unintentional omission of any name.

Contents

Summary	xix
List of Figures	xxi
List of Tables	xxii
1 Introduction	1
1.1 Aim of the thesis	4
1.1.1 Structure of thesis	6
2 Decay spectroscopy of Sn isotopes	7
2.1 Introduction	7
2.2 Interesting features of this region	8
2.3 Experimental details	9
2.3.1 Irradiation experimental details:	11
2.3.2 Setup I utilizing analog Data acquisition system	13

2.3.3	Setup II utilizing Digital Data acquisition system . . .	16
2.4	Results	16
2.4.1	Decay half-life measurement of parent nucleus from singles data	16
2.4.1.1	Decay half-life of ^{118m}Sb	16
2.4.1.2	Decay half-life of ^{117g}Sb	17
2.4.2	Excitation energy and Level structure : ^{118}Sn	18
2.4.2.1	984 keV:	20
2.4.2.2	The unplaced γ -transition:	23
2.4.2.3	Relative Intensities and Feeding Pattern: ^{118}Sn from ^{118m}Sb	24
2.4.3	Level lifetime measurement	26
2.4.3.1	Result of ^{118}Sn	29
2.4.3.2	Result of ^{117}Sn	31
	2.4.3.2.1 Setup 1: Measurement with $\text{LaBr}_3(\text{Ce})$ and BaF_2 scintillators:	32
	2.4.3.2.2 Setup 2: Measurement with VEN- TURE array:	34
2.5	Theoretical interpretation: Shell model calculations	41
2.5.1	Model space and interaction	42

2.5.2	Truncation schemes	42
2.5.3	Results and Discussions	43
2.6	Summary	44
3	Development of analysis method of digital data	47
3.1	Introduction	47
3.2	Digital Electronics	49
3.3	Experimental Details	50
3.4	Methodology	51
3.5	Data analysis procedure	54
3.5.1	Details about the data sorting program	54
3.6	Specific experiment details	56
3.6.1	Offline experiment:	56
3.6.1.1	^{118m}Sb : 8^- state	57
3.6.1.1.1	Discussion	57
3.6.1.2	^{117g}Sb : $5/2^+$ state	59
3.6.2	In-beam experiment:	60
3.7	Discussion	64
4	Detector development and characterisation	67
4.1	Introduction	67

4.2	Photodiodes used in the present project	70
4.3	Characteristics of photodiodes and PIN diodes used	70
4.3.1	Capacitance	70
4.3.2	Dark Current	72
4.4	Other essential details and electronics	73
4.4.1	Mounting of the detector	73
4.4.2	Preamplifier	73
4.4.3	Cooling the detector	76
4.4.3.1	Liquid N ₂ cooling arrangements	76
4.4.3.2	Development of cooling device: Using Thermoelectric cooler	78
4.5	Detection of nuclear radiation	80
4.5.1	Detection of alpha particles	80
4.5.1.1	BPW21	82
4.5.1.2	BEL Si-PIN diode	83
4.5.2	Detection of X-rays, gamma rays and conversion electrons	85
4.5.2.1	Identifying electron and X-ray peaks in the spectrum	86

4.5.2.2	Gamma-ray detection using cooling arrangement	87
4.5.2.3	Coincidence study between conversion electrons and γ -rays in ^{152}Eu	88
5	Theoretical study for Sn isotopes	93
5.1	Introduction	93
5.2	Motivation	94
5.3	Model space and effective interactions	95
5.3.1	The effective interactions used	95
5.3.1.1	The sn100pn interaction	95
5.3.1.2	The Bonnnewpn interaction	96
5.3.1.3	Bonnsn interaction	97
5.3.2	Reviewing the SPEs and TBMEs	97
5.3.2.1	Neutron single-particle energies	98
5.3.2.2	Proton single-particle energies	99
5.3.2.3	Neutron-neutron two body matrix elements (TBME)	100
5.3.2.4	Proton-proton two body matrix elements (TBME)	101
5.3.3	Neutron-proton two body matrix elements (TBME) . .	102

5.4	Isomers in even and odd Sn isotopes	103
5.4.1	Calculations and Results	104
6	Cross-shell excitation near ^{132}Sn	117
6.1	Introduction	117
6.2	Motivation of this work	119
6.3	Formalism	120
6.3.1	Model space and choice of single particle energies (spe)	120
6.3.2	The two body matrix elements (tbme)	122
6.3.2.1	Calculation using Delta interaction	123
6.3.2.2	Tuning of cross-shell $\nu - \nu$ tbme	124
6.3.2.3	Tuning of inter-shell tbmes	128
6.3.2.4	The center of mass correction	128
6.3.3	The interactions	130
6.4	The calculation I: Excitation spectra of ^{132}Sn and its neighbour	130
6.5	Results and Discussion - I	131
6.5.1	Binding Energies	131
6.5.2	Excitation Energies	132
6.5.2.1	$^{132}_{50}\text{Sn}_{82}$	132
6.5.2.2	$^{133}_{51}\text{Sb}_{82}$	135

6.5.2.3	$^{134}_{52}\text{Te}_{82}$	137
6.5.2.4	$^{135}_{53}\text{I}_{82}$	139
6.5.2.5	$^{131}_{50}\text{Sn}_{81}$	141
6.5.2.6	$^{132}_{51}\text{Sb}_{81}$	143
6.5.2.7	$^{133}_{52}\text{Te}_{81}$	145
6.5.2.8	$^{134}_{51}\text{Sb}_{83}$	148
6.5.2.9	$^{135}_{52}\text{Te}_{83}$	149
6.5.3	Transition Probabilities in ^{132}Sn and its neighbours	151
6.5.3.1	Effective charges	152
6.5.3.2	Comparison with experimental data	153
6.6	The calculation II: Determination of $B(E1:5^{-}_1 \rightarrow 4^{+}_1)$ of Sn isotopes	155
6.7	Results and Discussion - II	157
7	Summary and future outlook	159
A	Activation analysis	163
B	Gamma decay and Internal conversion	165
B.1	Gamma decay	165
B.2	Internal conversion	166

C Measurement of lifetime from time difference spectrum **169**

Bibliography **171**

List of Figures

2.1	Variations of experimental half-lives and excitation energies ([18]) of first $11/2^-$ state of odd A isotopes of Cd ($Z = 48$), Sn ($Z = 50$) and Te ($Z = 52$).	10
2.2	Variation of experimental energies and half-lives [18] of (5_1^- and 7_1^-) isomer in even A isotopes.	10
2.3	The schematic diagram [24]) of the different beamlines of $K = 130$ cyclotron. We have performed the irradiation experiment in channel 1.	11
2.4	(a) The collimator, target holder, and the Faraday cup as indicated in the picture constitute the irradiation flange. (b) The flange position and the direction of the beam along with the beamline are marked in the picture.	12
2.5	Experimental setup I is shown indicating the positions of detectors and the source stand. The distance between each Clover and the source stand is 5 cm.	14
2.6	The decay curve of parent nucleus ^{118}Sb , monitoring different γ -transitions of ^{118}Sn , as function of decay time utilizing the setup I.	17
2.7	Left : The population of 158 keV state ($3/2^+$ state of ^{117}Sn) from ^{117m}Sb ($5/2^+$ state) and ^{117m}Sn IT decay is shown in figure. Right : The decay curve of ^{117}Sb following the time evolution of 158 keV γ -transition from experimental setup I.	18

2.8	The decay scheme of ^{118}Sn via E.C. decay from 8^- state of ^{118}Sb . The 40 keV transition (coming from 5^- state to 4^+) is not mentioned because of closed spacing. Fig. (a) Adopted in NNDC, Fig. (b) decay scheme presented by Rahmouni <i>et al.</i> [16]. Red transitions are unplaced gammas that are not adopted in NNDC. Fig. (c) The decay scheme proposed from present work. Level energies and gamma transitions are expressed in keV.	19
2.9	Spectra gated by different strong γ -rays (253 keV, 1050 keV, 1229 keV) are shown. The γ -transitions confirmed in the present work and also included in the adopted decay scheme [18] are marked (blue colored). Energies of the unplaced [18] and new γ -rays are written in red-colored fonts.	21
2.10	The gated spectrum of 984 keV transition. In inset, it is compared with the normalised total projection spectrum of Clover detector.	22
2.11	The E_γ - E_γ matrix is shown. The Compton lines ($E_{\gamma_1} + E_{\gamma_2} = E_\gamma$) corresponding to $E_\gamma = 1229$ keV and 2615 keV are indicated. The vertical and horizontal lines corresponding to correlated photopeaks of 253 keV, 1050 keV and 1229 keV are also marked.	22
2.12	The gated spectra of new or unplaced transitions are shown.	25
2.13	Projection of TAC spectrum gating 25 keV in one Clover detector and 253 keV in the another (in log scale). The TAC spectrum has been compared with prompt distribution (normalised) obtained by gating 25 keV and 158 keV in the detectors.	29
2.14	Projection of TAC spectrum gating 253 keV in one Clover detector and 1229 keV in the another. In the inset, the TAC spectrum is compared with prompt distribution (normalised) gating after region 253 keV and 1229 keV in the detector.	30

2.15	The prompt TAC spectrum of ^{22}Na obtained by gating 154-160 keV in both detectors of set up I. The TAC spectrum is fitted with two different Gaussian distributions. The fitted left-side is shown in topmost left and right side is shown in topmost right part. In bottom, the asymmetrical prompt curve is fitted with the Gaussian distributions having different parameters for two sides.	34
2.16	The time-delayed spectrum of ^{117}Sn is fitted with convoluted function. In inset, comparison of the prompt (^{22}Na) and delayed (^{117}Sn) TAC spectra is shown.	35
2.17	Fig. (a) The setup of VENTURE array with six CeBr_3 detectors is shown. (b) The schematic diagram of electronics used for timing signal processing. The set up is identical to Ref. [45] except for the number of detectors.	35
2.18	(Left) Two dimensional E_γ - E_γ matrix is generated from the data collected using six CeBr_3 detector. (Right) The total projected spectrum obtained from the matrix is shown. The gated spectra are obtained by gating Xray and 158 keV peaks.	36
2.19	Two different matrices are constructed under two different conditions : (a) Time difference (TAC) vs. $E_{\gamma 1}$ matrix is build up by gating 158 keV in $E_{\gamma 2}$ and (b) vice versa. Different projected regions are also shown in the figure.	38
2.20	(a) The prompt TAC curve is generated by gating after region of 158 keV and it is fitted with a Gaussian distribution [shown by red curve]. (b) Delayed TAC curve is built up by gating 158 keV in both the detector. It is fitted with a Gaussian distribution function fixing the same width parameter obtained from the fitted prompt spectrum.	39

2.21	Fig. (a) shows delayed TAC curve, that is built up by gating 158 keV in both the detectors. Fig. (b) 158 keV-158 keV TAC is modified by substituting the left part by the prompt Gaussian distribution obtained from Fig. 2.20 (b). It is fitted with exponentially modified Gaussian distribution.	41
3.1	Schematic flow chart of data sorting program.	55
3.2	Typical gamma spectrum of irradiated natural Indium by 32 MeV α -beam collected using HPGe detector.	57
3.3	(Left) Growth curves of daughter nucleus for different intense γ -transitions. (Right) Decay of parent nucleus is followed to evaluate decay half-life. In Inset $\ln(\text{count rate})$ are shown. The spectra are generated time with 3M event bin.	58
3.4	Same as Fig. 3.3. The spectra are generated with 1M event bin.	58
3.5	The decay curve of ^{117}Sb following the time evolution of 158 keV γ -transition from the digital data acquired by CAEN 5780 Digitiser.	60
3.6	Typical in-beam and decay spectra of natural Zn target bombarded by 10 MeV proton projectile.	62
3.7	Variation of peak area of different γ -transitions with time. The dash-dotted line differentiates between the beam-on and beam-off situations. The inset shows a zoom-in of transition time.	63
3.8	Growth curves of Zn isotopes ($^{64,66,68}\text{Zn}$) generated from decay gamma rays of corresponding radioactive Ga isotopes	65

4.1	(Top) Left: The variation of projected range is plotted with alpha energy [56]. Right: The variation of absorption depth with the electron energy is presented. The plot has been taken from Ref. [57]. (Bottom) The variation of attenuation length is plotted with X-ray energy calculated from Ref. [58].)	68
4.2	The pictures of different diode detectors [(a) BPW24, (b) BPW21, (c) VTB8440BH, (d) BEL Si(PIN) diode] are shown along with their specification details provided by the manufacturer.	71
4.3	Variation of capacitance with varying reverse voltage for different diode detectors measured using Agilent LCR meter.	71
4.4	The spectra of ¹³³ Ba are compared for two different leakage current of BEL-Si(PIN) diode.	72
4.5	The schematic diagram of preamplifier circuit following circuit provided in Ref. [66].	74
4.6	The pulses of (a) laser light, (b) alpha source ²⁴¹ Am are processed using the preamplifier fabricated in a breadboard.	75
4.7	Different parts of the cooling arrangement using liquid N ₂ are shown in the figure.	77
4.8	The variation of leakage current of BEL-Si(PIN) diode is plotted with decreasing temperature.	77
4.9	Different arrangements using TEC are shown along with the schematic diagram.	79
4.10	The spectrum is acquired (a) without / (b) with using the TEC using water-cooling arrangement. The noise level reduces by a significant amount using the water-cooled TEC arrangement.	80
4.11	The block diagram of the experimental setup used in the alpha particle detection experiment.	81

4.12	The preamp pulses of different diode detectors, such as (a) BPW21, (b) BEL-Si (PIN), (c) VTB8440BH are displayed. The experimental conditions are also mentioned.	82
4.13	(Left) The alpha spectra are obtained by BPW21 detector using triple line alpha sources for different shaping times of spectroscopic amplifier. (Right) The alpha spectra for amplifier shaping time 10 μ s.	83
4.14	(Left) The alpha spectra are obtained by BEL-Si (PIN) diode detector using triple-line alpha source to set optimum shaping time of spectroscopic amplifier. The inset shows the alpha spectrum having the best resolution obtained for 3 μ s. (Right) The alpha spectra are compared for single -line and triple -line sources under the same experimental condition.	84
4.15	The effect of reverse bias is shown in figure using two different radioactive sources: (a) ^{241}Am and (b) ^{152}Eu	85
4.16	The X-ray - conversion electron spectra of ^{152}Eu is compared with increasing thickness of protective layer (plastic) around the source mentioned in legend.	87
4.17	The spectra are obtained using standard radioactive sources of ^{133}Ba at different reverse voltages applied on BEL Si(PIN) diode.	88
4.18	(a) The setup for the measurement of internal conversion coefficient. (b) The zoomed view of the setup with PIN diode cooled with TEC using by water-cooling arrangement. . . .	89

4.19	(a) The two dimensional energy matrix constructed from coincidence data using <i>LAMPS</i> software is represented. The X axis corresponds to the energy spectrum of gamma transitions detected by NaI(Tl). The Y axis represents the electron energy spectrum obtained using Si(PIN) diode. (b) The total projection of gamma spectrum is shown (green colour) indicating the peaks of ^{152}Eu . (c) The internal conversion spectrum is illustrated showing the energy of the peaks.	90
4.20	(a) A simplified decay scheme of ^{152}Eu is shown in the figure [76]. Approximate energies are presented in keV. (b) The gated spectra is represented. The spectra in blue colour are the projected electron spectra gating the specified gamma transition indicated in box. The spectrum in green colour is the projected gamma spectrum gating 115 keV electron peak.	91
5.1	The excitation energies of this enlisted nuclei are calculated to understand different ingredients of the effective interaction.	98
5.2	The theoretically calculated excitation energies of ^{101}Sn (left panel) and ^{131}Sn (right panel) are shown using different interactions. The experimental data [18] are also plotted wherever available.	99
5.3	The theoretically calculated excitation energies of ^{101}Sb (left panel) and ^{133}Sb (right panel) are shown using different interactions. The experimental data [18] are also compared wherever present.	100
5.4	The theoretically calculated excitation energies of ^{102}Sn (left panel) and ^{130}Sn (right panel) are shown using different interactions. The experimental data [18] are also plotted wherever available.	101

5.5	The theoretically calculated excitation energies of ^{102}Te (left panel) and ^{134}Te (right panel) are shown using different interactions. The experimental data [18] are also plotted wherever available.	102
5.6	The theoretically calculated excitation energies of ^{102}Sb (left panel) and ^{132}Sb (right panel) are shown using different interactions. The experimental data [18] are also plotted wherever available.	103
5.7	The variation of excitation energy and half-lives of different isomers observed in even (left panel) and odd (right panel) isotopes of Sn are shown. Data are taken from Refs. [18, 21, 84–86]. The half-lives of 5^- and 7^- states of ^{118}Sn have been determined in the present work.	104
5.8	Comparison of experimental and calculated (two interactions : sn100pn and Bonnnewpn) excitation spectra of $^{124,126,128,130}\text{Sn}$. Experimental data are obtained from Ref. [18]. . .	106
5.9	Comparison of experimental and calculated (two interactions : sn100pn and Bonnnewpn) excitation spectra of $^{125,127,129}\text{Sn}$. Experimental data extracted from Ref. [18]. . . .	107
5.10	The level energies of different isomeric states are shown. The experimental levels (star symbol) are compared with theoretical energies using sn100pn (circle symbol) and Bonnnewpn interaction (up triangle). The left panel shows the excitation energies of 5^- isomeric states of even isotopes and $19/2^+$ states for odd isotopes. The right panel indicates the excitation energies of 7^- isomeric states of even isotopes and $23/2^+$ states for odd isotopes. . . .	108
5.11	The level energies of different isomeric states are shown systematically. The experimental levels (star symbol) are compared with theoretical energies using sn100pn interaction (circle symbol) and Bonnnewpn interaction (up triangle).	110

5.12	The experimental reduced transition probabilities, $B(E2)$ are compared with theoretical results. The calculations are performed for two different effective charges such as $e_n = 0.50e$ and $0.85e$ for both interactions, $sn100pn$ and $Bonnnewpn$. The results are given for $7^- \rightarrow 5^-$ state for even isotopes (left panel) and $23/2^+ \rightarrow 19/2^+$ state for odd isotopes (right panel).	112
5.13	The experimental reduced transition probabilities, $B(E2)$ are compared with theoretical results. The calculations are performed for two different effective charges such as $e_n = 0.50e$ and $0.85e$ for both interactions, $sn100pn$ and $Bonnnewpn$. The results are given for $15^- \rightarrow 13^-$ state for even isotopes (left panel) and $19/2^+ \rightarrow 15/2^+$ state for odd isotopes (right panel).	114
5.14	Same as Fig.5.12. Here, the results are plotted for $10^+ \rightarrow 8^-$ state for even isotopes (left panel) and $27/2^- \rightarrow 23/2^-$ state for odd isotopes (right panel).	114
5.15	The theoretically calculated magnetic moments are compared with the experimental results [91].	115
6.1	The empirical interaction energy between two nucleons is plotted. One of them is in $1h_{11/2}$ orbit and the other in $2f_{7/2}$ orbit. The CWG (sm56: present) $\pi - \nu$ ($\nu - \nu$) interaction. The dashed (solid) line indicates the monopole energy for CWG (sm56: present) interaction.	127
6.2	The list of nuclei for which theoretical calculations have been done. The maximum $\nu\pi\nu$ excitation mode which was computationally possible in the present calculation has been indicated in the chart.	131
6.3	Comparison of theoretically calculated and experimental binding energies with respect to ^{132}Sn .	132

6.4	Comparison of (a) positive parity and (b) negative parity states in the experimental spectra of ^{132}Sn with theory with 3p3h excitations. The results with <i>sm56fp</i> are shown with filled blue bullets and those with <i>sm56fph</i> are indicated with open blue bullets. The number of asterisks (N) appearing as superscript in the value of angular momentum in the x-axis label indicate it as the (N+1)th state of that spin.	134
6.5	Comparison of experimental spectra of high spin states in ^{133}Sb with theory. More details are included in the legend, caption of Fig. 6.4 and the text.	136
6.6	Comparison of experimental spectra of ^{134}Te with theory.	138
6.7	Comparison of experimental spectra of ^{135}I with theory.	140
6.8	Comparison of experimental spectra of ^{131}Sn with theory.	143
6.9	Comparison of experimental spectra of ^{132}Sb with theory.	145
6.10	Comparison of experimental spectra of ^{133}Te with theory.	146
6.11	Comparison of experimental spectra of ^{134}Sb with theory.	147
6.12	Comparison of experimental spectra of ^{135}Te with theory.	152
A.1	Schematic figure of activity building and decaying of daughter nucleus during the irradiation and after the irradiation.	164
B.1	The internal conversion coefficient is plotted with increasing energy for Sn element. It is calculated theoretically using BRICC code [74].	168
C.1	A typical gamma ray spectrum indicating photopeaks and their neighbouring background.	169

C.2 These four spectra illustrate the regions in which the photo-peaks or their backgrounds are selected as gating region. The gating regions have been specified in each of the spectrum.

CHAPTER 1

Introduction

The presence of shell-closure and discovery of magic numbers (2, 8, 20, 28, 50, 82, 126) at the shell closure of atomic nuclei, prescribed by Goeppert-Mayer and Jensen in 1940s [1, 2], are key achievements in nuclear structure physics. The structural feature near the doubly magic shell has enormous importance. The long isotopic chain between two doubly magic nuclei ^{100}Sn and ^{132}Sn has grabbed a special interest both from experimental and in theoretical view. This chain of isotopes having eight stable isotopes ($^{114-120}\text{Sn}$, ^{122}Sn) provides insight to explore the change in nucleon-nucleon interaction starting from proton-rich nuclei near ^{100}Sn ($N \sim Z$ and $N/Z \sim 1$) to neutron-rich nuclei near ^{132}Sn ($N - Z \sim 32$ and $N/Z \sim 1.64$) via the line of stability.

In this current doctoral thesis, the experimental as well as theoretical investigation of the nuclear structure of Sn (Tin) isotopes between two doubly magic nuclei ^{100}Sn and ^{132}Sn and their neighbours have been explored. With the progression in experimental and theoretical tools, the available spectroscopic data of the most neutron-deficient $N = 50$ isotope till neutron-rich isotopes with $N =$

82-88 are useful to analyse different basic concepts of nuclear physics. Therefore, this particular series can be a fertile ground to investigate the evolution of nuclear interaction with increasing neutron numbers. This whole chain can be partitioned into few groups such as,

- neutron deficient ones near ^{100}Sn (near proton drip line),
- isotopes at the mid-shell with $N \simeq 64$ (on and close to the line of stability),
and,
- the neutron-rich and exotic isotopes (near to neutron drip line).

Each of these groups has distinctive features of its own. The experimental methods to populate these different groups also vary widely. Fusion evaporation reaction is an appropriate technique to populate these nuclei. However, being far away from stability, the low production rate is crucial for these experiments. The nuclei around the mid-shell can be produced using the heavy-ion fusion evaporation reaction. However, with increasing neutron numbers, relatively lighter projectile-induced fusion reaction and Coulomb excitation methods are more effective methods to study them. Heavier Sn isotopes, after $A > 122$, are difficult to populate using standard fusion-evaporation reaction due to lack of proper stable projectile and target combination. The neutron-rich species, closer to the neutron drip line, can only be populated through fission or fragmentation reactions.

The vital physics issues for these groups reveal different aspects of nuclear structure. In the proton-rich region, ^{100}Sn is predicted to be the heaviest self-

conjugate doubly magic core. It lies in the proton drip line's vicinity and has been populated experimentally [3, 4]. This nucleus is bound by ~ 3 MeV against the proton emission [5]. Since this region resides near the $N=Z$ line, the protons and the neutrons occupy identical orbitals. This feature brings the opportunity to study the pairing relation between the proton and neutron. In the neutron-deficient region, there is an ambiguity in the assignment of the ground state spin of Sn isotopes due to the near degenerate energies of the neutron $1g_{7/2}$ and $2d_{5/2}$ orbits outside the ^{100}Sn core. From the conventional shell model, it was expected that, at least, the ground states of $^{101-105}\text{Sn}$ must be identical, and the spin value will be either $J^\pi = 5/2^+$ or $7/2^+$ depending on the lowest single-particle orbital spin. It is observed that for $^{101,103-109}\text{Sn}$, $5/2^+$ is the ground state spin [6]. However, in a later experiment [7], the ground state of ^{101}Sn has been reported as $7/2^+$. The ambiguous ordering of $\nu 1g_{7/2}$ - $\nu 2d_{5/2}$ orbits needs a more detailed spectroscopic study to be resolved.

One of the most exciting topics for the chain of Sn isotopes is the study of the evolution of $B(E2, 0^+_{g.s} \rightarrow 2^+_1)$ values with increasing neutron number from ^{100}Sn . For semi-magic nuclei, according to the generalized seniority scheme, it is expected that the excitation energy of 2^+_1 should have a constant value, and the transition rate will exhibit a parabolic feature showing a maximum at mid-shell. The excitation energy of the 2^+_1 states ($\simeq 1.2$ MeV) and the transition rates in the neutron-rich side of Sn isotopes follow the theoretical predictions well. Experimentally, a local minimum is observed at $A = 116$ i.e. at mid-shell, showing higher values than predicted values for $^{112,114}\text{Sn}$ [8, 9]. A few

theoretical calculations are performed, which can interpret part of the features of experimental data successfully [10]. For more neutron-rich Sn isotopes beyond $N=82$, a sudden depression in 2_1^+ energy ($E(2_1^+)$ for $^{134}\text{Sn} = 0.726$ keV) is observed [11]. Comparison with the systematics of 2_1^+ energies of other n-rich domains and the spin-tensor decomposition of the two interactions establish the prediction for a new shell closure at ^{140}Sn . The anomalously depressed 2_1^+ states in Sn isotopes having $N = 84-88$ and the new shell closure for $N = 90$ might have interesting consequences for the r-process nucleosynthesis [12–14].

1.1 Aim of the thesis

With the advent of technology, most recent nuclear spectroscopic studies are intended to extend to the extremes of angular momentum, energy, and isospin. However, to have complete information about nuclear structure over the entire nuclear chart from stability to drip lines, the existing knowledge of the low-spin structure of nuclei on and near the valley of stability needs to be refined further. Although the features observed in two extreme sides of the isotopic chain near the two drip lines are more demanding and reveal interesting physical phenomena, the mid-shell also offers different intriguing facts. The low energy spectra of these nuclei are generally accessed through decay-spectroscopy. For mid-shell Sn isotopes, most of these experiments were studied almost two decades ago [15–17]. Additionally, these data contain some uncertainties, as mentioned in the recent compilations [18]. The information about ^{118}Sn [produced from

EC decay of ^{118m}Sb ($T_{1/2} = 5.0$ hr)] provided in ENSDF (Evaluated Nuclear structure Data File [18]) incorporates information about some gamma transitions that are not placed in the adopted level scheme. These gamma transitions are only reported in the work of Rahmouni *et al.* [16]. Moreover, all of these previous works had been performed at best with Ge(Li) detectors. Therefore, with the available improved experimental and theoretical tools, decay studies should be revisited to resolve the present ambiguities to understand the nuclear structure better. Such refined decay data might be advantageous to have complete information on beta decay feeding levels, including level lifetimes, moments, etc. Thus the motivation of the present thesis is to study the low-excitation spectra of near mid-shell nuclei from decay spectroscopy with improved detection and analysis techniques that are available to us to eliminate some of the uncertainties.

To have a complete understanding of experimental studies of nuclear structure physics, there is also a need for developmental work. Such activity helps to have thorough knowledge about the detector, data acquisitions system, which are the essential components of any experimental study. Additionally, with the advancement in the detection system, development in the analysis technique is also indispensable.

On a theoretical front, we have reviewed the available effective interactions and constructed a new one to probe important physics issues spanning over the whole isotopic chain of Sn.

1.1.1 Structure of thesis

The subject matter of the thesis has been divided into two major parts: experimental investigation and theoretical study. In the first part of experimental studies, revalidation of decay data and resolution of present uncertainties have been studied through decay spectroscopy experiments described in Chapter 2. The subsequent chapters (Chapter 3 and 4) include associated developments in analysis techniques and detector characterization. The second part contains the results using available nuclear interactions for this mass region to better explain the experimental data theoretically. Large basis shell model calculations have been performed to interpret experimental data of nuclei near shell closure and also of mid-shell isotopes in Chapter 5. A multi-shell interaction has been constructed to describe cross-shell excitation across $N=82$ shell. The details of the calculation and the results obtained using this interaction have been reported in detail in Chapter 6. Additional information on techniques and methodologies used in this thesis are included in the Appendices.

CHAPTER 2

Decay spectroscopy of Sn isotopes

2.1 Introduction

The long isotopic chain of Sn, between two doubly magic ^{100}Sn and ^{132}Sn , is of special interest to both experimentalists and theoreticians. One can study the evolution of nucleon-nucleon interaction from neutron-deficient nuclei ($N \sim Z$, $N/Z \sim 1$) to neutron-rich ($N-Z \sim 32$, $N/Z \sim 1.64$) domain.

The energies of low-lying states, associated electromagnetic transition probabilities, and moments are useful experimental observables for testing and tuning the effective interaction for any region. The experimental data associated with low-lying yrast and non-yrast states are extracted from decay spectroscopy. Most of these studies for nuclei on and close to the stability line have been pursued a long ago. Hence, with the advanced experimental tools, theoretical techniques, and computational facilities, these decay spectroscopy measurements need to be revisited to refine the data further. These studies may result in the completeness of the information on beta decay feeding of levels, including level lifetimes, magnetic and quadrupole moments, etc.

The Sn isotopes lying at the mid-shell of this isotopic chain are mostly stable

($A = 112, 114, 115, 116, 117, 118, 119, 120, 122, \text{ and } 124$). These isotopes are well studied experimentally [18–21]. Most of these studies were mainly intended for the high spin states. The recent nuclear spectroscopy experiments' primary objectives are to extend the measurements to the extremes of angular momentum, energy, and isospin. However, the decay data, particularly for Sn nuclei close to the stable ones, have been obtained almost two decades back [15–18], except for recently published [22] decay spectroscopy data of ^{118}Sn from the decay of ^{118}In . Hence, to have a complete understanding of the evolution of nuclear structure starting from stability to drip lines, the existing knowledge of stable nuclei at low-spins and decay data need to be appropriately refined.

2.2 Interesting features of this region

To describe the region of the long isotopic chain of Sn isotopes, starting from ^{100}Sn to ^{132}Sn , the relevant neutron single particle orbits are $1g_{7/2}$, $2d_{5/2}$, $2d_{3/2}$, $3s_{1/2}$ and $1h_{11/2}$. Among them, $1h_{11/2}$ is the intruder orbit because of its opposite parity relative to the other neighbouring orbits. Due to this intruder nature, neutron $1h_{11/2}$ orbital plays a vital role in the structure of Sn ($Z=50$) nuclei and its neighbours with $N=50-82$. Up to ^{114}Sn (i.e. $N = 64$), the low-lying positive parity states originate primarily from $1g_{7/2}$ and $2d_{5/2}$ orbits. For these light isotopes of Sn, $\nu 1h_{11/2}$ orbit lies at relatively higher energy. Hence, it does not affect the low-lying states significantly. However, beyond $N=64$, when $1g_{7/2}$,

$2d_{5/2}$ orbits are completely filled up, the neutron $1h_{11/2}$ orbit starts playing an important role in the low-lying spectra of the Sn isotopes.

The downward evolution of the energies of yrast $11/2^-$ states of Sn odd isotopes as a function of increasing neutron number is shown in Fig. 2.1 (a). Even with the addition (removal) of two protons in Te (Cd) with $Z=52$ (48), similar variation is observed for odd A isotopes of Te (Cd). Relatively higher angular momentum and opposite parity of $1h_{11/2}$ orbit compared to the other neighbouring positive parity ones ($2d_{3/2}$, $3s_{1/2}$) have been the primary reasons behind the origin of such low-lying isomers for odd isotopes of Sn, Te, and Cd (with $N>64$). Fig. 2.1 (b) shows the half-lives of these $11/2_1^-$ states, which justifies this statement [23].

In the case of even isotopes of Sn ($^{112-132}\text{Sn}$) also, neutron $1h_{11/2}$ orbit plays a significant role in the formation of negative parity low-lying isomers. The evolution of energies and half-lives of yrast 5^- and 7^- states are shown as shown in Fig. 2.2. The angular momenta of these states are generated from the coupling of one unpaired neutron in $1h_{11/2}$ orbit with the other either in $3s_{1/2}$ or in $2d_{3/2}$ orbit.

2.3 Experimental details

In this present work, to study the low energy excited states of $^{117,118}\text{Sn}$, two irradiation experiments were performed using energetic alpha particle beams to irradiate natural Indium targets. Both experiments have been carried out

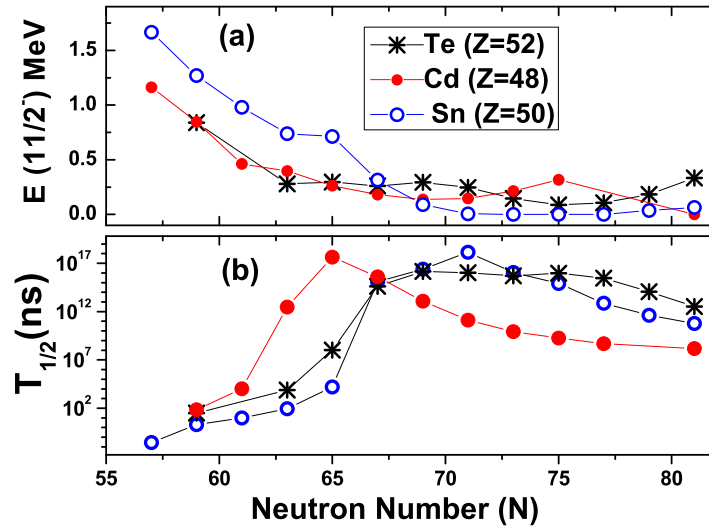


Figure 2.1: Variations of experimental half-lives and excitation energies ([18]) of first $11/2^-$ state of odd A isotopes of Cd ($Z = 48$), Sn ($Z = 50$) and Te ($Z = 52$).

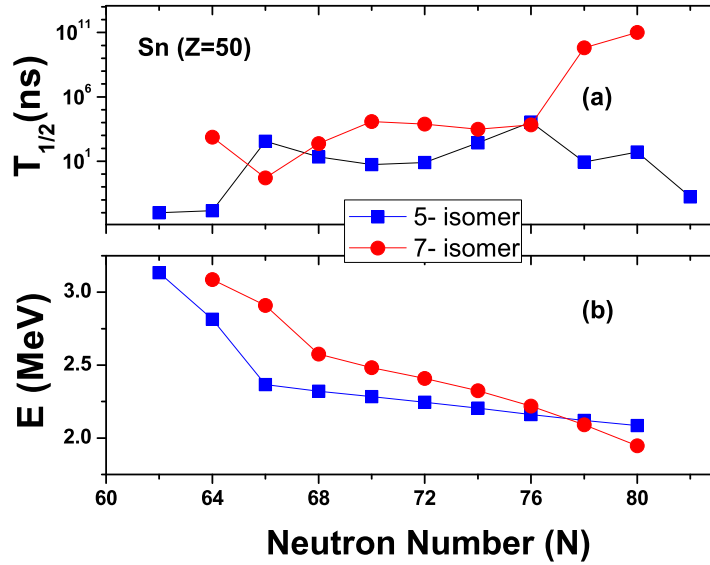


Figure 2.2: Variation of experimental energies and half-lives [18] of $(5^-_1$ and $7^-_1)$ isomer in even A isotopes.

using $K = 130$ cyclotron in the Variable Energy Cyclotron Centre (VECC), Kolkata, India.

This cyclotron facility has four beamlines [24]. The choice of the beamline for an experiment depends on the experimental motivation. The irradiation

experiments with the high current requirement are performed at 0° beamline at channel 1. The second beamline (channel 2) at 15° is utilized for experiments which need a large scattering chamber. The third beamline at 30° (channel 3) is used for gamma-ray spectroscopy experiments and neutron detection-related measurements. The fourth beamline is constructed for the RIB (radioactive ion beam) facility. The schematic layout of different beamlines is shown in Fig. 2.3. The pictures of the beamline and the target mounting flange with the Faraday cup are shown in Fig. 2.4. In the target mounting flange, a Faraday cup is attached to estimate the irradiation dose by measuring the charge collected in it.

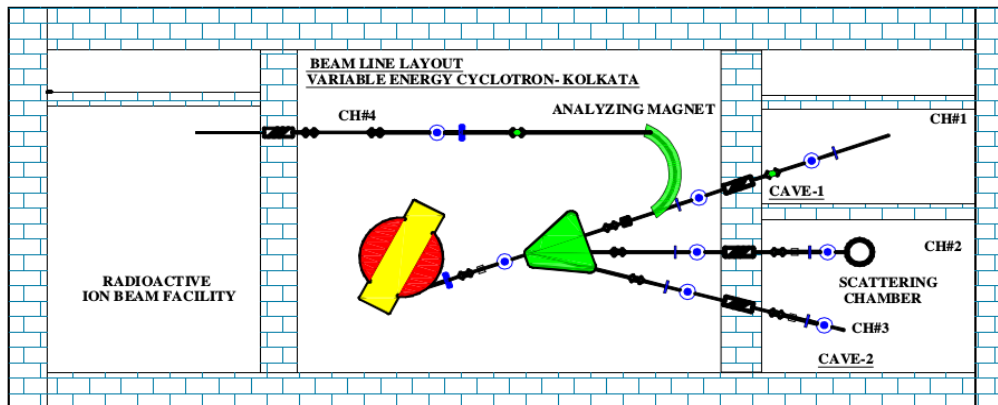


Figure 2.3: The schematic diagram [24]) of the different beamlines of $K = 130$ cyclotron. We have performed the irradiation experiment in channel 1.

2.3.1 Irradiation experimental details:

The experiments have been performed at channel 1 (0°) with a high beam current of approximately $1 \mu\text{A}$. The target chosen for the experiment are foils of



Figure 2.4: (a) The collimator, target holder, and the Faraday cup as indicated in the picture constitute the irradiation flange. (b) The flange position and the direction of the beam along with the beamline are marked in the picture.

natural Indium (In: $Z=49$) of thicknesses 54 and 60 microns. Natural Indium contains mainly two isotopes: ^{115}In with 95.71 (5)% and ^{113}In with 4.29 (5)% abundances [25]. They are irradiated by 32 MeV α -beam.

After the fusion evaporation reaction, a compound nucleus is formed and it decays via various exit channels. To predict the cross-sections of these different channels, we have used PACE4 (Projection Angular-momentum Coupled Evaporation) [26, 27] statistical model code. The results of the calculation are tabulated in table 2.1.

The irradiation time is fixed depending on the half-life of the long-lived nucleus of interest. The half-lives of other nuclei produced during the irradiation, which are not of interest, are also considered before starting the measurement (see, Appendix A).

Table 2.1: The estimated cross-section of different reaction channels. Only the dominant channels are tabulated. The target is ^{115}In with α -projectile of energy 32 MeV. The calculations are done using the code PACE4 [27].

Nucleus	Events	Cross-section		Nucleus	Events	Cross-section	
		in %	in mb			in %	in mb
^{117}Sb	72448	72.40	1.05E3	^{117}Sn	7044	7.04	102
^{114}In	1727	1.73	25	^{118}Sb	48	0.05	0.695

In both cases, the irradiation time was around 5 h . The long-lived isotopes $^{117g,118g,118m}\text{Sb}$, and an isomer of ^{117}Sn were produced. The half-lives of the isotopes and their metastable variants are: ^{118g}Sb : 1^+ ground state ($T_{1/2} = 3.6$ (1) min), ^{118m}Sb : metastable 8^- state ($T_{1/2} = 5.00$ (5) h) [28] and ^{117g}Sb : $5/2^+$ ground state ($T_{1/2} = 2.80$ (1) h) [29]. Along with these two isotopes, a considerable amount of ^{117m}Sn ($T_{1/2} = 13.91$ (3) d) [30] isotope has been populated. The irradiated target is then allowed to cool for a few hours to eliminate the short-lived unwanted activities to a permissible limit. Later it has been brought to a nearby laboratory for counting purposes. Thus, when the counting was started, the activity of ^{118g}Sb : 1^+ ground state has decayed almost fully.

Two different experimental setups utilizing two different approaches (analog and digital) for data acquisition have been used in the two experiments.

2.3.2 Setup I utilizing analog Data acquisition system

The experimental setup consists of two Clover detectors and a ‘low energy photon spectrometer’ (LEPS). Most of the previous decay studies [15–17] have been done with either scintillator or with Ge(Li) detectors. Therefore,

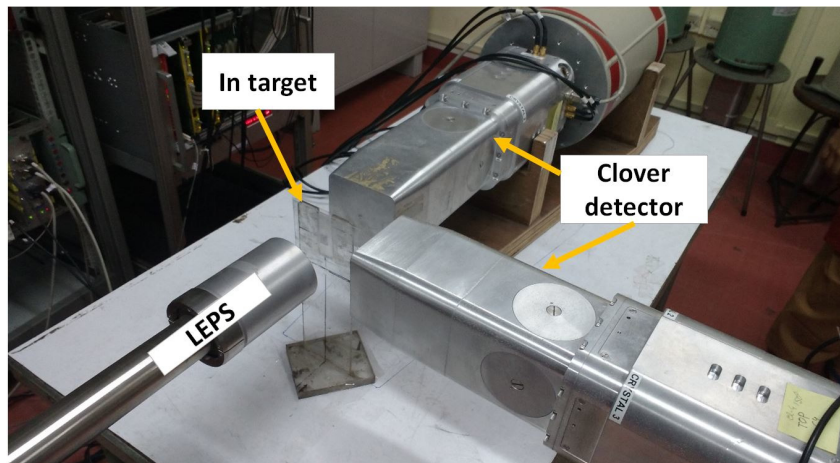


Figure 2.5: Experimental setup I is shown indicating the positions of detectors and the source stand. The distance between each Clover and the source stand is 5 cm.

the present high-resolution and high efficiency set up will be advantageous to improve the results. The Clover detectors are placed at 90° (as shown in Fig. 2.5) with respect to each other. The LEPS detector is set at 180° relative to Clover 1 detector.

For pulse processing, ORTEC amplifiers and other standard NIM electronics were used. Data were collected using VME based data acquisition system (LAMPS software [31]).

Each of the Clover detectors has eight (two for each crystal) output signals that convey the energy and timing information. One set of pulses were fed in amplifiers (ORTEC 672) to shape and amplify the heights of the pulses. Next, they were sent to the Analog to Digital Converters (ADC).

The other set were amplified by using timing filter amplifiers (TFA: ORTEC 474). Then, they were fed to the constant fraction discriminators (CFD: ORTEC CF8000) to generate the signals containing the time information of the pulses by eliminating the effects related to the (amplitude-dependent) time

walks. The four output CFD pulses were properly time matched to preserve the timing correlation among the different crystals. The OR of the time-matched CFD pulses were sent to the input of a Time to Amplitude Converter (TAC) to act as START or STOP signal. The OR outputs were also processed in the input logic unit (ORTEC C04020). This module executes logic functions (AND, OR, NOT, etc) required in most of the coincidence experiments. For the master trigger generation, the OR outputs (of the four CFD outputs) of two Clover detectors and the LEPS have been sent to the gate and delay generator (GG8020). The OR output from the GG unit acted as the master gate signal, or trigger signal in DAQ system to acquire the incoming energy and timing information.

In singles mode measurement, spectra were stored in sequences of 10 minutes. The decay rates for various transitions were followed to identify their origin and confirm their parent nuclei's half-lives. Two TAC (Time to Amplitude Converter) spectra are generated from Clover 1-LEPS and Clover 1-Clover 2 combinations, to acquire time-correlated data and timing information. The data were collected in LIST mode.

The energy calibration of the Clover has been performed using standard radioactive sources, ^{152}Eu and ^{133}Ba . In case of LEPS, the X-ray energies of ^{152}Eu and ^{133}Ba have been taken into consideration. The relative efficiencies of Clovers and LEPS are determined from standard ^{152}Eu and ^{133}Ba sources. The analysis has been done using LAMPS [31] and INGASORT [32] softwares.

2.3.3 Setup II utilizing Digital Data acquisition system

In this approach, data have been collected with a single 80% relative efficiency HPGe detector and a CAEN 5780M desktop digitizer (14 bit, 16k channel, and 100 MS/s). The specific details of the detector and data acquisition system as well as the employed analysis technique will be discussed in forthcoming Chapter (section 3.6.1).

2.4 Results

2.4.1 Decay half-life measurement of parent nucleus from singles data

2.4.1.1 Decay half-life of ^{118m}Sb

To estimate the decay half-life of 8^- state of ^{118m}Sb , the counts (area) under the strong photopeaks of daughter nucleus ^{118}Sn with increasing decay time are determined as shown in Fig. 2.6. The decay constant or half-life is determined from the best fit of the plot with an exponential decay function by using χ^2 -minimization. The extracted half-lives are in well agreement with the previously reported values [18] as shown in table 2.2.

The time-stamped singles data acquired by the digitizer in the second experiment have also been utilized to determine the radioactivity built-up and the decay of ^{118m}Sb (using setup II). The details are in preceding chapter.

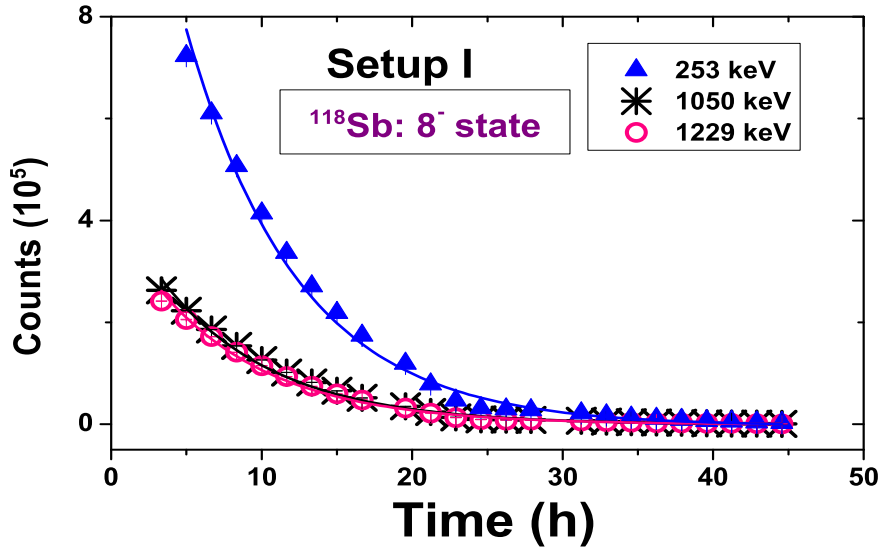


Figure 2.6: The decay curve of parent nucleus ^{118}Sb , monitoring different γ -transitions of ^{118}Sn , as function of decay time utilizing the setup I.

Table 2.2: Half-life of ^{118m}Sb determined from time-evolution of different decay γ -rays for Setup I. The errors are indicated within brackets.

Energy (keV)	Half-life (h)	
	Prev. [18]	Present (Setup I)
253		5.13 (20)
1050	5.00 (2)	5.14 (18)
1229		5.15 (17)
Average		5.14 (10)

2.4.1.2 Decay half-life of ^{117g}Sb

In this particular experiment, ^{117}Sn has been populated through two different decay channels. The first one is via the decay of ^{117g}Sb ($T_{1/2}=2.80$ (1) h [18, 29]) and the other directly through the fusion evaporation reaction, ^{117m}Sn ($11/2^-$ state at 314 keV: $T_{1/2}=14.0$ d). The off-line data has recorded the strong 158 keV γ -ray of ^{117}Sn from both the decays [Fig. 2.7 (left)]. Therefore, while following time evolution of the area of 158 keV γ -ray, two distinctive slopes

must be found if the sufficiently long time data can be acquired. On the other hand, the evolution of 156 keV, which is solely emitted from ^{117m}Sn , will follow the half-life of ^{117m}Sn . But, we could not collect data for sufficiently long time to evaluate the half-life of ^{117m}Sn . The half-life of ^{117g}Sb has been extracted utilizing both the setup I and II. The half-life obtained using setup I is 2.91 (5) [Fig. 2.7 (right)]. The half-life extracted from digital data will be discussed in later Chapter.

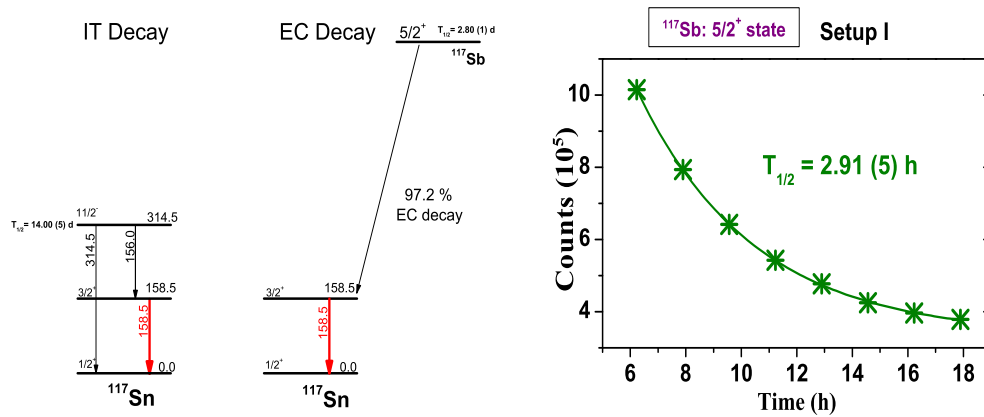


Figure 2.7: Left : The population of 158 keV state ($3/2^+$ state of ^{117}Sn) from ^{117m}Sb ($5/2^+$ state) and ^{117m}Sn IT decay is shown in figure. Right : The decay curve of ^{117}Sb following the time evolution of 158 keV γ -transition from experimental setup I.

2.4.2 Excitation energy and Level structure : ^{118}Sn

The work started with searching already known and placed [18] γ -transitions of ^{118}Sn populated from the electron capture decay of ^{118}Sb . The job of placing the gamma in the level scheme is done by inspecting coincidence relationship. By putting a gate on this unknown transition on the one axis, other coincidence partners are identified from the projected spectrum.

In all the earlier experiments [15–17] including in current experiment, the

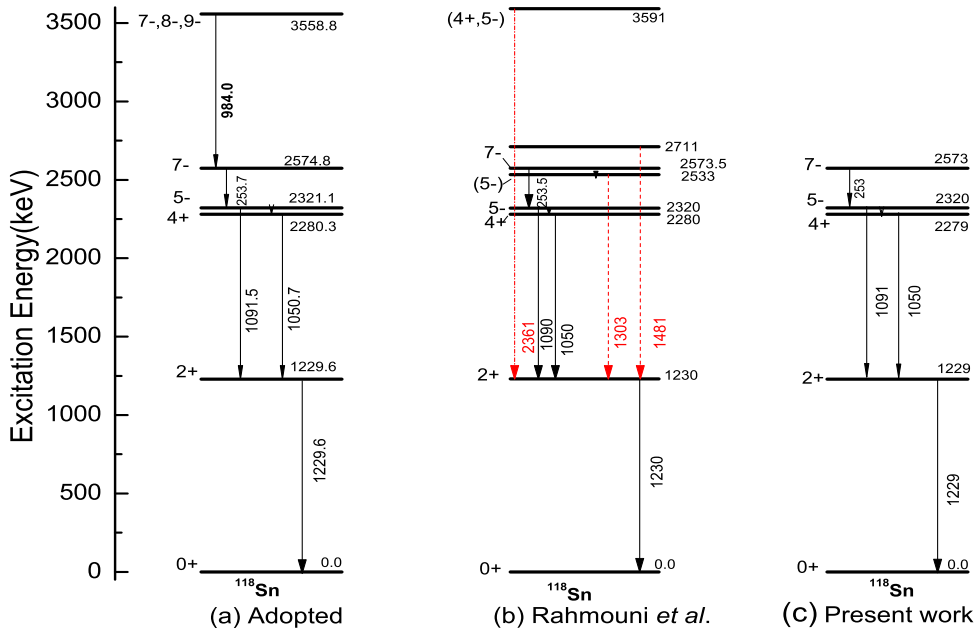


Figure 2.8: The decay scheme of ^{118}Sn via E.C. decay from 8^- state of ^{118}Sb . The 40 keV transition (coming from 5^- state to 4^+) is not mentioned because of closed spacing. Fig. (a) Adopted in NNDC, Fig. (b) decay scheme presented by Rahmouni *et al.* [16]. Red transitions are unplaced gammas that are not adopted in NNDC. Fig. (c) The decay scheme proposed from present work. Level energies and gamma transitions are expressed in keV.

strong peaks at energy 41 keV, 253 keV, 1050 keV, 1091 keV and 1229 keV are seen unambiguously. An additional γ -transition (984 keV) from the level energy 3558.8 keV level is assigned in the adopted level scheme [18] as shown in Fig. 2.8 (a). This transition is only mentioned in the work of Hattula *et al.* [17]. Additionally, three unplaced γ -transitions are enlisted without any assignment of spin-parity or placement in the National Nuclear Data Centre [18]. These unplaced γ -transitions, such as 1303 keV, 1482 keV, 2362 keV and also 984 keV have been identified in this current experiment. In order to clarify this ambiguity, three different symmetrised E_γ - E_γ (Clover-Clover) correlation matrices have been build up by putting different timing condition in the TAC spectrum, such as, (a) no timing condition, (b) gate of 855 ns and (c) gate of 270 ns. The projected spectra are generated from time gated matrix

with coincidence time window of 270 ns, such that the randomly correlated peak at 158 keV (most intense γ -ray emitted from excited state of ^{117}Sn) can be eliminated significantly. The gated spectra of the strong gammas such as 253 keV, 1050 keV and 1229 keV generated (270 ns time gated matrix) are shown in Fig. 2.9. In the gated spectrum of 253 keV, coincident 1050 keV, 1229 keV, 1091 keV, 41 keV as well as X-ray of Sn (25 keV) are seen properly, which is expected. Along with these, a few gamma-transitions such as 1387 keV, 2279 keV and 2362 keV are also seen in the projected spectrum. Among these, 2362 keV has been reported only in Ref. [16]. In the same manner, in the gated spectrum of 1050 keV, unknown gamma transitions are observed at energy 411 keV, 1387 keV and 1482 keV (Fig. 2.9). In case of gate at energy 1229 keV, additional transition at 1208 keV and 1303 keV are identified. Among these unplaced transitions, 1303 keV, 1482 keV and 2362 keV are reported only by Rahmouni *et al.* [16]. This group has placed these gammas in their proposed decay scheme (Fig. 2.8 b) but it is not adopted in National Nuclear Data Centre [18].

2.4.2.1 984 keV:

As mentioned earlier, this particular γ -ray is adopted in the level scheme and it originates from $I^\pi = (7^-, 8^-, 9^-)$ state to 7^- state with very low intensity (Fig. 2.8). The presence of this transition is confirmed only in Hattula *et al.* [17]. But in our present data, in the gate of 253 keV, it is seen very weakly (almost

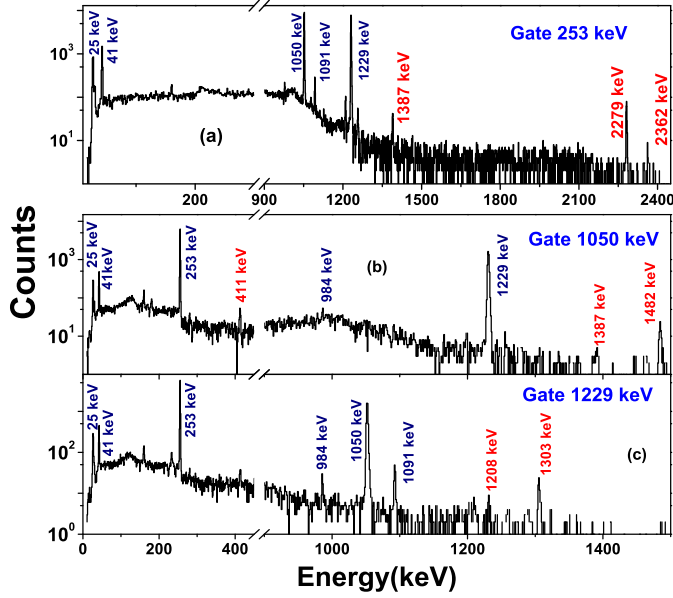


Figure 2.9: Spectra gated by different strong γ -rays (253 keV, 1050 keV, 1229 keV) are shown. The γ -transitions confirmed in the present work and also included in the adopted decay scheme [18] are marked (blue colored). Energies of the unplaced [18] and new γ -rays are written in red-colored fonts.

comparable to the background level). Whereas, strong existence is observed in the gated spectra of 1050 keV and 1229 keV (Fig. 2.9). Weaker presence in the gated spectrum 253 keV is unexpected as this transition has been shown to feed the level, which deexcites by emitting 253 keV transition. Therefore, it is an indication that even if 984 keV belongs to ^{118}Sn , it is not placed correctly. In reverse gate of 984 keV (Fig. 2.10), the transitions at energy 66 keV, 245 keV, 476 keV, 1050 keV and 1229 keV are observed. Presence of strong peak at 245 keV instead of 253 keV in the gated spectrum is an indication of a problem in placing that transition in level scheme. It is found out from E_γ - E_γ two dimension plot (Fig. 2.11) that, this 245 keV and 984 keV are correlated Compton pairs of 1229 keV. Similarly, 66 keV is a part of 1050 keV Compton line with the complementary part 984 keV. From this, it is concluded that 984 keV is Compton part of 1050 keV and 1229 keV. Furthermore, by comparing

the decay scheme of $^{120,122,124}\text{Sn}$, the presence of 984 keV can be ruled out also.

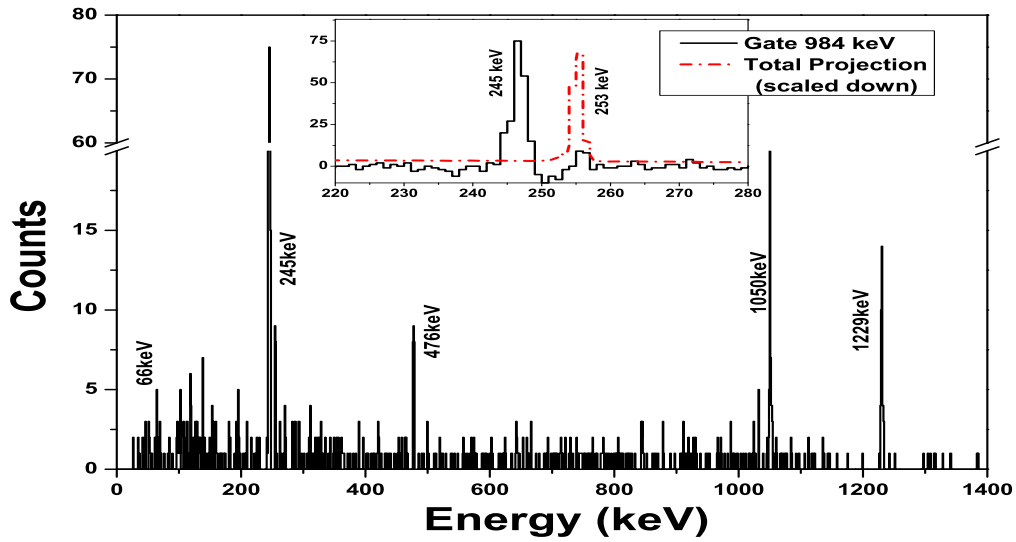


Figure 2.10: The gated spectrum of 984 keV transition. In inset, it is compared with the normalised total projection spectrum of Clover detector.

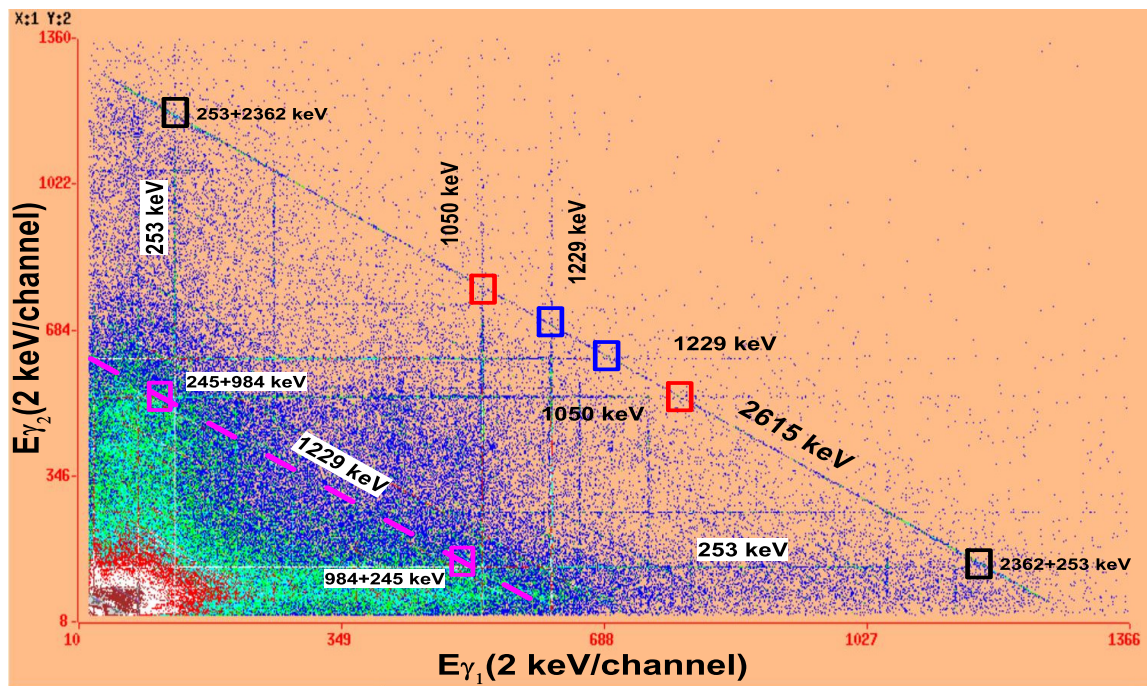


Figure 2.11: The E_γ - E_γ matrix is shown. The Compton lines ($E_{\gamma_1} + E_{\gamma_2} = E_\gamma$) corresponding to $E_\gamma = 1229$ keV and 2615 keV are indicated. The vertical and horizontal lines corresponding to correlated photopeaks of 253 keV, 1050 keV and 1229 keV are also marked. .

2.4.2.2 The unplaced γ -transition:

From the coincidence study, we can establish that all of these unplaced transitions (411 keV, 1208 keV, 1303 keV, 1387 keV, 1482 keV, 2279 keV, 2362 keV) as well as 984 keV transition do not belong to ^{118}Sn . These transitions are originating from the three different conditions. These peaks are generated due to random summing and also from coincidence summing. Since only two Clover detectors have been utilized in the experiment, even the correlated Compton parts appeared as distinctive peaks. The various events have been categorised in different sections:

1. 411 keV, 1208 keV and 1387 keV peaks are originating from random summing of 253 keV, 1050 keV and 1229 keV γ -rays, respectively, of ^{118}Sn with intense 158 keV γ -ray of ^{117}Sn due to high count-rate and/or during the addback process.
2. 1303 keV and 1482 keV peaks are arising from coincidence summing of intense 253 keV γ -rays with 1050 keV and 1229 keV transitions, respectively (from ^{118}Sn itself).
3. From 2D plot of E_γ - E_γ matrix (Fig. 2.11), it is concluded that 2279 keV peak originates from coincidence summing of 1050 keV and 1229 keV, which are emitted sequentially.
4. These correlated Compton scattered pairs of γ -rays are,
 - (476 keV + 984 keV) and (157 keV + 1303 keV) and (1208 keV

- + 253 keV) arising from 1460 keV room-background γ -ray emitted from long-lived ^{40}K .
- (253 keV + 2362 keV) and (336 keV + 2279 keV) and (1386 keV + 1229 keV) and (2204 keV + 411 keV) from 2615 keV emitted from the decay of ^{208}Tl , which is a progeny of long-lived ^{232}Th ($T_{1/2} = 1.40(1)\times 10^{10}$ y).
- (66 keV + 984 keV) from 1050 keV and (245 keV + 984 keV) from 1229 keV, an intense γ -transition of ^{118}Sn .

The details of the origin of these unplaced γ -rays are given in Table 2.3. For each γ -transition, the table contains information about the energy of the gates in which it is observed (Fig. 2.9). It also enlists the γ -transitions observed in the spectrum gated by that particular unplaced γ -transition (Fig. 2.12). Finally, based on these observation, we have identified the origin of these γ -transitions.

2.4.2.3 Relative Intensities and Feeding Pattern: ^{118}Sn from ^{118m}Sb

The relative intensity of gamma transition contains information regarding the population of the different levels. We have calculated the relative intensity from the time gated (855 ns) symmetrised γ - γ matrix to remove the unwanted contributions coming from background. The intensity of low energy 41 keV includes substantial error due to uncertainties associated with the threshold values of the CFD of different crystals of the Clovers. The corrections due to the presence of sum-peaks have been incorporated in the intensity calculation,

Table 2.3: The list of γ -transitions, which do not originate from ^{118}Sn , but observed in the present work. The origins of these γ -rays are also listed. All the energies are quoted in keV.

Energy	Seen in gate	γ -rays observed in reverse gate	Remarks
411	1050	1229, 1050, 2204	(158+253) keV (2204+411) keV = 2615 keV
984	1050, 1229	66, 245, 476, 1050, 1229	(66+984) keV = 1050 keV (245+984) keV = 1229 keV (476+984) keV = 1460 keV
1208	1229	156, 253, 1229	(158+ 1050) keV (1208+253) keV = 1461 keV
1303	1229	158, 1229	(253+1050) keV (157+1303) keV = 1460 keV
1387	1050	253, 1050, 1229	(158+1229) keV (1387+1229) keV = 2616 keV
1482	1050	1050	(253+1229) keV
2362	253	253	(253 + 2362) keV = 2615 keV
2279	253	253, 336	(1050+1229) keV (336+2279) keV = 2615 keV

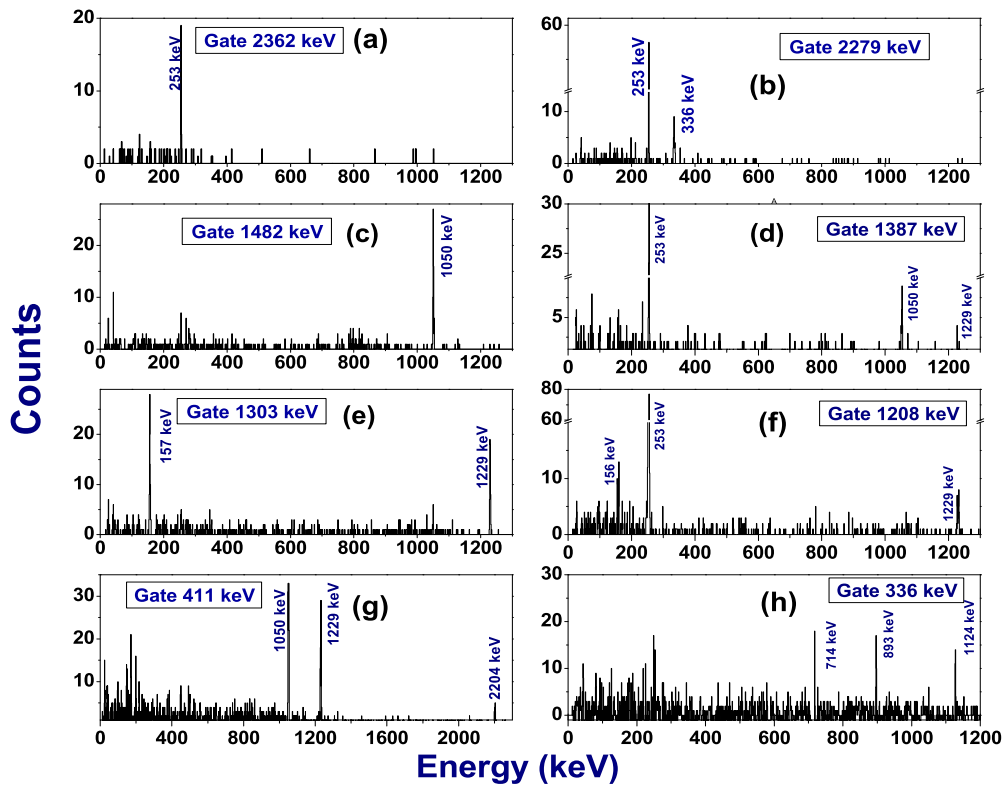


Figure 2.12: The gated spectra of new or unplaced transitions are shown.

wherever needed. The relative intensity values are tabulated in the table 2.4.

From the present investigation, we have ruled out the presence of 984 keV γ -

Table 2.4: Intensity of γ transitions. The conversion coefficients are obtained from Ref. [18].

Energy (keV)	I_γ		$I_{\gamma+c.e}$	
	Adopted [18]	Present	Adopted [18]	Present
41	30 (2)	29 (5)	97 (6)	92 (16)
253	99 (6)	91 (6)	105 (6)	97 (6)
1050	97 (5)	95 (5)	97 (5)	95 (5)
1091	3.6 (3)	3.2 (3)	3.6 (3)	3.2 (3)
1229	100 (5)	100 (5)	100 (5)	100 (5)

transition in the decay scheme as shown in Fig. 2.8 (c). Therefore, the feeding intensity of 2573 keV (Fig. 2.8 (a)) has been modified from 98.3% [18] to 100%. No other levels have any direct feeding.

2.4.3 Level lifetime measurement

In nuclear spectroscopy, determination of level lifetime of nuclear excited state carries wealth of information as it provides insight about the internal structure, shape, deformation etc. The lifetimes of excited states cover a very broad range, and therefore several techniques are applied depending on the range of lifetime of the nuclear state. In this current work, we have mostly used delayed coincidence technique, where time difference between two events occurring within the coincidence window is measured.

In order to have accurate measurement of lifetime, we need to consider the intrinsic time resolution of the experimental set up. That arises because of the time fluctuation of the detectors and associated electronics. To have a knowl-

edge about the time resolution, one has to derive the experimental prompt distribution. This can be obtained by using a radioactive source that emits consecutive gamma radiations strictly simultaneously. So that, the level lifetime of the nuclear state (radioactive source) is very smaller than the lifetime that we want to measure. In general, this prompt distribution $[P(t)]$ is a symmetric Gaussian distribution (if two similar kind of detectors are used). The full width at half maximum i.e. FWHM of this distribution is noted as time resolution of the experimental setup. It is important that the prompt curve has to be generated under the same conditions as the delayed distribution.

The delayed time distribution $[F(t)]$ is not an ideal exponential function, but it is the result of convolution of $P(t)$ with the exponential function (say, with decay constant λ). It can be expressed as [33],

$$F(t_j) = N\lambda \int_0^{\infty} P(t_j - t)e^{-\lambda t} dt, \quad (2.1)$$

where, N is the total counts of the time distribution, $P(t_j)$ corresponds to prompt time distribution (in general) and λ is the characteristic decay constant of the isomeric state.

Depending on the order of the lifetime generally two methods are used to extract the life-time : slope method or deconvolution method and centroid shift method. We have used slope method as well as deconvolution techniques to extract the lifetimes. Taking logarithmic derivative of the equation 2.1, one can deduce the following equation [33, 34],

$$\frac{d}{dt} \ln F(t) = -\lambda(1 - P(t)/F(t)). \quad (2.2)$$

Now, for the situation, where $F(t) \gg P(t)$, equation 2.2, reduces to

$$\frac{d}{dt} \ln F(t) = -\lambda. \quad (2.3)$$

This particular method is known as slope method. It is applied generally if the level lifetimes are much longer (approximately 30% [35]) than the time resolution of the experimental set up. If the lifetime is comparable or slightly longer than the prompt distribution, then deconvolution technique is used. In this particular case, the prompt distribution is an important parameter. In this process the real delayed distribution is extracted by unfolding the delayed distribution with the help of prompt distribution. In this case the delayed function is defined as [36, 37].

$$\begin{aligned} F(t_j) &= N_0 \int_0^{\infty} P(t_j - t) \frac{1}{\tau} e^{-t/\tau} dt \\ &= N_0 \int_0^{\infty} \frac{1}{\sqrt{2\pi}\sigma} e^{(t_j-t)/2\sigma^2} \frac{1}{\tau} e^{-t/\tau} dt \\ &= \frac{N_0}{2\tau} e^{-t_j/\tau} e^{\sigma^2/2\tau^2} \left[1 - \operatorname{erf}\left(\frac{\sigma}{\sqrt{2}\tau} - \frac{t_j}{\sqrt{2}\sigma}\right) \right] \end{aligned} \quad (2.4)$$

where, the prompt distribution is defined by Gaussian distribution with width σ and the decay constant λ of exponential function is given by, $\lambda = 1/\tau$. Here, N_0 is the normalisation constant and $\operatorname{erf}(\dots)$ is the the error function and also $F(t_j)$ is described as the convolution of Gaussian and exponential distribution.

2.4.3.1 Result of ^{118}Sn

In the present work, lifetimes of both the levels at energies 2320 keV (5^-) and 2573 keV (7^-) are remeasured from Clover-Clover TAC data using delayed coincidence technique. To extract the half-life of 7^- state, the TAC spec-

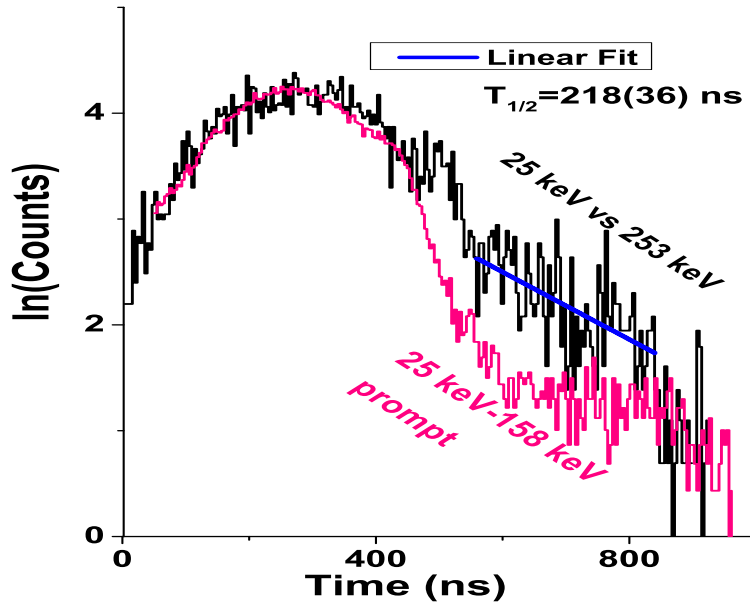


Figure 2.13: Projection of TAC spectrum gating 25 keV in one Clover detector and 253 keV in the another (in log scale). The TAC spectrum has been compared with prompt distribution (normalised) obtained by gating 25 keV and 158 keV in the detectors.

trum is projected under the condition of gating the energy spectra of Clovers. That particular level (at $E_{level} = 2573$ keV) has direct feeding (100% as established in present work) through electron-capture (E.C.) decay from ^{118m}Sb . The electron-capture decay has an associated emission of K X-ray (25 keV). Thus a TAC spectrum has been generated by selecting 25 keV (Sn K X-ray) in one Clover, and 253 keV is chosen in the other. It has been compared with the prompt spectrum generated from 25 keV vs 158 keV (intense γ -ray of ^{117}Sn) TAC spectrum. An additional slope of the delayed spectrum is observed as

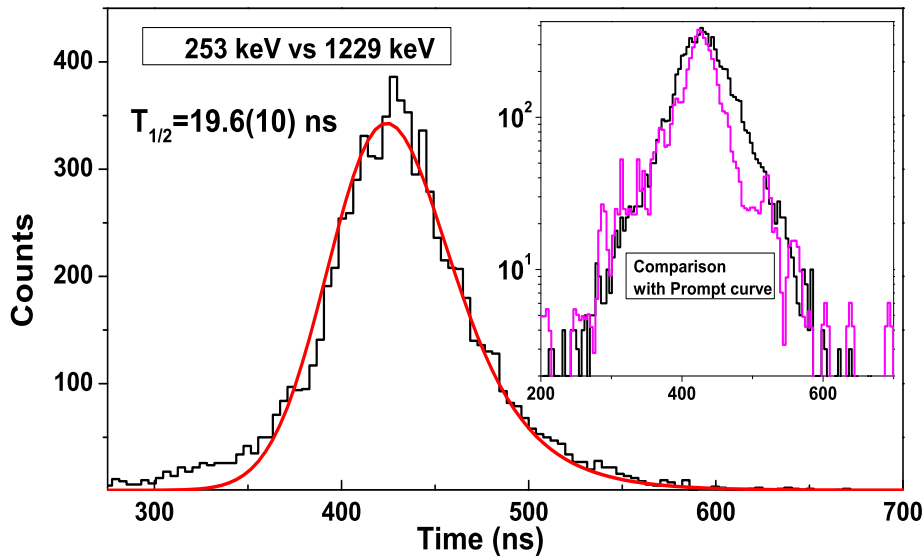


Figure 2.14: Projection of TAC spectrum gating 253 keV in one Clover detector and 1229 keV in the another. In the inset, the TAC spectrum is compared with prompt distribution (normalised) gating after region 253 keV and 1229 keV in the detector.

shown in Fig. 2.13. By fitting the delayed region by a straight line, the half-life is estimated from the slope of the line as shown in the Fig. 2.13. The half-life is deduced to be 218 (36) ns.

Now, the same procedure has been followed to evaluate the lifetime related to 5⁻ state. The TAC spectrum has been generated by putting energy gates at 253 keV in one detector and another at 1229 keV. Instead of choosing the immediately following transition such as highly converted 40.8 keV; 1050 keV, or 1229 keV is selected in order to minimize the contribution coming from the energy jitter for timing. Also, the half-lives of the associated states are much smaller (<0.7 ns [18]). Gating 1229 keV does not add further time delay. For this case, prompt spectrum is generated by gating the region after 253 keV (over the same number of channels as 253 keV gated) vs 1229 keV (inset of Fig. 2.14).

Since the reported half-life of this level [18] is 21.7 (2) ns, which is comparable to the full width at half maxima (FWHM) of prompt curve, deconvolution of Gaussian and exponential has been applied (as described in equation 2.4) to extract the half-life. The half-life of (5^-) is found out to be 19.6 (10) ns (Fig. 2.14). Similar order of result has also been estimated from 253 keV vs 1050 keV gated spectrum.

2.4.3.2 Result of ^{117}Sn

As stated earlier, ^{117}Sn is populated from two different decay channels: a) via decay of ^{117g}Sb [$T_{1/2} = 2.80$ (1) h] [18, 29] and b) from an isomeric state of ^{117}Sn having $T_{1/2} = 14.00$ (5) d [18] ($J^\pi = 11/2^-$). From the statistical model calculation (PACE 4 [26]), it is estimated that the cross-section in fusion reaction is about 7% (table 2.1). This isomeric state decays primarily via emission of two coincident γ rays of energies 156 keV ($11/2^- \rightarrow 3/2^+$) and 158 keV ($3/2^+ \rightarrow 1/2^+$). The 156 keV transition is of M4 character, and hence, it is highly converted, with a conversion coefficient = 46.9 [18](see appendix B).

Our main objective is to remeasure the level lifetime of $3/2^+$ state of ^{117}Sn . From earlier studies, estimated lifetime is of the order of 279 (9) ps [18]. The lifetimes obtained from other measurements [39] deviate around 12-30% from the adopted one. This short lifetime can be usually measured using fast scintillators. But, the main difficulty of measuring this is to separate out feeding gamma (156 keV) from the decaying gamma of the 158 keV state. The difference being only 2 keV, one cannot resolve these two gammas using commonly

used fast timing detectors. As a result of this, both sides of the delayed spectrum contain timing information. It needs some special analysis technique to resolve this. P. John *et al* [38] has discussed this technique. However, the type of detector used in the measurement of lifetime was not explicitly mentioned in the reference. In another work [39], both conversion electron-electron and electron- γ -ray coincidence measurements were done and the lifetime is reported as $T_{1/2} = 0.31 (3)$ ns. Hence, this lifetime needs a remeasurement for resolving this ambiguities.

•Present work

To address this uncertainty, we have used two different setups consisting of different fast scintillators.

2.4.3.2.1 Setup 1: Measurement with LaBr₃(Ce) and BaF₂ scintillators: In the first measurement, the setup consists of a LaBr₃(Ce) and BaF₂ scintillators. $\gamma - \gamma$ timing spectra (TAC) has been generated by gating 154-160 keV in both detectors using necessary analog electronics . In our experimental setup, prompt spectrum is generated using ²²Na source. The time calibration of this spectrum is 0.09 ns/ch.

As stated earlier, ideally, prompt TAC spectrum should be generated under the identical condition as in the delayed case. But, due to unavailability of radioactive sources with emitting correlated photopeaks at similar energy range, the prompt spectrum has been generated by gating at the Compton continuum

at an energy region 154-160 keV. The system resolution of this setup is 900 ps (at energy range 154-160 keV). As discussed earlier, deconvolution technique has to be adopted, when the prompt resolution is comparable to the level lifetime.

In general, deconvolution method is an iterative approach where decay curve and the prompt time distribution are separated from experimental delayed time distribution [42]. However, in the case of unresolved feeding and decaying gammas, normal deconvolution method does not work properly [38].

Using two similar kind of detectors, for the degenerate feeding and decaying transition, the delayed time distribution (equation 2.1) can be modified as [38, 43],

$$F(t_j) = N \int_0^{\infty} [P(t_j - t) + P(t_j + t)]e^{-\lambda t} dt. \quad (2.5)$$

Since in our experiment, the start detector and the stop detector are different, the prompt function will not be a symmetric one (as the right and left edges are different). So, the decay spectrum has to be modified as,

$$F(t_j) = N \int_0^{\infty} [P(t_j - t) + P'(t_j + t)]e^{-\lambda t} dt, \quad (2.6)$$

where $P(t_j-t)$ and $P'(t_j+t)$ represent the prompt characteristics of two dissimilar detectors. Since the prompt distribution is asymmetrical, the distribution is segregated into two parts (i.e. left part and right part). It is fitted with two different Gaussian functions having two different width parameters (say, σ_l, μ_l for left part and σ_r, μ_r for right part). The two different parameters of Gaussian

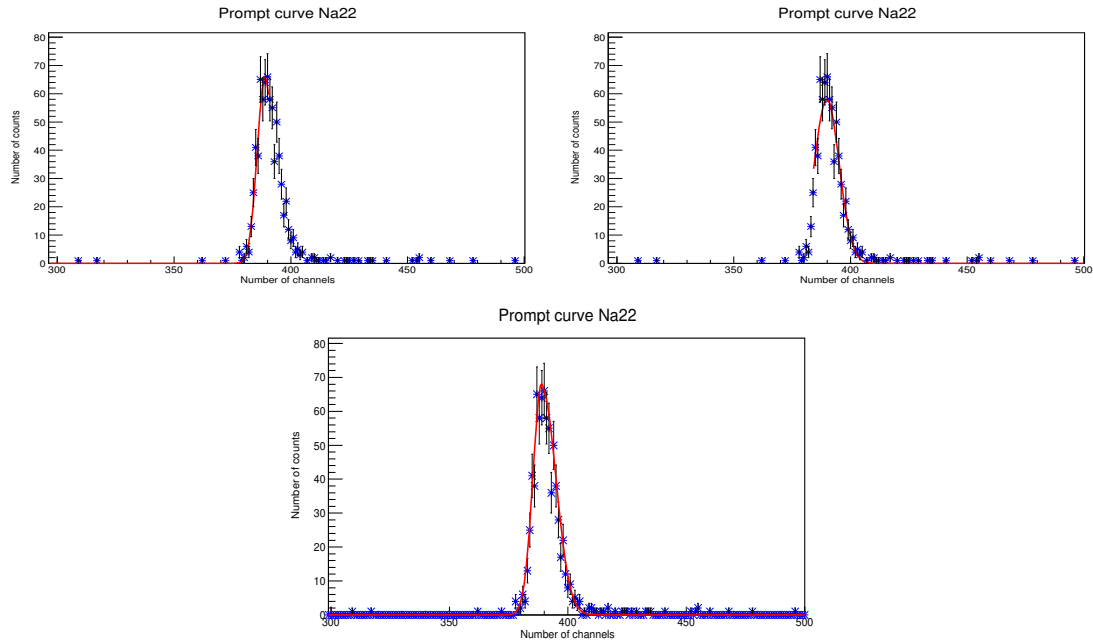


Figure 2.15: The prompt TAC spectrum of ^{22}Na obtained by gating 154-160 keV in both detectors of set up I. The TAC spectrum is fitted with two different Gaussian distributions. The fitted left-side is shown in topmost left and right side is shown in topmost right part. In bottom, the asymmetrical prompt curve is fitted with the Gaussian distributions having different parameters for two sides.

distribution are used to fit the full prompt distribution (Fig. 2.15).

Now, by varying the decay parameter of exponential function (of equation 2.6), the best fit of the delayed spectrum has been obtained by minimisation of χ^2 (Fig. 2.16). The procedure has been executed numerically using ROOT package [44]. The minimum χ^2 of the fitting is obtained half-life $T_{1/2}=0.281$ (28) ns. Both statistical as well as fitting error have been considered.

2.4.3.2.2 Setup 2: Measurement with VENTURE array:

Experimental details In this experimental set up, we have used **VENTURE** array (abbreviation of VECC array for Nuclear fast Timing and angUlar corRelation studies (VENTURE)).

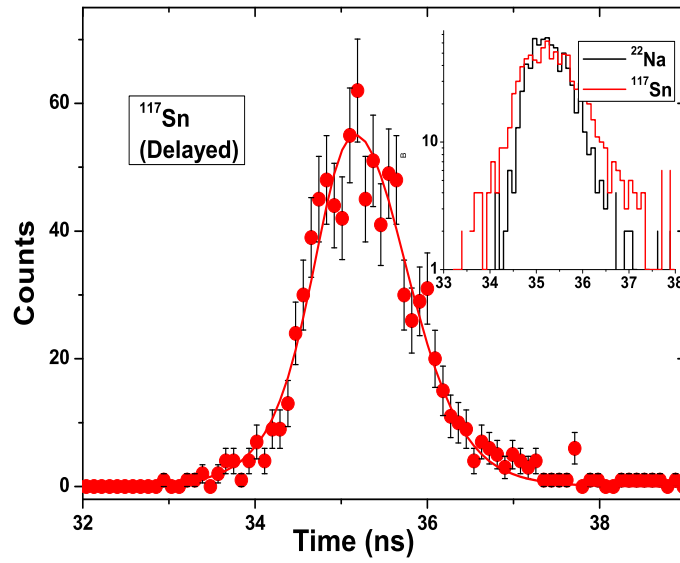


Figure 2.16: The time-delayed spectrum of ^{117}Sn is fitted with convoluted function. In inset, comparison of the prompt (^{22}Na) and delayed (^{117}Sn) TAC spectra is shown.

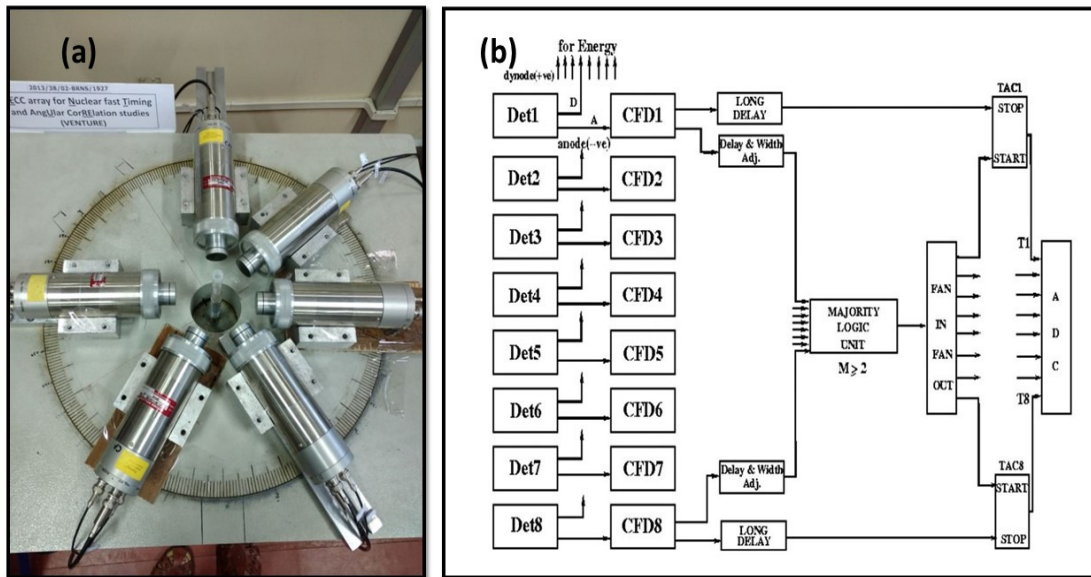


Figure 2.17: Fig. (a) The setup of VENTURE array with six CeBr_3 detectors is shown. (b) The schematic diagram of electronics used for timing signal processing. The set up is identical to Ref. [45] except for the number of detectors.

The set up consists of six (6) CeBr_3 detectors, having dimension of $1'' \times 1''$. The characterisation details of the detector can be found in the Ref. [45]. Each of the detector has been coupled with Hamamatsu R9779 PMT. Along with

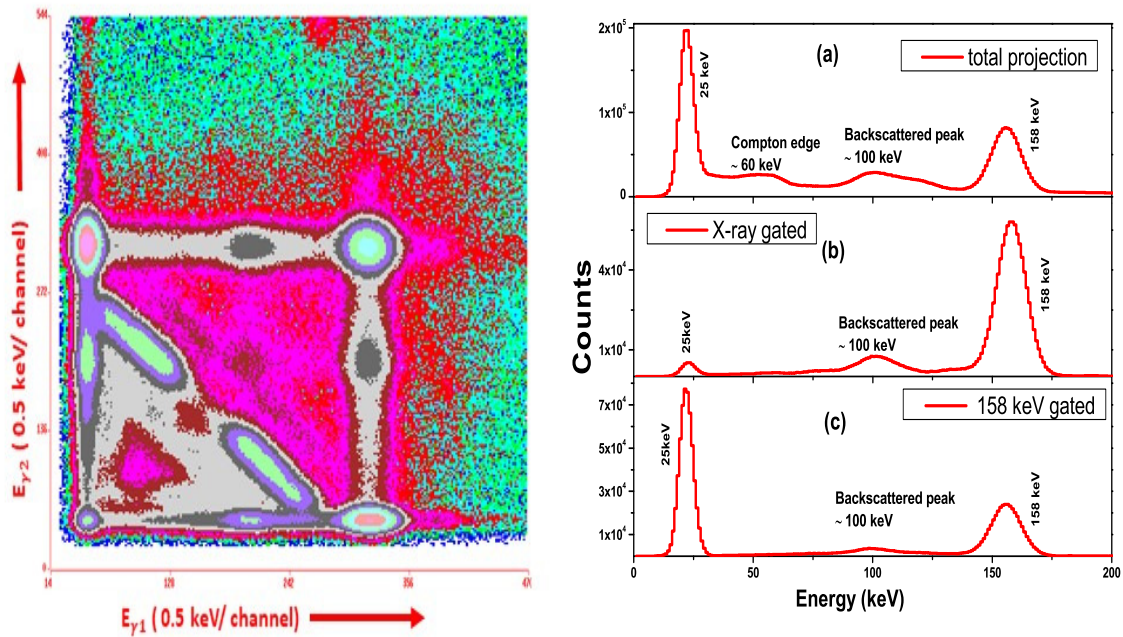


Figure 2.18: (Left) Two dimensional E_γ - E_γ matrix is generated from the data collected using six CeBr_3 detector. (Right) The total projected spectrum obtained from the matrix is shown. The gated spectra are obtained by gating Xray and 158 keV peaks.

this, standard NIM based electronics has been used for pulse processing. To acquire data, VME based data acquisition (that includes Mesytec MAD-32 unit and *LAMPS* [31] data acquisition system) has been used. All of the detectors are operated at bias voltage -1.2 kV (using ORTEC 556 module). At this high voltage, the detectors show best time resolution. In this present set up, we have followed common start technique. The schematic diagram of the experimental set up is same as Fig. 2.17(b) as mentioned in Ref. [45]. In our case the only change is in the detector number which is six instead of eight. The details about the experimental setup can also be found in this reference.

Data analysis procedure and results: At our present experiment, list mode data have been stored at an interval of 1 h. Data of standard radioactive source,

^{152}Eu is taken for the energy and efficiency calibration. At the starting, the energy spectra are calibrated. Now, all the energy as well as time parameters are gain matched. In some cases, the drift in the amplifier as well as in TAC spectrum is observed with increasing time. Because of this, accurate gain matching is an essential step.

During the analysis, the list mode data have been sorted in such a way that the ADC corresponding to the energy (say E_m and E_n) and timing parameter (TAC_m and TAC_n) contain valid data. Now, for each of the events, TAC_m and TAC_n are subtracted. The resultant spectrum is the time difference spectrum TAC_{mn} ($m > n$). In the current setup, there are 6 detectors. So, ${}^6\text{C}_2$ i.e. 15 unique combinations of time difference spectra (TDS) can be generated. Now, a shift is observed between these different combination of time difference spectra. This discrepancy is removed by matching all the TAC spectra with respect to a particular TAC spectrum. After that, all these spectra have been added to generate the 'Total Time Difference Spectrum'. Additionally, the gain matched energy of each pair of detectors E_m and E_n are kept in two energy parameters. In this condition, these two energy parameters with total TDS are equivalent to a setup containing two detectors.

Now, the Tac spectrum can be projected by gating feeding transition in one of the energy parameter and decaying transition in the other.

Two dimensional energy-energy ($E_{\gamma 1}$ vs $E_{\gamma 2}$) symmetric $\gamma - \gamma$ matrix is constructed as shown in Fig. 2.18(a). The total projection is also shown in Fig. 2.18(b) (topmost). In the Sn K X-ray (25 keV) gated spectrum, the peak of

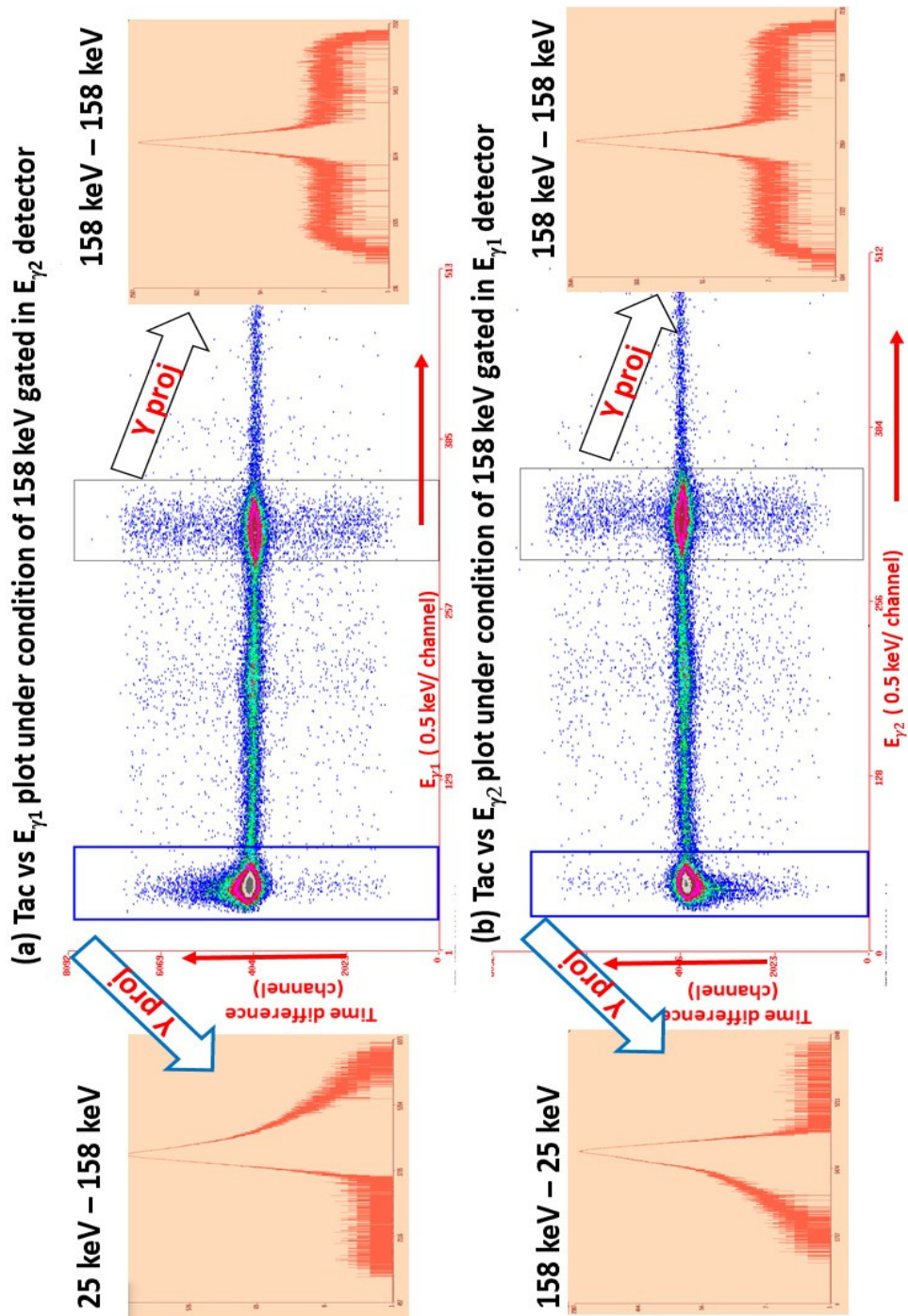


Figure 2.19: Two different matrices are constructed under two different conditions : (a) Time difference (TAC) vs. E_{γ_1} matrix is build up by gating 158 keV in E_{γ_2} and (b) vice versa. Different projected regions are also shown in the figure.

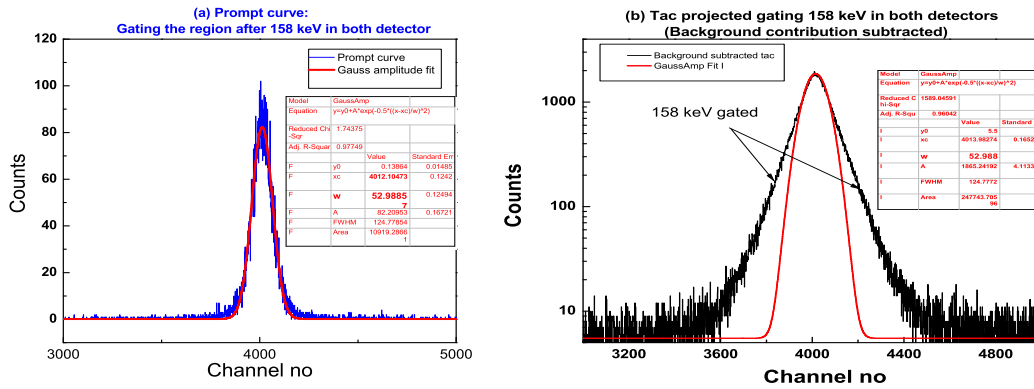


Figure 2.20: (a) The prompt TAC curve is generated by gating after region of 158 keV and it is fitted with a Gaussian distribution [shown by red curve]. (b) Delayed TAC curve is built up by gating 158 keV in both the detector. It is fitted with a Gaussian distribution function fixing the same width parameter obtained from the fitted prompt spectrum.

156-158 keV (unresolved) is seen very clearly. A small contribution of 25 keV (self-coincidence) is also observed. A bump around energy 100 keV is also marked that corresponds to the region of backscattered peak of 158keV. The gated spectrum of 158 keV shows the peak of 156 keV (unresolved) as well as the peak of Sn X-ray.

The time resolution at the photopeak energies of ^{60}Co is 0.154(8) ns for any two CeBr_3 detectors. The time resolution for the full array is 0.188 (3) ns [45]. In order to estimate the half-life, two matrices are generated having time difference (TAC) in one axis (say along Y axis) and energy parameter (say, $E_{\gamma 1}$ along X axis) along the other axis under condition of 158 keV gated in another energy parameter (say, $E_{\gamma 2}$) and vice versa (Fig. 2.19). The TAC spectrum is projected under condition of gating 156-158 keV in the both energy parameters. Since, 156 and 158 keV can not be distinguished properly, same region (158 keV photo-peak) is gated. As a result, the timing information is present in both sides of delayed spectrum. Hence, both sides of the delayed distri-

bution show exponential slope. The prompt spectrum is generated by gating Compton region after 158 keV photo-peak in the both detectors (Fig. 2.20 (a)). The resolution comes out to be 762(2) ps. The background contribution is subtracted from the total TAC to have only real counts as discussed in Appendix C (Fig. 2.21 (a)). Since, the start and stop γ -rays are almost degenerate, the centroids of the delayed and anti-delayed distributions shift opposite to each other. Hence, the centroid of the distribution does not show any effective shift. The left part of the delayed spectrum is now replaced by a Gaussian distribution having the same width of the prompt spectrum (Fig. 2.20 (b)). Now, this modified delayed spectrum (Fig. 2.21 (b)) is fitted with an exponentially modified Gaussian distribution (as described in equation 2.4). Using deconvolution technique, the half-life has been deduced to be 258 (18) ps. Since the statistical error is too small, only error from the fitting parameters are considered.

From these two above measurements, the weighted half-life of $3/2^+$ state of ^{117}Sn is deduced to be 265 (15) ps.

Table 2.5: Comparison of experimental lifetimes of excited levels in $^{117,118}\text{Sn}$ measured in the present work with previous data.

Spin (I^π)	E_x (keV)	Half-life ($T_{1/2}$)	
		Prev. [18]	Present
^{118}Sn			
5^-	2320	21.7 (2) ns	19.6 (10) ns
7^-	2573	230 (10) ns	218(36) ns
^{117}Sn			
$3/2^+$	158	0.279 (9) ns	0.265 (15) ns

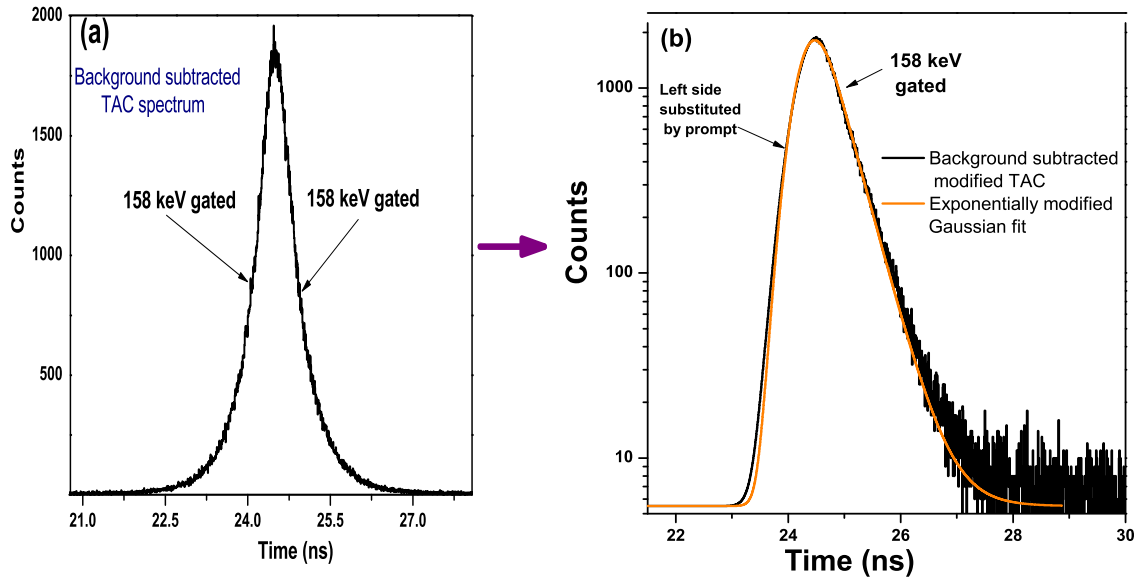


Figure 2.21: Fig. (a) shows delayed TAC curve, that is built up by gating 158 keV in both the detectors. Fig. (b) 158 keV-158 keV TAC is modified by substituting the left part by the prompt Gaussian distribution obtained from Fig. 2.20 (b). It is fitted with exponentially modified Gaussian distribution.

2.5 Theoretical interpretation: Shell model calculations

To interpret the experimental data and understand the microscopic structure of the low-lying states of $^{117,118}\text{Sn}$, a large basis shell model (LBSM) calculation has been performed using OXBASH [46] code. The low-lying excitation spectra of Sn isotopes involve neutron excitations within the shell model orbitals between $N = 50$ and 82 . Among the five relevant neutron orbitals, the intruder negative parity relatively high-spin $1h_{11/2}$ orbit is mostly responsible for the occurrence of low-lying isomers in Sn isotopes with $N \geq 64$.

For Sn isotopes with around 64 neutrons (N), the number of valence neutron particle (hole) is ≈ 14 -16 above (below) the $N=50$ (82) core. Therefore, unrestricted calculations are difficult, if not impossible. The low-lying states in

these mid-shell Sn isotopes are expected to be collective involving the mixing of multiple configurations. However, the isomers in these nuclei, have much purer structure. In even Sn isotope, 7^- has dominant neutron configuration $\nu 1h_{11/2}^{-1}2d_{3/2}^{-1}$, whereas the excitation of 5^- can be described by either $\nu 1h_{11/2}^{-1}2d_{3/2}^{-1}$ or $\nu 1h_{11/2}^{-1}3s_{1/2}^{-1}$ configurations. Therefore, these states can be interpreted by putting reasonable restrictions in the model space. More details about theoretical calculations to study the structure of Sn isotopes and comparison of results with available interactions will be discussed in Chapter 5 of this thesis.

2.5.1 Model space and interaction

In the calculation, *sn100pn* interaction [47] with the *gdsh* model space ($1g_{7/2}$, $2d_{5/2}$, $2d_{3/2}$, $3s_{1/2}$, $1h_{11/2}$ for both neutrons and protons) and ^{100}Sn core have been used. The residual interaction is derived from CD-Bonn renormalized G matrix. For *sn100pn* interaction, the neutron single particle energies (spe) are -10.6089, -10.2893, -8.7167, -8.6944, -8.8152 (all in MeV) for $\nu 1g_{7/2}$, $\nu 2d_{5/2}$, $\nu 2d_{3/2}$, $\nu 3s_{1/2}$ and $\nu 1h_{11/2}$ orbits, respectively.

2.5.2 Truncation schemes

Three different truncation schemes, namely SM1, SM2, SM3 are used. In SM1, $\nu 1g_{7/2}$ and $\nu 2d_{5/2}$ orbitals are kept fully occupied with 8 and 6 neutrons, respectively. Only $\nu 1g_{7/2}$ orbital is fully occupied in the case of SM2, with no other restrictions in other orbitals. In SM3 truncation scheme, $\nu 1g_{7/2}$ orbital is

restricted to have minimum 4 and maximum 8 neutrons, $\nu 2d_{5/2}$ orbital with 2 (minimum) - 6 (maximum) neutrons and $\nu 1h_{11/2}$ orbital with 0 (minimum) - 2 (maximum) neutrons.

2.5.3 Results and Discussions

The calculated excitation energies for ^{118}Sn with different truncations are tabulated in Table 2.6. Due to severe restriction, none of the results reproduce experimental data well. The results with SM2 truncation have reproduced the relative ordering and the energy values of the levels observed in the present experiment much better than the other two.

Therefore, the transition probability for 7^- to 5^- transition in ^{118}Sn are calculated with SM2 truncation. The theoretical $B(E2: 7^- \rightarrow 5^-) = 3.091 e^2\text{fm}^4$ matches reasonably well with experimental data $2.200 (103) e^2\text{fm}^4$ [18] ($2.325 (554) e^2\text{fm}^4$ from present study) with $e_n^{eff} = 0.15e$.

Table 2.6: Comparison of experimental excitation energy of ^{118}Sn with sn100pn for different restrictions.

Spin (I^π)	Excitation energy (MeV)			
	Expt.	sn100pn		
		SM1	SM2	SM3
0^+	0	0	0	0
2^+	1.229	0.754	0.989	0.626
4^+	2.28	1.203	1.660	1.157
5^-	2.324	1.351	1.856	3.069
7^-	2.574	1.378	2.069	2.773

With same SM2 restriction, the excitation energy and transition rates for ^{117}Sn have been calculated. Although, the $3/2^+$ state has been predicted at 149

keV, reasonably well compared to the $1/2^+$ (experimental energy 158 keV), the $11/2^-$ state is underpredicted severely by around 580 keV, and it appears as the ground state. Therefore, experimental γ - energies are considered while calculating the lifetimes of the excited states from theoretical reduced transition probabilities. The branching ratio of 314.48 keV state and lifetimes of excited states are compared with experimental data (Table 2.7).

The neutron effective charge $e_n^{eff} = 0.15e$ is low compared to the standard values adopted in this region. However, for the truncation scheme (SM2), this low value reproduces the experimental data reasonably well for both $^{117,118}\text{Sn}$.

Table 2.7: Comparison of different experimental observables [18] related to transition rates for ^{117}Sn with theoretically calculated (sn100pn) values using SM2 restrictions. $B(E\lambda)$ is expressed in $e^2\text{fm}^{2\lambda}$ and $B(M\lambda)$ is expressed in $\mu_n^2\text{fm}^{2\lambda-2}$. The neutron effective charges and g factors are mentioned in footnote.

$J_i \rightarrow J_f$	Observables		
	Type	Expt.	Theory
$3/2^+ \rightarrow 1/2^+$	$B(M1)^1$	0.0306	0.0327
	$B(E2)^2$	3.09 (40)	2.315
	$\delta(E2/M1)$	0.0133 (8)	0.0118
	Half-life ($T_{1/2}$) in ps	279 (9), 265 (15) ³	263.89
$11/2^- \rightarrow 3/2^+$	$B(M4)^4$	$1.22 (72) \times 10^5$	1.43×10^5
$11/2^- \rightarrow 1/2^+$	$B(E5)^2$	$2.44 (65) \times 10^4$	3.84×10^4
$11/2^-$	Branching for M4	99%	99%
$11/2^-$	Half-life ($T_{1/2}$) in d	13.91 (3)	11.41

$${}^1g_s^{eff} = g_s^{free}; {}^2e_n^{eff} = 0.15e; {}^3\text{Present work}; {}^4g_s^{eff} = 0.5 g_s^{free}.$$

2.6 Summary

The decay studies of $^{117g,118m}\text{Sb}$, have been performed with high resolution γ -spectroscopy setup. The decay half-lives of $^{117g,118m}\text{Sb}$ have been remeasured.

The present study has modified the adopted level scheme of ^{118}Sn by excluding the 984 keV γ -ray from the scheme and revised the feeding intensity of the 2573 keV state to 100%. The origins of the unplaced γ -rays reported earlier have been identified. It is conclusively proven that none of them belongs to the excitation spectrum of ^{118}Sn . The remeasured lifetimes of the isomeric levels agree reasonably well with reported values.

The half-life of $3/2_1^+$ state of ^{117}Sn which is measured using two independent experimental setups agree reasonably well with the values available in the literature.

The shell model calculations have been done with different truncation schemes to interpret the experimental results. Although the results failed to reproduce the experimental excitation energies satisfactorily in both the nuclei, the calculated transition rates agree reasonably well with the data. A low $e_n^{eff} = 0.15e$ has been found to reproduce the B(E2) values for both the nuclei.

CHAPTER 3

Development of analysis method of digital data

3.1 Introduction

In general, the decay half-life of a radioactive nucleus is a key observable in nuclear spectroscopy. It contains invaluable information about the overlapped states between which the transition occurs. In the case of unstable nuclei, the role played by the β -decay holds immense importance. In that way, the half-life related to this weak interaction offers a wealth of information about the internal structure of the nuclei. One of the crucial tests of different theoretical nuclear models is an accurate reproduction of lifetime related to either β -decay or EM transition.

In order to measure the activities of short-lived radionuclide, in general, the activation method (appendix [A](#)) is used as discussed in earlier chapter. The target is irradiated over a specific period of time depending on the estimated half-lives. After that, the decay data are accumulated to extract the half-life. For such a situation, where a set of nuclei have been populated with unknown half-lives. They may span over a range from a few seconds to days order

or higher. In that case, choosing the time step for counting is very difficult. Motivated by this fact, we made an attempt to remeasure the lifetimes those are too long for measurement using in-beam electronic technique and also too short for off-beam methods. For determination of half-lives of different orders, we have relied on the digital approaches utilizing the time-stamped data.

The advancement of digital technology is rapidly substituting the analog technology in different areas of nuclear spectroscopic experiments [48, 49]. This progression is offering a different level of flexibility in nuclear spectrometry that was previously very difficult or impossible to implement with the use of standard analog techniques. In recent timing, digital pulse processing (DPP) provides not only improved technical performance and reliability but also its compact physical dimension and low weight carry extra credit. The aim of signal processing (both in analog and digital process) in nuclear spectroscopic experiment is to extract information regarding the radiation or radiation-induced events. These signals contain not only information about the energy deposited by the particle, but also about the time of arrival and the shape information depending upon the experiment.

In previous chapter, the decay half-lives of $^{117g,118m}\text{Sb}$ have been determined from the data using analog system. In this current chapter, we have remeasured these decay half-lives of employing digital techniques from an off-beam data. To demonstrate the effectiveness of such digital technique, decay data have also been stored continuously from in-beam to off-beam condition during an in-beam experiment. Utilizing such singles time-stamped data, the half-lives

of different orders ranging from few minutes to several hours (for Ga isotopes) have been estimated. Moreover, the data have been employed to note minute details of beam profile in an in-beam experiment. Also, one can discriminate the in-beam and off beam situations by analysing such digital data.

3.2 Digital Electronics

Over last few decades, fast analog to digital converters (ADCs), field programmable gate arrays (FPGAs), and digital signal processors (DSPs) are evolving very rapidly. Taking advantages of these, the output of the detector can be processed in digitizer just after the pre-amplification. DPP is mainly dependent on high speed digitizer and digital filter. The signals are continuously sampled and saved in a compressed data format that contains the relevant informations. The readout or simple digital processing is mainly processed by the algorithms implemented in FPGAs, such as digital filters, pulse shapers, constant fraction discriminators etc. These algorithms are used to evaluate several necessary parameters like amplitude or the arrival time of the pulse. In digitizer, pulse shaping is done by means of a trapezoid filter or ‘moving window de-convolution filter’ [50]. This filter can transform an input signal (typically an exponential pulse) produced by charge sensitive pre-amplifier into a trapezoidal pulse. Generally, the amplitude of the pulse is measured from the pulse height difference between the flat top of trapezoid and signal base-line. It is the measure of the energy released by the particle in the detector. In this digital approach,

the pulse height analysis algorithm has the power to perform online base-line restoration, ballistic effect correction and to manage the pile-up of online data acquisition [51]. In order to determine the arrival time of the pulse, the second derivative of the input signal is calculated. This is performed by an algorithm implemented on FPGA and this replaces the usage of traditional CFD. The purpose of this derivation is to eliminate low frequency fluctuations associated with the baseline part. From a simple calculation, one can understand that the zero crossing of the pulse is independent of pulse amplitude and depends on only the time constant of the pulse. So, the zero crossing of second derivative of the input signal estimates the accurate time arrival with an uncertainty equivalent to one unit of sampling time [52]. Whenever the pulse crosses the base-line, a trigger signal is generated that produces a time-stamp.

3.3 Experimental Details

Two distinctive experiments have been carried out at Variable Energy Cyclotron Centre (VECC), Kolkata. The first experiment is related to the spectroscopic study of long-lived isotopes populated via irradiation. The second one is an in-beam study.

Both of the experiments have been performed using an HPGe detector to detect the γ -rays decaying from the excited target. It is coupled with a CAEN 5780M desktop digitizer [51] to acquire the experimental information. This 14 bit (16 k channel and 100 MS/s sampling rate) digitizer module is equipped with

two high voltage power supplies (± 5 kV, $300 \mu\text{A}$) along with two preamplifier power supplies (± 12 V, ± 24 V). Therefore, no separate module has been used in purpose of biasing and pre-amplification. It is well furnished with DPP-PHA (Digital Pulse Processing-Pulse Height Analyzer) firmware. This feature enables the digitizer to evaluate precise energy and timing information [51]. The data has been collected with the use of *MC²analyzer* software [53].

The data exchange and control command between the computer and the digitizer was carried out by attaching the USB cable. This can be done also by connecting a CAEN proprietary optical bus. The maximum transfer rate can be 30 MB/s while using USB cable. This can be increased up to a transfer rate of 80 MB/s [51] via optical link, that offers Daisy-chain capability. In the present work, using USB cable is the most convenient choice.

3.4 Methodology

In this current study, the lifetime or the half-life has been estimated following two different methods: from the decay of parent nucleus as well as from the growth of daughter nucleus.

In general, the half-life of the parent nucleus is generally described by the equation,

$$N_m^t = N_m^0 e^{-\lambda_m t}, \quad (3.1)$$

where N_m^0 is the number of parent nuclei present at $t = 0$ and λ_m is the decay constant. This equation can also be expressed as,

$$\ln(N_m^t) = \ln(N_m^0) - \lambda_m t, \quad (3.2)$$

Now, by taking derivative of the equation 3.1, the equation reduces to be,

$$\frac{dN_m^t}{dt} = -\lambda_m N_m^0 e^{-\lambda_m t}. \quad (3.3)$$

Now, if the decay half-life of daughter nucleus is much much larger than that of parent i.e. the daughter nucleus is stable, the growth curve of daughter nuclei can also be generated from the data. The number of daughter nuclei produced will increase exponentially and will attain a saturation value following the relation,

$$N_d^t = N_m^0 [1 - \exp(-\lambda_m t)], \quad (3.4)$$

where, N_d^t is the number of daughter nuclei produced in time t . The half-life can be obtained either from the decay of the parent nuclei or growth of the daughter nuclei. The variation of count rate as a function of time is obtained in case of the decay of parent nucleus. Whereas, the growth of the daughter nucleus can be generated by accumulating the data with increasing the time-bin of digitizer time-stamped data.

In case of decay of parent nucleus, the count rates are determined at different instants of time. Let us assume that T_o is the starting time of the measurement. Now, the next measurements are done at an interval of time ΔT . Now,

the spectra corresponding to T_o to $T_o + \Delta T$, $T_o + \Delta T$ to $T_o + 2\Delta T$ and so on are generated. The peak area of the most intense γ -transitions are plotted (as a function of time). However, in the current study, we have adopted a different technique to analyse the time-stamped data. The interval of time is not kept uniform for all instants. Rather, we have kept the number of total decay events to be constant and it leads to a variation in time bin. This can be explained as: at the starting time of the decay, the rate is faster as 3 million (3M say) events can decay within a smaller time. Whereas, after some time, to accumulate the same number of decay events, a longer time bin is needed. Lastly, the count rate i.e. the number of decay events per unit time of accumulation is calculated and plotted with time to estimate the half-life.

The decay constant is evaluated by fitting the curve with an exponential function (equation 3.3) with minimum χ^2 value to have the best fitting. One can also estimate half-life by fitting the curve [i.e. $\ln(\text{count rates})$ vs time] with a linear function (equation 3.2). The slope of that function is the measure of the half-life.

In case of building the growth curve of the daughter nucleus, for an equal number of decay events associated with different intervals of time ΔT are summed up consecutively such that spectra are generated for (*i.e.* T_o to $T_o + \Delta T$, T_o to $T_o + \Delta T + \Delta T'$...) time period. As the decay time increases, the area under the γ -peak of interest increases by reducing the statistical error.

3.5 Data analysis procedure

The ‘LIST mode’ data format of digital acquisition system is beneficial as it offers sequential list of the events with measured parameters depending upon the requirement of the experiment. In the present work, energies and corresponding timing information are key parameters. List mode data can be saved either in ‘Binary’ format or in ‘ASCII’ format. In our case, we have saved the data in ‘ASCII’ format. In this format, the list mode file typically contains two columns. The first column describes the arrival time of different pulses (multiplying by 10 ns) w.r.t. the Digitiser and the second one represents the number proportional to the pulse amplitude (Energy parameter). Now, selecting a particular time window, the list mode data can be handled using a simple computer program. Using *MATLAB* [54] software package, the list mode file is analysed to generate histograms of energies within specific time windows. The whole algorithm is defined in few steps described below.

3.5.1 Details about the data sorting program

The main issue of handling the data file is particularly the size of the file, which is typical of the order of few GBs as it contains information of several hours. Importing the whole data into the array is very time consuming. One can handle such files using ‘datastore’ function in *MATLAB*.

As stated earlier, in the list mode data, there are two columns : the first column gives information about the timing and the second represents the energy

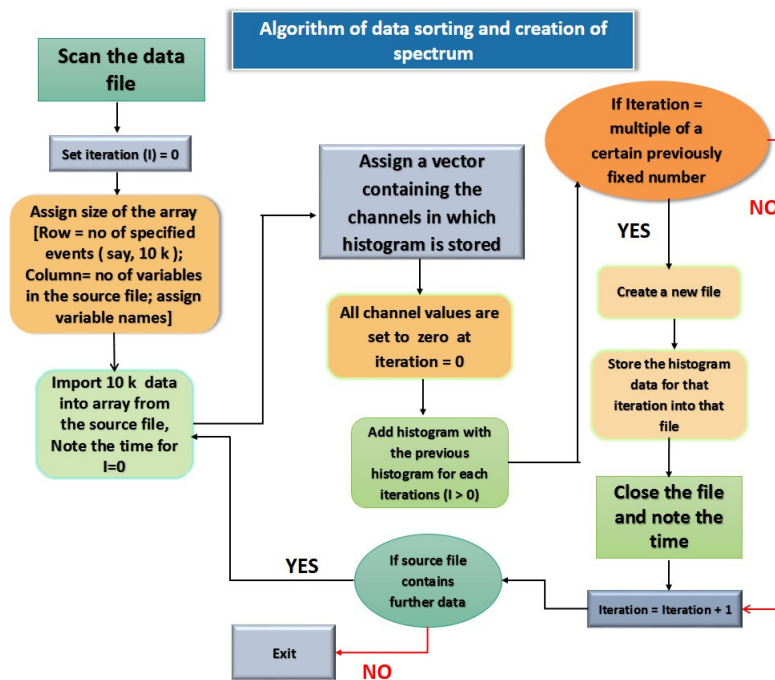


Figure 3.1: Schematic flow chart of data sorting program.

parameters. For the first set of data, the time-stamp corresponding to the first event is noted. Then, the set of data is plotted as a histogram to generate a specified spectrum. This histogram is stored in an array. If the data file contains further information, then again a set of 10k events are replaced in the data array. The corresponding histogram is now added with the previous histogram. The stored histogram is written in the file only after a specific number of iteration to be fixed by the user. Otherwise, a large number of spectra will be created that is too difficult to handle. Additionally, the time-stamp of the last event of that histogram is also noted to have the timing information. A flow chart of the program is given in Fig. 3.1.

The number of the generated spectrum can also be reduced by increasing the number of events in per event bin. Hence briefly, the large data streams are split into different parts by specifying a particular event bin such as 10k events. If

the time resolution of the digitizer is 10 ns and then, for 10 k events, the time interval should correspond to at least of 100 μ s. The exact time interval is estimated by calculating the difference between the last and first time-stamp of each set of 10k events. Therefore, depending on the predicted half-life, event bin for saving consecutive decay spectra can be chosen appropriately to follow the decay.

Ideally, event binning must be chosen in such a way that reasonably good statistics remains even at the end of the decay. But, this reduces the total number of data points in the decay curve. On the contrary, the smaller event binning results into larger number of data points. A larger number of data points results into a better fit in some cases. However, it also increases the error in the area of each peak. So, optimization has to be done depending on the source strength and half-life.

At last, the energy histogram is plotted with a specified number of event-bin. In order to find the area under the photopeak from the generated spectrum, *INGAS ORT* [32] software has been used.

3.6 Specific experiment details

3.6.1 Offline experiment:

Similar to the experiment described in chapter 2, ^{117g}Sb ($T_{1/2} = 2.80$ (1) h), ^{118m}Sb ($T_{1/2} = 5.00$ (5) h) and ^{117m}Sn ($T_{1/2} = 14.00$ (5) d) have been populated via the irradiation of ^{nat}In target of thickness 54 μm by α -beam of 32 MeV

energy at VECC, Kolkata. In this particular case, the experimental setup (referred as Setup II in section 2.3.3) contains only HPGe detector 80% relative efficiency and CAEN 5780M Digitizer.

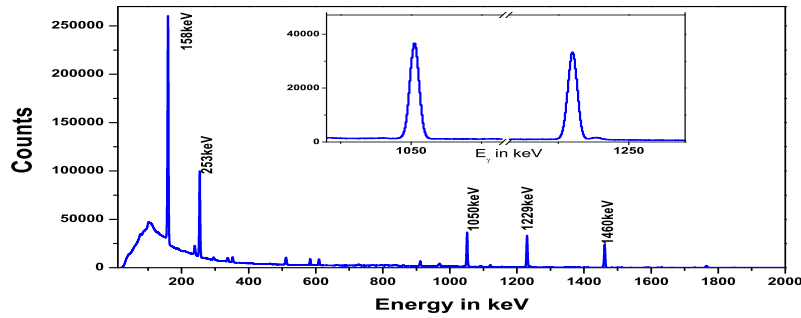


Figure 3.2: Typical gamma spectrum of irradiated natural Indium by 32 MeV α -beam collected using HPGe detector.

3.6.1.1 ^{118m}Sb : 8^- state

To estimate the decay half-life of ^{118m}Sb ($I^\pi=8^-$ state), the decay of ^{118m}Sb (parent) and the growth of ^{118}Sn (daughter) have been plotted for different γ -transition of daughter nucleus taking two different event bins such as 3M and 1M as shown in Fig. 3.3 and Fig. 3.4. The results obtained using different binning and techniques are tabulated in the table 3.1 and compared with the previous results [18].

3.6.1.1.1 Discussion It is noted that in case of smaller bin (for 1M event bin in this case), more number of data points are present in the curve. That results in the better fitting. Eventually, the error related to this area (statistical one) also increases. Hence, to have a more accurate result, optimization is always necessary. As shown in the table 3.1, the half-lives estimated employing the

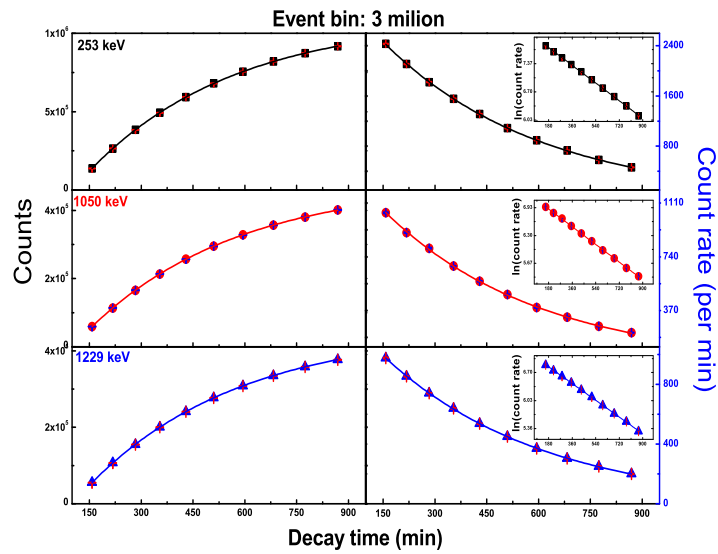


Figure 3.3: (Left) Growth curves of daughter nucleus for different intense γ -transitions. (Right) Decay of parent nucleus is followed to evaluate decay half-life. In Inset $\ln(\text{count rate})$ are shown. The spectra are generated time with 3M event bin.

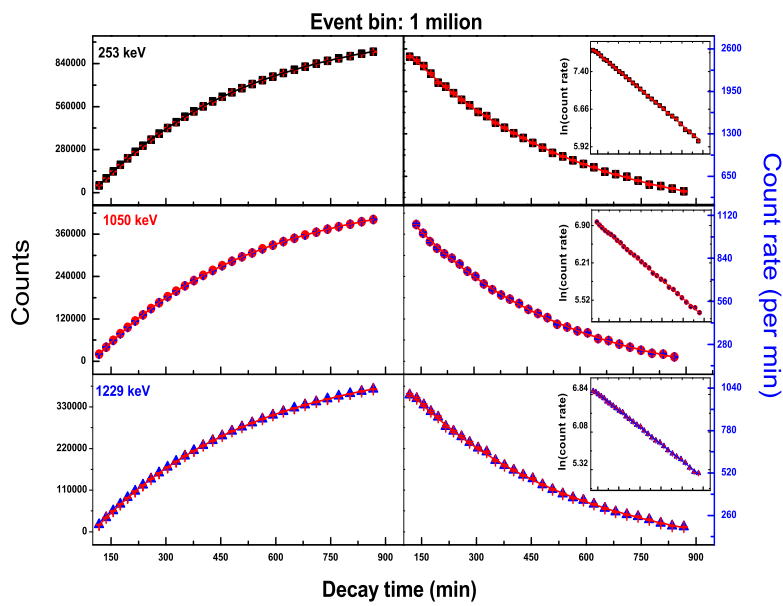


Figure 3.4: Same as Fig. 3.3. The spectra are generated with 1M event bin.

Table 3.1: Decay half-life of ^{118m}Sb (8^- state) determined from time-evolution of different intense γ -transitions. The errors are reported within parentheses.

		Half-life (h)					
Energy (keV)	Prev. [18]	Present					
		Decay				Growth	
		Eqn. (3.3)		Linear ¹		Eqn. (3.4)	
		BIN1 ²	BIN2 ³	BIN1 ²	BIN2 ³	BIN1 ²	BIN2 ³
253		5.28 (5)	5.25 (8)	4.95 (3)	4.92 (2)	4.87 (1)	4.87 (1)
1050	5.00 (2)	5.18 (15)	5.07 (10)	5.20 (3)	5.03 (2)	5.00 (2)	4.99 (1)
1229		5.36 (7)	5.23(10)	5.17 (2)	5.11 (2)	5.04 (1)	5.04 (1)

¹Determined from logarithmic plot.

²Event Bin of 3M.

³Event Bin of 1M.

both techniques reasonably agree with the previous results [18]. Among them, the results obtained from the growth curve show a better match. Also, change of size in event bin shows less effect in case of the half-lives determined from growth curves.

3.6.1.2 ^{117g}Sb : $5/2^+$ state

The decay half life of ^{117g}Sb of $5/2^+$ state has been evaluated having event bin 3M following the technique described above. Similar to section 2.4.1.2, the time evolution of 158 keV is plotted to estimate the decay half-life as shown in Fig. 3.5. The half-life is estimated to be 2.98 (1) h. Hence, the weighted average of different experimental setup is found out to be 2.97 (2) h.

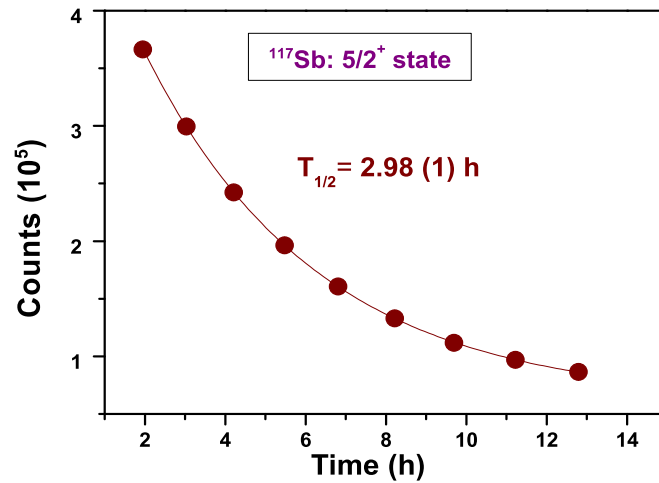


Figure 3.5: The decay curve of ^{117}Sb following the time evolution of 158 keV γ -transition from the digital data acquired by CAEN 5780 Digitiser.

3.6.2 In-beam experiment:

This in-beam experiment has also been carried out at VECC, Kolkata, using proton beam of energy 10 MeV produced from the K-130 cyclotron. The target was ^{nat}Zn . The isotopic composition of natural Zn is tabulated in Table 3.2. In this experiment, by fusion evaporation reaction, the compound nuclei, *viz.*, $^{65,67,68,69,71}\text{Ga}$ isotopes have been populated. The main deexcitation processes proceeded by emitting one neutron and the populated nuclei are $^{64,66,67,68,70}\text{Ga}$. These nuclei were eventually decayed and the most dominant decay channel at that particular energy was (p,n) reaction. The details of the decay modes have been enlisted in table 3.2.

Hence, this particular data set of data includes information about the several radioactive decays of nuclei, of which half-lives span from minutes to days. The experimental data have been acquired encompassing in-beam condition to

Table 3.2: Isotopic composition of natural Zn and decay modes, half-lives and most intense decay γ -ray energies of short-lived Ga isotopes produced by (p,n) reaction. The masses (shown in first column) are same for target Zn (Z=30) isotopes and corresponding Ga (Z=31) isotopes produced as reaction products [18].

Mass (A)	Abundance ^{nat} Zn [25]	Decay mode	Half-life (Error)	γ -ray Energy (keV) Intensity(%) ¹
64	49.17%	EC	2.627 min (12)	991.51 ² (46)
66	27.73%	EC	9.49 h (3)	1039.22 ² (37)
67	4.04%	EC	3.2617 d (5)	93.31 ² (72.57)
68	18.45%	EC	67.71 min (8)	1077.34 ² (3.22)
70	0.61%	β^- (99.59%) EC (0.41%)	21.14 min (5)	1039.51 ³ (0.65)

¹Absolute intensity per 100 decays.

²From corresponding Zn isotopes via electron capture (EC)-decay.

³From ⁷⁰Ge via β^- -decay.

beam off situation (Fig. 3.6). Data have been collected using a 20% relative efficiency HPGe detector with the same CAEN 5780 digitizer.

In the Fig. 3.7, the variations of count rate with the time for the strong gamma rays associated with the transition from 2⁺ to 0⁺ for ^{64,66,68}Zn isotopes i.e. 991 keV, 1039 keV, 1077 keV respectively are shown. These γ -transitions, which are emitted from excited levels of ^{nat}Zn isotopes have been populated from two different feeding channels. Those are ^{nat}Zn(p,p')^{64,66,68}Zn reactions and decay of ^{64,66,68}Ga isotopes populated via ^{nat}Zn(p,n) reactions.

Now, the 1014 keV γ -ray is the de-exciting gamma transition of ²⁷Al from the first excited state to its ground state. It is populated via (p,p') reaction. This material is one of the component of the target holder and other accessories of the chamber. Hence, the count rate of this particular transition can be a parameter related to the measure of misalignment of the beam. Four gamma-

ray energies 991, 1039, 1077 and 1014 keV are arising from the excited states of ^{64}Zn , ^{66}Zn , ^{68}Zn and ^{27}Al (target frame material) respectively. It is observed that, the total area under the photo-peaks remain almost constant in the BEAM-ON interval. As no drastic change has been made in beam parameters (like current intensity or beam focusing etc.), such an observation is expected [55].

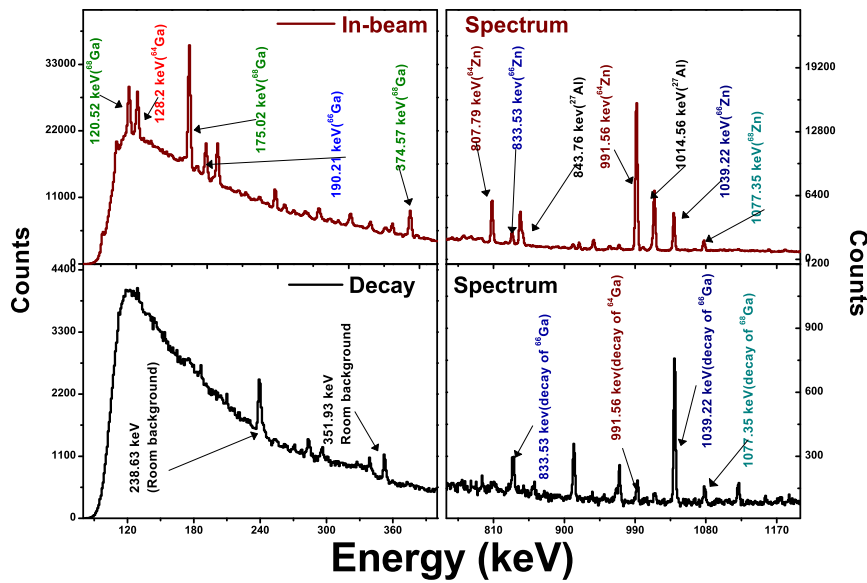


Figure 3.6: Typical in-beam and decay spectra of natural Zn target bombarded by 10 MeV proton projectile.

In general, for a specific target material, the absolute area under the photo-peak depends on the various parameters such as, the abundance of the isotope, cross-section of the reaction at the particular energy and also on beam specifications (like, beam current incident on the target). Additionally, a variation of count rate of characteristic γ -s emitted from the elements present in the target holder or in accessories of the chamber can provide information about the beam tuning and focusing. Such minute details as a function of time can be obtained from such time-stamped data. A significant increase in the count of real peaks along with the beam-generated background peaks will be the signature

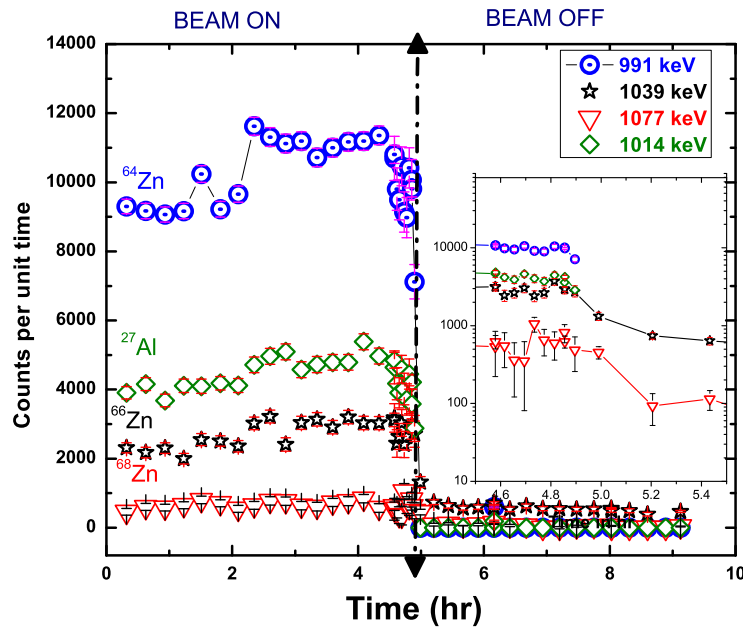


Figure 3.7: Variation of peak area of different γ -transitions with time. The dash-dotted line differentiates between the beam-on and beam-off situations. The inset shows a zoom-in of transition time.

of an increase in beam intensity. Whereas, on the other hand, the increment in these background peaks compared to the real peaks, will be an indication of poor beam focusing. In the BEAM-OFF condition, data has been accumulated for 4 hours. It is noted that since the half-life of ^{64}Ga is nearly order of a few minutes, it decays more sharply than other nuclei ($^{66,68}\text{Ga}$) as shown in Fig. 3.7. It is also observed that the area of 1014 keV goes to zero as a prompt effect of beam stop. The $^{27}\text{Al}(p,n)$ reaction product ^{27}Si has a half-life of 4.15 sec, which can also populate 1014 keV γ ray. However, the ^{27}Si decays 99.7% to the ground state of ^{27}Al . Thus, 1014 keV γ -ray is originating mostly from the in-beam excitation. From Fig. 3.7, the yield curves of different Zn isotopes follow the abundance ratio in ^{nat}Zn . Their de-excitation γ s have nearly the same energy, which ensures that the detector efficiency will be

Table 3.3: Measured half-lives of short-lived Ga isotopes.

Mass	Energy (keV)	Half-life	
		Adopted [18]	Present work
64	991	2.627 ± 0.012 min	2.61 ± 0.15 min
66	1039	9.49 ± 0.03 h	9.82 ± 1.18 h
68	1077	67.71 ± 0.08 min	70.30 ± 3.57 min

nearly the same. The half-lives of $^{64,66,68}\text{Ga}$ isotopes have been determined from the BEAM-OFF portion of the curve in Fig. 3.7. We have not analysed the decay data of $^{67,70}\text{Ga}$ due to long half-life (^{67}Ga : 3.2617(5) d) and weak decay γ -transition (^{70}Ga : 1039.51 keV). The growth curve of ^{64}Ga , is plotted for 12 minutes, beyond which it saturates as shown in Fig. 3.8. The growth curves (Fig. 3.8) of $^{66,68}\text{Ga}$ have been plotted up to ~ 4 h (depending upon the availability of data). The extracted half-lives of $^{64,66,68}\text{Ga}$ are tabulated in Table 3.3. The calculated half-lives match reasonably well (Table 3.3) with the previously values [18]. A large deviation of calculated half-life from the reported value is seen in case of ^{66}Ga . It must be due to the time restriction of our data (as only $\simeq 4$ h data was available). Moreover, for ^{68}Ga , relatively lower abundance of ^{68}Zn (see, Table 3.2) in natural Zn and lower intensity of the decay γ -ray have increased the error in the result.

3.7 Discussion

In this current work, the digital data saved in List mode have been used to estimate decay half-life of several different nuclei. The data have been sorted for a constant number of event bin instead of constant time interval. The half-

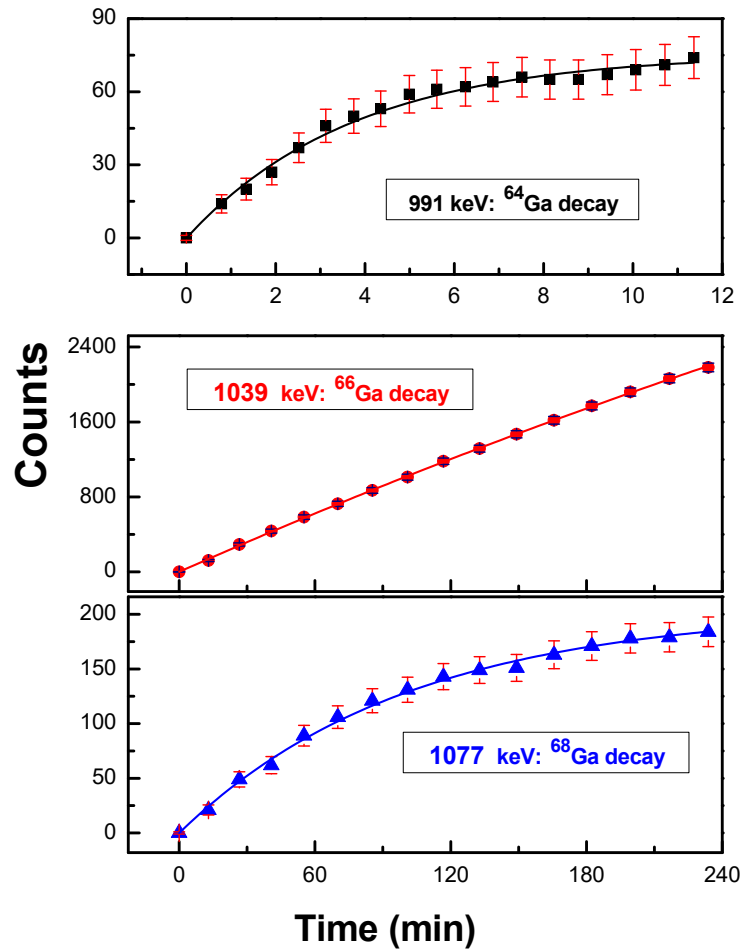


Figure 3.8: Growth curves of Zn isotopes ($^{64,66,68}\text{Zn}$) generated from decay gamma rays of corresponding radioactive Ga isotopes .

lives have been remeasured from the decay of parent nucleus as well as growth of daughter nucleus. The obtained results show a very good agreement with previously reported value. It is observed that, building up growth of curve is more advantageous, as a relatively small statistical error is induced by resulting in better fit. Whereas, the count rate gradually decreases as the time evolves in case of decay curve. Moreover, with different event bins, the applied technique has been discussed.

CHAPTER 4

Detector development and characterisation

4.1 Introduction

Recently, low-cost photodiodes and similar devices are utilized as radiation detectors, especially in high energy physics experiments, nuclear radiation-based medical diagnostic tools, security surveillance monitors, etc.

A photodiode that can be used for nuclear radiation detection should have its capacitance low, decreasing with increasing reverse bias. However, as the reverse bias increases, the leakage/dark current increases. Thus the choice of a suitable photodiode for radiation detection needs a careful measurement of the capacitance and leakage current with increasing reverse bias to select the optimum operating reverse voltage for that particular variety of the diode. The low capacitances (\approx pF) of these detectors demand the usage of properly impedance matched preamplifiers.

When radiation interacts with the detector material, energy deposition results in the creation of electron-hole pairs. In the case of semiconductors, the main advantage is low ionization energy. On average, 3.6 eV is needed at 300

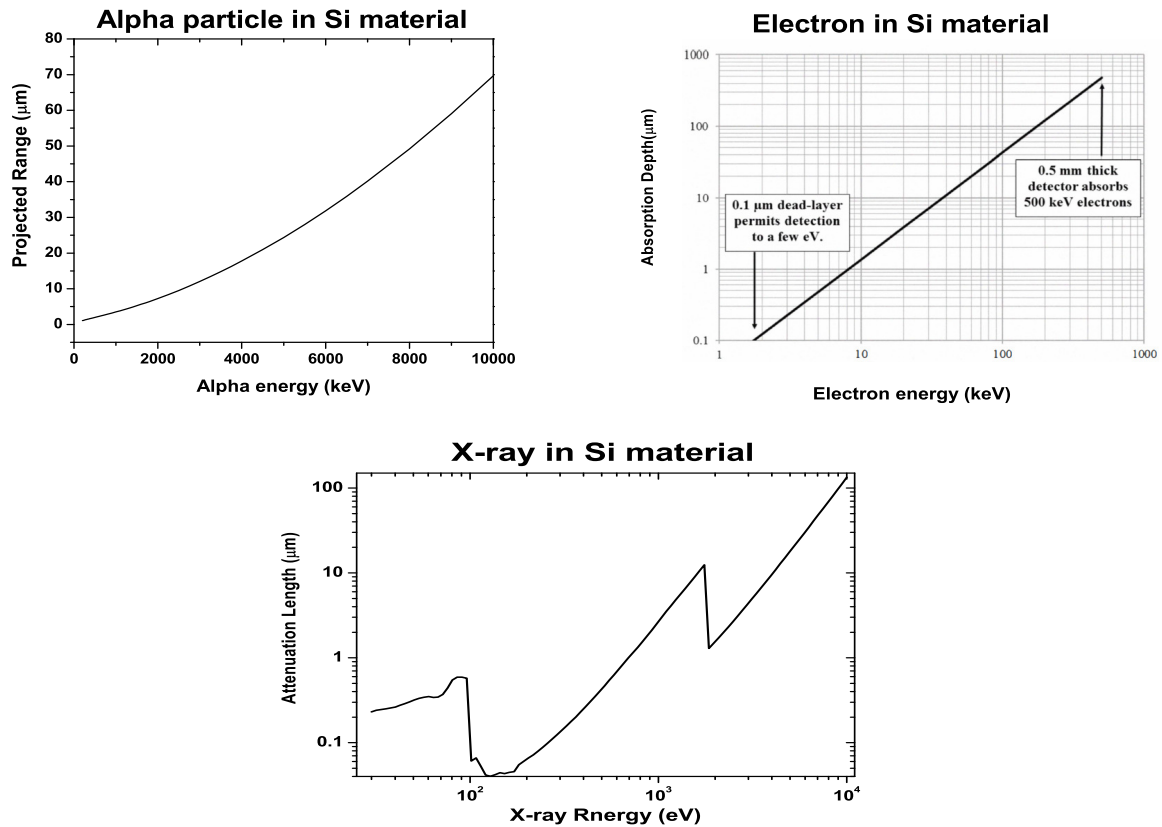


Figure 4.1: (Top) Left: The variation of projected range is plotted with alpha energy [56]. Right: The variation of absorption depth with the electron energy is presented. The plot has been taken from Ref. [57]. (Bottom) The variation of attenuation length is plotted with X-ray energy calculated from Ref. [58].)

K to create one electron-hole pair in silicon (Si). The number of generated electron-hole pairs is proportional to the particle's energy, provided the energy is entirely deposited in the active volume of the detector.

For charged particles such as alpha particles or heavy ions, the energy is dissipated along a linear track [59]. The path-length is dependent on the type and energy of the incident particle. In contrast, beta particles' tracks are non-linear as their ranges are long due to relatively smaller mass. Additionally, electron penetration is also dependent on the thickness of the detector layer.

X-ray and gamma rays are electromagnetic radiations that interact with mat-

ter via three processes depending upon their energies. The interaction processes are photoelectric effect, Compton scattering, and pair production. For Si with $Z=14$, the cross-section of photoelectric absorption dominates in the lower energy range, < 50 keV in the soft X-ray region. In this process, the full energy of the X-ray photon is transmitted to electron-hole pairs. These pairs are the source of electric current under the applied electric field. For $E > 50$ keV, the Compton scattering process dominates. In this process, a fraction of X-ray or gamma-ray energy is transmitted to the electron-hole pairs. The partial deposition of energy reduces the detection efficiency. The efficiency depends on incident radiation's energy and varies as a function of Si wafer thickness [60]. For a thick Si wafer, the efficiency of the detection of higher energy photon improves.

It is well known that Si-photodiodes and PIN diodes can efficiently detect alpha particles and low energy x-rays and gamma rays. The detection efficiency of a 300-micron silicon wafer falls off sharply beyond ten keV. The diodes have an intrinsic capacitance, which reduces with increasing reverse voltage to reach the maximum depletion zone to give the best detection efficiency. However, an increase in reverse bias voltage results in a higher leakage current. This dark leakage current is temperature-dependent and increases due to thermal excitation. Dark current approximately doubles for every 10 °C increase in temperature. The dark current dramatically reduces by cooling the detector diode.

4.2 Photodiodes used in the present project

In the present work, two different types of photodiodes are used: PN photodiode and PIN photodiode. PN photodiode is a two-terminal device, in which one side is doped with p-type and another with n-type of material. In PIN diodes, an extra intrinsic layer (highly resistive) is present between the heavily doped p-type and n-type material. This extra layer benefits high-speed response with reverse bias operation. PIN type diodes offer additional advantages due to their thicker depletion layer, enabling it to be hit more number of particles or photons.

In this study, we have used photodiodes that are cost-effective relative to standard commercial ones. We started our testing procedures with BPW34 (from VISHAY Semiconductors), BPW21 (from OSRAM Opto Semiconductors), VTB8440BH (from Excelitas Technologies), and BEL-Si PIN diode (from Bharat Electronics Limited). Typical optical and electrical characteristics of these diodes can be found from their data-sheets [61–64]. The important functional parameters have been specified in Fig. 4.2.

4.3 Characteristics of photodiodes and PIN diodes used

4.3.1 Capacitance

Junction capacitance is the parameter that is related to the response speed of the photodiode. When the depletion region is fully depleted, the capacitance

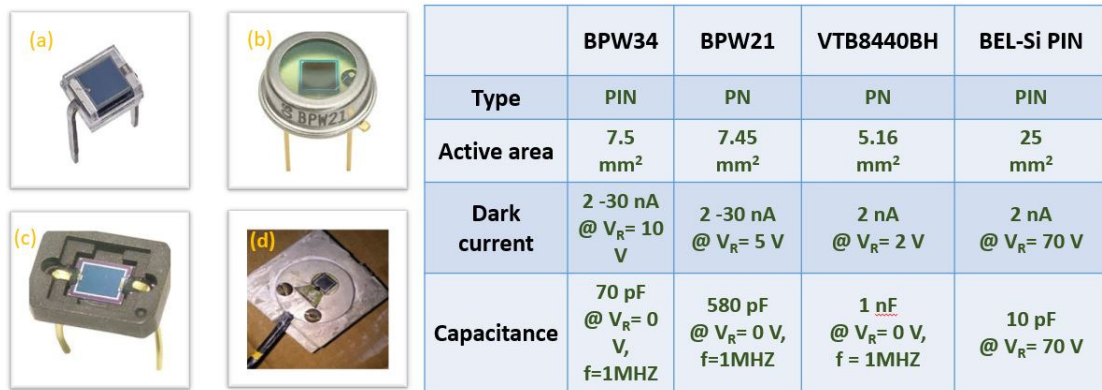


Figure 4.2: The pictures of different diode detectors [(a) BPW24, (b) BPW21, (c) VTB8440BH, (d) BEL Si(PIN) diode] are shown along with their specification details provided by the manufacturer.

is minimum. It is essential to keep the capacitance as low as possible. With increasing reverse bias, the width of the depletion layer increases, resulting in lower capacitance.

At the Advanced Material Science Lab of SINP, using Agilent E4980A LCR meter, we successfully measured the range of different photodiodes’ capacitance with reverse voltages shown in Fig. 4.3.

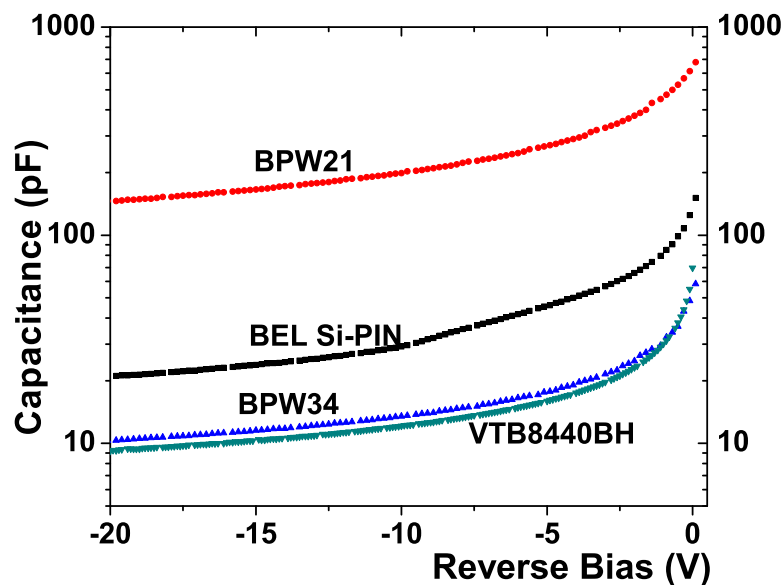


Figure 4.3: Variation of capacitance with varying reverse voltage for different diode detectors measured using Agilent LCR meter.

4.3.2 Dark Current

Dark current or leakage current is a relatively small but finite amount of current, which flows in a photodiode even when no radiation / charged particle is incident on the diode. This current increases with the detector volume and surface area [65]. Photodiodes have temperature-dependent leakage current, which increases with temperature and reverse bias.

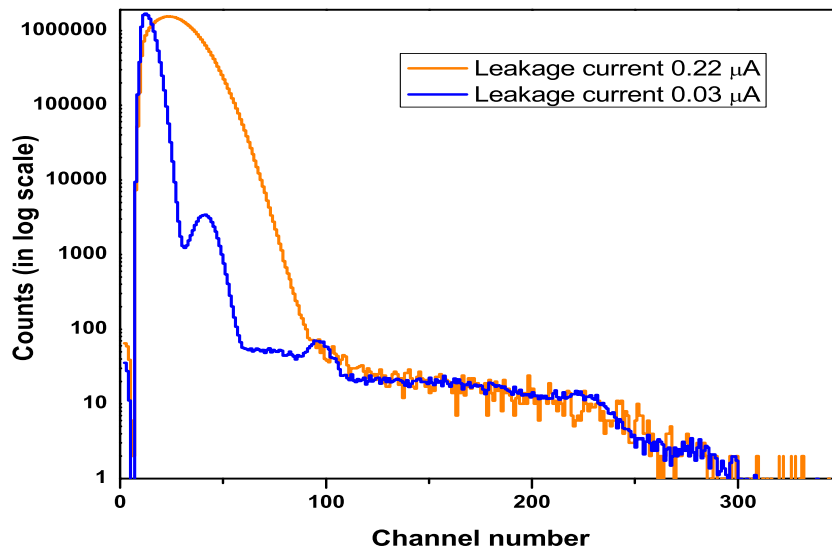


Figure 4.4: The spectra of ^{133}Ba are compared for two different leakage current of BEL-Si(PIN) diode.

The detector leakage current is an indicator of stability. For a steady condition, the value of the leakage current will be stable. Any abrupt increase of leakage current indicates deterioration of detector performance in terms of worsening of energy resolution. The leakage current of the detector increases significantly after it is continuously used for a long time. It is evident from the spectrum of ^{133}Ba acquired by a Si-PIN diode, as displayed in Fig. 4.4. The

leakage current increases from $0.03 \mu\text{A}$ to $0.22 \mu\text{A}$, after the BEL - Si PIN diode is continuously used.

Detector cooling is one of the practical solutions to minimize leakage current. Under such circumstances, cooling the detector is essential.

4.4 Other essential details and electronics

4.4.1 Mounting of the detector

The photodiodes' flying leads are mounted either with 50 ohm BNC or Lemo connector. However, the parasitic capacitance and inductance can pose a serious problem while extracting signals from the wire. Thus mounting the photodiode is very critical and needs special attention. Moreover, in some cases, for detecting the charged particles, the protective window of the diode has to be removed carefully.

4.4.2 Preamplifier

A preamplifier is needed to generate an equivalent voltage pulse for processing the electron-hole pairs generated by the charged particle's interaction in the depletion region of the photodiode. The preamplifier's function is to extract the signal from the detector without affecting the signal's quality. It has to be kept as close as possible to the detector. It acts as an impedance matching component (to have high impedance to the detector side and low impedance on the amplifier side). Most frequently, a charged sensitive preamplifier (CSP)

is used. The sensitivity or the limitation is determined from the signal to noise ratio.

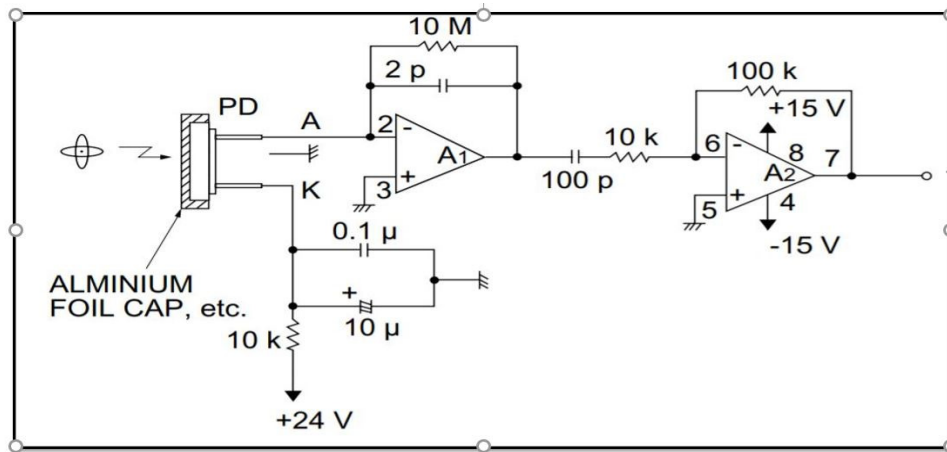


Figure 4.5: The schematic diagram of preamplifier circuit following circuit provided in Ref. [66].

Usually, commercially available preamplifiers are quite costly. So, we intended to develop a suitable preamplifier that would be cost-effective. We have fabricated a preamplifier in the breadboard following the circuit given in the Ref. [66]. The first part of the circuit acts as a current integrator or charge amplifier having a high impedance. In this circuit, we have used LF442 (JFET operational amplifier) as A_1 shown in Fig. 4.5. It is connected with a high impedance of $10\text{ M}\Omega$ resistor. It converts the charge accumulated into a proportional voltage output. Further, it is fed to an inverting amplifier that amplifies its pulse height. We tested the preamplifier with a laser light source and a radioactive source (α source: ^{241}Am).

The preamp pulses are shown in Fig. 4.6. It is observed that the output pulse height for input from the laser source is very high and saturates at 10 V. Whereas, for input from an alpha source emitting alpha particles of 5.486

MeV, the output amplitude is around 150 mV. The laser source emits photons of a single frequency. An intense ray of visible light is emitted from the laser source. The output pulses from individual photons overlap with each other, resulting in a higher output voltage.

However, for a standard laboratory radioactive source, the number of alpha particles/X-rays/gamma-rays emitted is much less. Thus output corresponding to each incident particle/photon is distinct, and the pulse height becomes directly proportional to the energy of the incident particle/photon (Fig. 4.6). Therefore, for X-rays (< 50 keV), the output pulse is comparable to the electronic noise and can not be distinguished from the noise.

Despite some success, we could not reduce increasing stray capacitance,

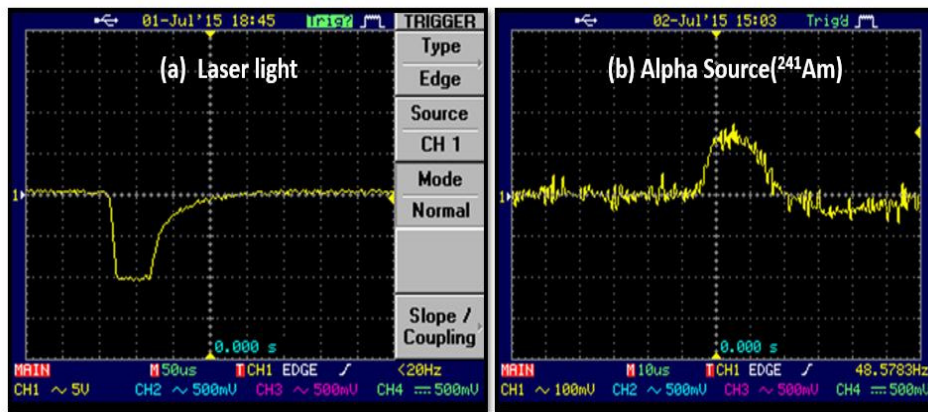


Figure 4.6: The pulses of (a) laser light, (b) alpha source ^{241}Am are processed using the preamplifier fabricated in a breadboard.

which induces electrical noise with this particular circuit. We have tried to improve the circuit but eventually failed. Therefore, we have to opt for commercially available preamplifiers like ORTEC 142A, 142B, 142IH e.t.c.

4.4.3 Cooling the detector

The thermal excitation of the electron-hole pair is one of the sources of leakage current. The leakage current is strongly dependent upon the temperature (T) following the equation [67],

$$I_{LC} \propto T^2 e^{-\frac{E_g}{2\kappa_B T}}, \quad (4.1)$$

where I_{LC} is leakage current, T represents the temperature, E_g denotes the bandgap energy (1.12 eV for Si), κ_B is the Boltzmann constant.

Hence, to improve the detector performance, cooling the detector is immensely important. In general, the Si Photodiode or PIN diode detector can be used at average room temperature during the heavy-charged particle detection. However, for an X-ray or low energy photon, the number of e-h generated is minimal and almost comparable to the electronic noise level. In such a case, the detector's noise level should be reduced as far as possible to distinguish real pulses from the noise. To maintain such a condition, the cooling of the detector is essential. In this present work, an effort has been made to cool these diodes using different arrangements.

4.4.3.1 Liquid N₂ cooling arrangements

Most of the semiconductor gamma detectors require cooling at cryogenic temperature. The standard method is to cool using liquid Nitrogen (LN₂). We also used LN₂ for cooling. The detector was placed on a metallic plate at the top

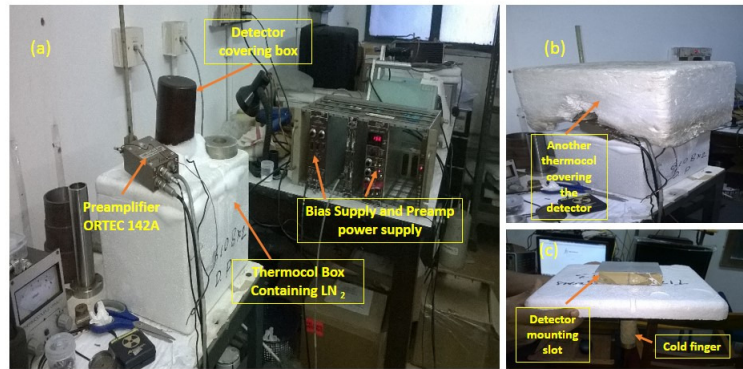


Figure 4.7: Different parts of the cooling arrangement using liquid N_2 are shown in the figure.

of a thermocol box filled with LN_2 . A copper (Cu) rod, attached to the plate, was dipped in LN_2 . The rod worked as a cold finger to cool the detector. The detector was covered by another box (as shown in Fig. 4.7) to minimize the background light.

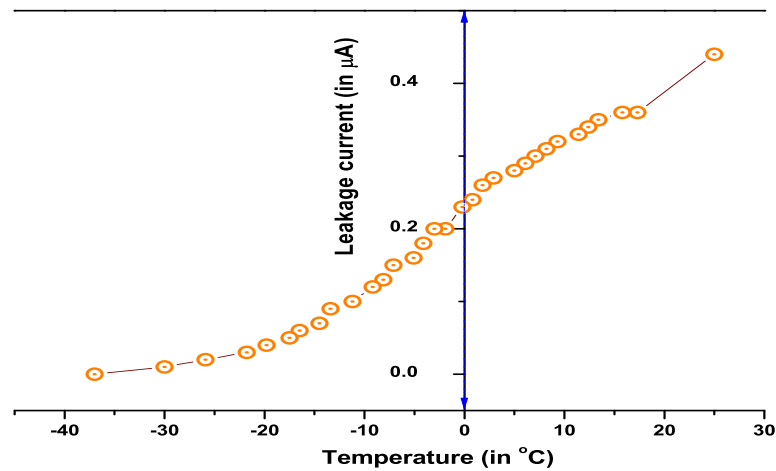


Figure 4.8: The variation of leakage current of BEL-Si(PIN) diode is plotted with decreasing temperature.

The effect of cooling is quite dramatic and is demonstrated from the variation of leakage current with temperature (Fig. 4.8). The leakage current decreases from $0.45 \mu A$ to $0 \mu A$, when the PIN diode is cooled from room temperature to $-37^\circ C$.

4.4.3.2 Development of cooling device: Using Thermoelectric cooler

We procured cheap and compact thermoelectric coolers (TEC), TEC 12706, from the local market. These coolers work following the basic principle of the Peltier effect. The internal structure of a TEC consists of an array of semiconductor pellets connected in series electrically [68]. But, thermally, they are arranged in parallel to achieve maximum heat transfer between the hot and cold sides. When the required voltage is applied across the device, one of the sides becomes hot, and the other side becomes colder, maintaining a constant temperature difference (60°C in the present) between the two sides. From the data-sheet provided by the manufacturer, we can get an estimate of the temperature difference that can be created between the two sides for a given operating voltage. Thus to achieve a low temperature at the cold side, one has to dissipate the heat generated at the hot side as quickly as possible.

The Thermoelectric cooler TEC-12706 (manufactured by Hebei IT Co. LTD [69]) draws a maximum of 6 Amp current. An ATX 24 pin switched-mode power supply (SMPS, which is frequently used in the motherboard of a computer) or a high – current power supply provided 12V with the required current specification to the device. The TEC has been mounted with thermal paste on a suitable heat sink to ensure good contact between the sink and TEC module. The different arrangements have been tested with the heat sink to dissipate the hot side's heat most effectively (Fig. 4.9).

In the first arrangement, (Fig. 4.9(a)) the TEC is connected with a high

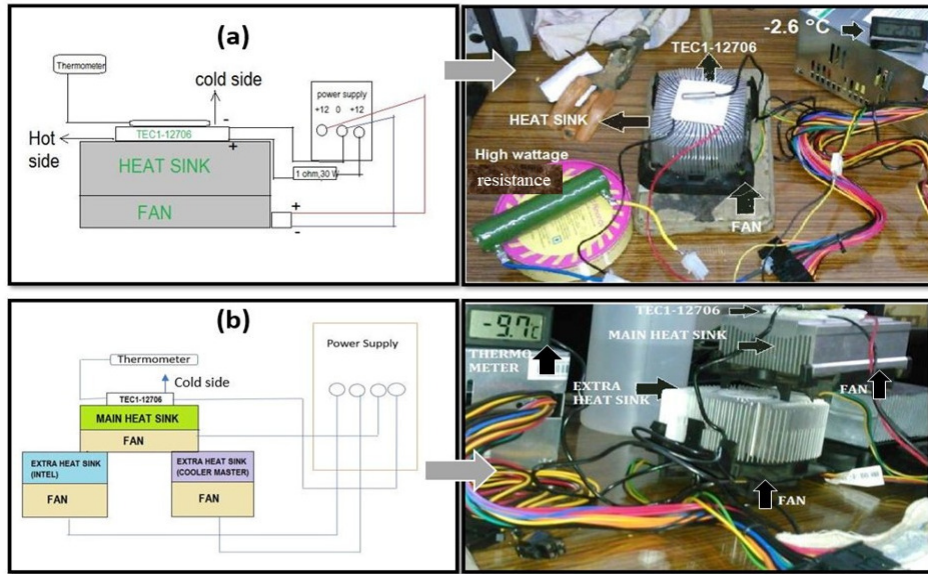


Figure 4.9: Different arrangements using TEC are shown along with the schematic diagram.

wattage low resistance (1Ω , 30 W) in series to control the current. The minimum temperature reached using this setup is around -2.6°C (when the ambient temperature was $\sim 30^{\circ}\text{C}$). However, with this arrangement, we could not maintain a low temperature over a long time.

In the second arrangement, three heat sinks were used, and the TEC was placed in the middle heat sink, as shown in Fig. 4.9 (b). The minimum temperature for the cold side reached -9.7°C . However, it was challenging to maintain a stable minimum temperature.

Later, this second arrangement was used to cool the photodiodes. However, the mechanical vibration of the fan attached to the heat sink introduced additional noise in the response of the detector. Therefore, cooling with TEC in combination with heat sink and fan was discarded.

Finally, continuous water flow worked perfectly for TEC cooling. The TEC

was mounted on a hollow metallic box with thermal paste. A small pump was used to continuously flow water in that metallic box (Fig. 4.18). The TEC's hot side temperature started to come down very quickly, increasing the device's efficiency. The improvement of using this cooling arrangement is evident from Fig. 4.10. The noise level reduces w.r.t two other peaks as shown in Fig. 4.10 (b).

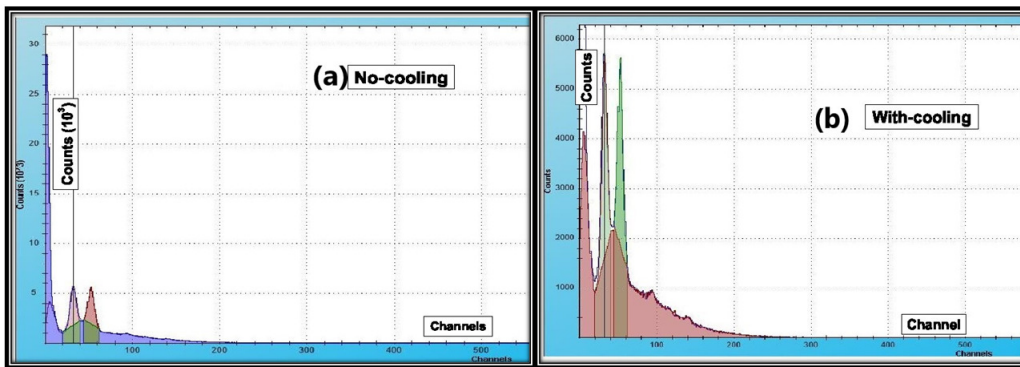


Figure 4.10: The spectrum is acquired (a) without / (b) with using the TEC using water-cooling arrangement. The noise level reduces by a significant amount using the water-cooled TEC arrangement.

4.5 Detection of nuclear radiation

We have used the photodiodes of a few varieties, as discussed before, for the detection of electrons, alpha particles, and X-ray, as well as gamma photons.

4.5.1 Detection of alpha particles

To test the detectors, we have started with the alpha sources. As the energy of the alpha particles emitted by radioactive sources available in our laboratory is around 5 MeV, the pulse heights are expected to be above the noise level, even without cooling the detector. Moreover, the intrinsic detection efficiency

is around 100% for charged particles of moderate energy.

Two different alpha sources are used. One is $^{241}_{95}\text{Am}$ ($T_{1/2}=432.2(6)$ y) that emit alpha particles of energy 5.486 MeV (84.8% [18]). The second source, namely triple line alpha source, is a mixed one that consists of three different radioactive isotopes $^{239}_{94}\text{Pu}$ ($T_{1/2}=24,100(30)$ y; $E_{\alpha}=5.156$ MeV), $^{241}_{95}\text{Am}$, and $^{244}_{96}\text{Cm}$ ($T_{1/2}=18.11$ (3) y; $E_{\alpha}=5.805$ MeV).

The detector is coupled with a preamplifier (ORTEC 142A or 142B or 142IH, depending on the photodiode's capacitance) with bias supplied from 710 Quad 1 kV Bias Supply or an equivalent unit. The detector and the source are placed in the vacuum chamber to minimize the alpha particles' energy loss. The output of the preamplifier is amplified by a spectroscopic amplifier (ORTEC 576) for pulse processing. It is later sent to a multi-channel analyzer (FAST COMPTEC- MPA) for analog to digital conversion. The block diagram is shown in Fig. 4.11.

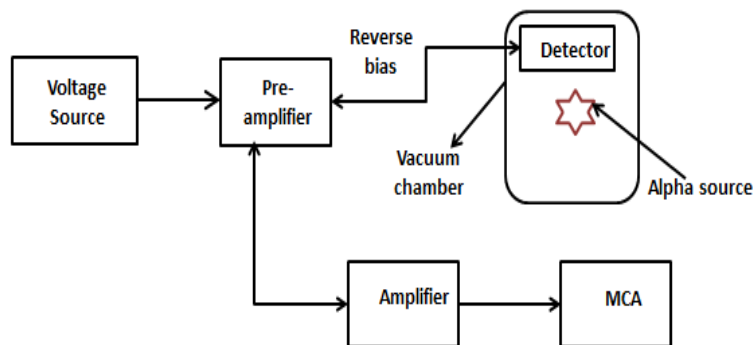


Figure 4.11: The block diagram of the experimental setup used in the alpha particle detection experiment.

For different photodiodes, the preamplifier pulses corresponding to alpha par-

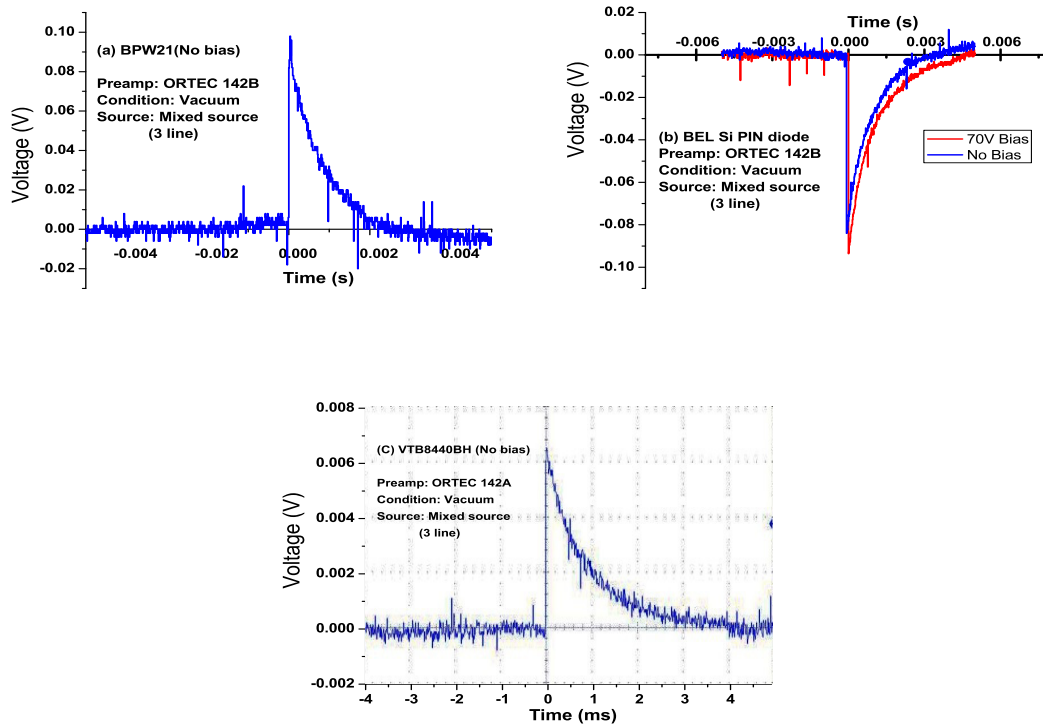


Figure 4.12: The preamp pulses of different diode detectors, such as (a) BPW21, (b) BEL-Si (PIN), (c) VTB8440BH are displayed. The experimental conditions are also mentioned.

Figure 4.12 [70]. BPW34 photodiode contains a protective layer (window), which can not be removed easily. This window is thick enough to stop ≈ 5 MeV alphas. So, we could not use this diode in alpha detection. For BPW21, the protective window of the diode encasing was removed for alpha detection. The Bharat Electronics Limited (BEL) Si-PIN diode is windowless. The preamplifier pulses from BPW21 and Si-PIN are relatively high for incident alphas, even without any applied reverse bias.

4.5.1.1 BPW21

For BPW21, the preamplifier output became noisy with reverse bias. So, the data were acquired under no bias condition. It is well known that energy res-

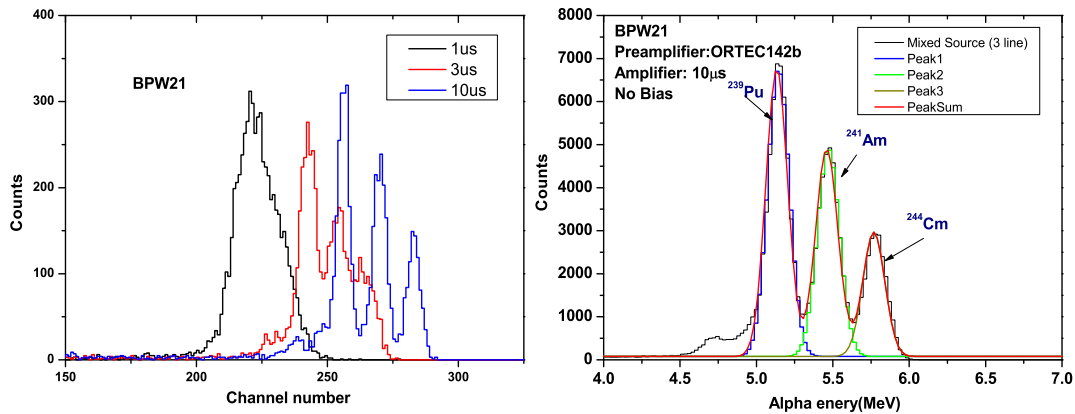


Figure 4.13: (Left) The alpha spectra are obtained by BPW21 detector using triple line alpha sources for different shaping times of spectroscopic amplifier. (Right) The alpha spectra for amplifier shaping time $10 \mu\text{s}$.

olution is also dependent on the shaping time of the amplifier. The optimum value of shaping time of the amplifier was obtained to improve the detector performance.

Under the same condition, spectra are acquired with varying shaping times of the amplifier. With increasing shaping time, the resolution of the energy peak improved. For the lowest shaping time ($1 \mu\text{s}$), the three intense peaks of the triple line source could not be resolved. With increasing shaping time, peaks are resolved. The best resolution is achieved for $10 \mu\text{s}$ [Fig. 4.13 (left)].

4.5.1.2 BEL Si-PIN diode

Similarly, the amplifier's optimum shaping time was selected by acquiring data for triple-line source with varying shaping times with the BEL-Si diode detector. The best resolution of the detector was obtained for $3 \mu\text{s}$ shaping time (Fig. 4.14 [left panel]). The Si pin diode is operated with reverse bias voltage -70

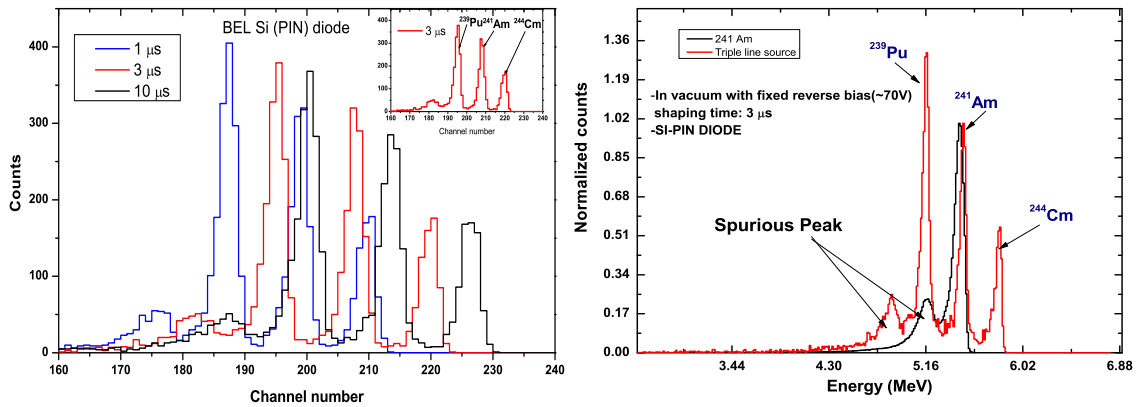


Figure 4.14: (Left) The alpha spectra are obtained by BEL-Si (PIN) diode detector using triple-line alpha source to set optimum shaping time of spectroscopic amplifier. The inset shows the alpha spectrum having the best resolution obtained for $3 \mu\text{s}$. (Right) The alpha spectra are compared for single -line and triple -line sources under the same experimental condition.

V as specified in the manufacturer's data-sheet. The diode is placed within a vacuum chamber, and data are acquired for $3 \mu\text{s}$ shaping time of the amplifier. The data have been acquired with both the alpha sources (single and triple line). The spectrum was calibrated using the triple-line source.

The data obtained with ^{241}Am showed an additional low intense peak apart from that at 5.486 MeV. The triple line source normalized spectrum has been overlapped in the same plot (Fig. 4.14 right) to identify the small peak. Interestingly, the three-line source spectrum also contains a low-intensity additional peak at the left side of the alpha peaks. Such spurious peaks have also been reported in the alpha spectra acquired by a similar detector [71]. One of the significant reasons is incomplete charge collection in the diode's edges, or the fluctuation in energy loss through the dead layer [65]. Such partial energy loss can also broaden the peak, resulting in the deterioration of the detector's energy resolution.

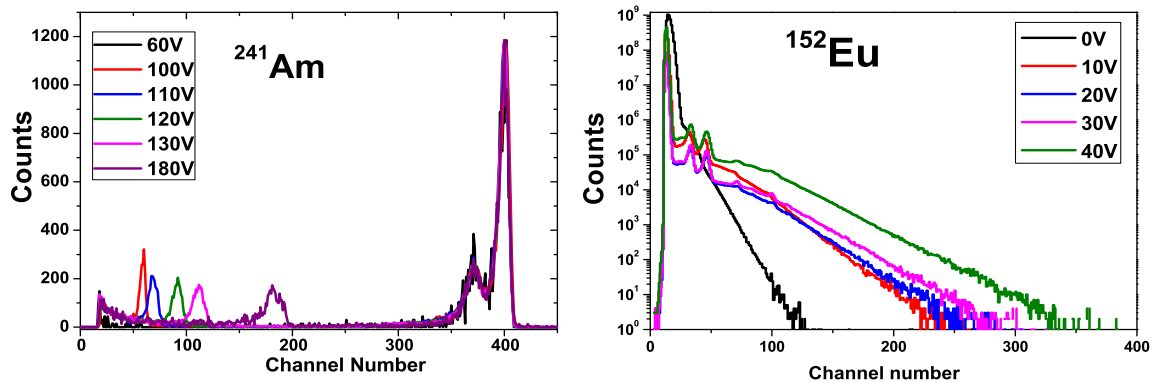


Figure 4.15: The effect of reverse bias is shown in figure using two different radioactive sources: (a) ^{241}Am and (b) ^{152}Eu .

4.5.2 Detection of X-rays, gamma rays and conversion electrons

We only worked with the BEL Si- PIN diodes to detect X-rays, gamma rays, and conversion electrons. In general, Si PIN diodes are capable of detecting X-ray and gamma photons. But the detection efficiency sharply decreases with the thickness of Si. For a wafer of $300\ \mu\text{m}$, the detection efficiency reduces drastically for γ -rays beyond 10 keV. The best detection efficiency can be achieved by increasing the reverse voltage that induces a more extensive depletion layer. The neutral gamma rays interact differently with the medium than charged particles. Whereas alpha and beta (electrons) beam transfer their energy to the medium gradually, gamma (X-ray) photons may or may not fully or partially transfer their energies. Thus gamma (X-ray) photons have longer penetration depths. Therefore, the Si-PIN diode also needs higher reverse bias voltage to improve detection efficiency for even low energy X-rays. However, it introduces a higher leakage current and induces more thermal noise. For the detection of X-rays, cooling of the detector becomes essential.

Several sets of data were acquired by varying the reverse bias to identify the optimum voltage for detecting alphas and X-rays. For 3 μ s shaping time, the reverse bias is varied from 60 to 180 V [72]. It is observed that for the single-line source (^{241}Am), the alpha peak remains fixed at one position (Fig. 4.15). However, on the low energy side, a low-intensity peak varied its position (moving to higher channels) with increasing bias voltage. We know that ^{241}Am source also emits internal conversion electrons (associated with 59 keV excitation energy), several low energy X-rays, and a low energy 59 keV gamma-ray. The moving peak may correspond to them. Increasing bias voltage increases the depletion layer's width. It improves charge collection, which increases the pulse height. However, for alpha particles, the depletion depth corresponding to the lowest voltage is sufficient to stop it entirely.

The effect of increasing reverse bias with ^{152}Eu source is evident in Fig.4.15. The beta ray continuum distribution becomes more prominent for higher bias voltage.

4.5.2.1 Identifying electron and X-ray peaks in the spectrum

To allow conversion electrons from the source to reach our detector, we prepared a ^{152}Eu source covered with a thin X-ray Mylar foil to minimize the energy (intensity) loss of electrons (low energy X-rays).

Three distinct strong peaks with two weaker ones are seen in the spectrum. These are X-ray and conversion electron peaks. The first peak corresponds to 40 keV X-ray. The other peaks correspond to conversion electrons of energies

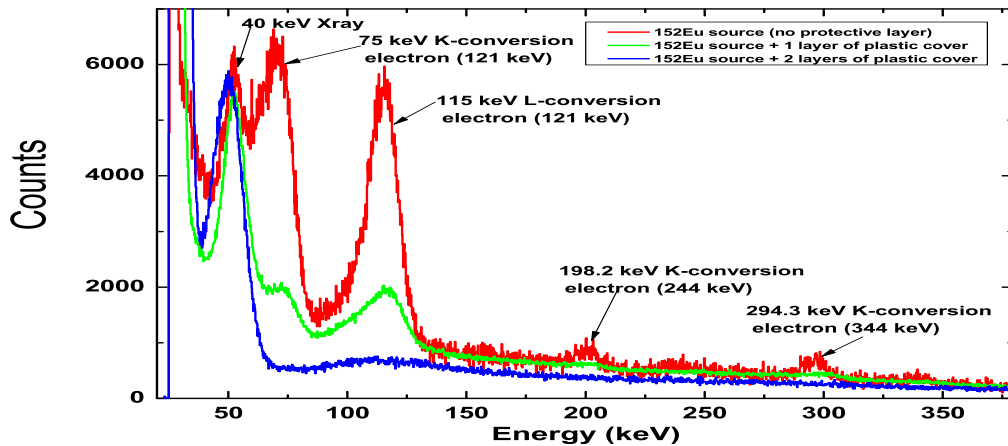


Figure 4.16: The X-ray - conversion electron spectra of ^{152}Eu is compared with increasing thickness of protective layer (plastic) around the source mentioned in legend.

75 keV (K-conversion electron energy of 121 keV), 115 keV (L conversion electron peak of 121 keV), 198 keV (K-conversion electron energy of 244 keV), and 294 keV (K-conversion electron energy of 344 keV) [73, 74].

Data have been acquired by introducing a plastic cover on the source to check the correctness of identification of the peaks. With the increasing number of plastic layers, the intensities of the electron peaks significantly reduced. However, the X-ray peak height at 40 keV remain almost constant (Fig. 4.16). For two layers of plastic, the peak heights of 75 keV and 115 keV are reduced drastically. These peaks correspond to the conversion electron peaks. Thus, we can successfully distinguish between the X-ray and conversion electron peaks.

4.5.2.2 Gamma-ray detection using cooling arrangement

In general, detecting gamma-ray with energy more than 50 keV using this Si (PIN) detector is difficult, if not impossible. Because of the relatively low atomic number, the photoelectric effect's cross-section ($\propto Z^5$) is significantly

low. However, the detection efficiency improved by increasing the applied reverse bias after cooling the detector.

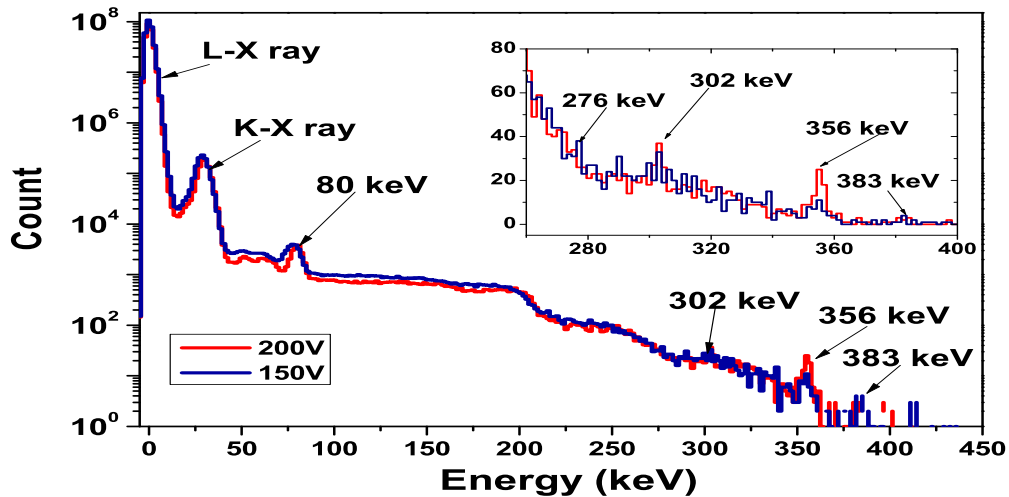


Figure 4.17: The spectra are obtained using standard radioactive sources of ^{133}Ba at different reverse voltages applied on BEL Si(PIN) diode.

The arrangement of LN_2 cooling (Fig. 4.7) as discussed before has been utilized. The data have been acquired with ^{133}Ba radioactive source. To prevent the detection of conversion electrons, the source was covered with thick plastic. The data have been taken for two different reverse bias voltages (150 V and 200 V, respectively). By cooling the detector, the spectrum improved. In Fig. 4.17, the reduction in detection efficiency with increasing energy is also evident. However, with cooling, bias could be increased to 200V, and the peaks at higher energies also become more prominent.

4.5.2.3 Coincidence study between conversion electrons and γ -rays in ^{152}Eu

The correlation between the conversion electrons and γ -rays of ^{152}Eu has been tested. The experimental set up is arranged very compactly in a compact geom-

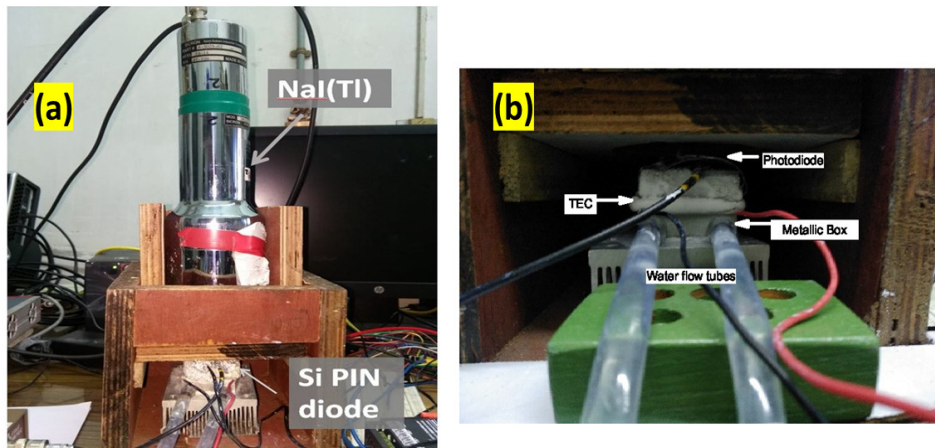


Figure 4.18: (a) The setup for the measurement of internal conversion coefficient. (b) The zoomed view of the setup with PIN diode cooled with TEC using by water-cooling arrangement.

etry without a vacuum chamber. To detect gamma rays a $3'' \times 3''$ NaI(Tl) has been used [75] (as shown in Fig. 4.18). The conversion electrons are detected using Si-PIN diode which is cooled by a TEC using water-cooling arrangement as discussed before. The data have been collected using CAEN 5780M desktop digitizer. The digitizer provided the detector bias. The Si (PIN) diode has been used with ORTEC 142B preamplifier. The output of the NaI(Tl) detector is fed directly to the digitizer for further pulse processing.

The standard ^{152}Eu ($T_{1/2} = 13.517(14)$ y) is one of the suitable sources that decays to two different daughter nuclei via beta decay. It disintegrates to ^{152}Sm via electron capture (72.1%) and positron emission process (0.0027%). Whereas, rest (27.9%) of the decay is followed by β^- emission to ^{152}Gd [18]. A simplified decay scheme is shown in Fig. 4.20(a).

The data were collected in ‘LIST’ mode format to store the energy as well as temporal information with a coincidence window of $2.5 \mu\text{s}$. The data have

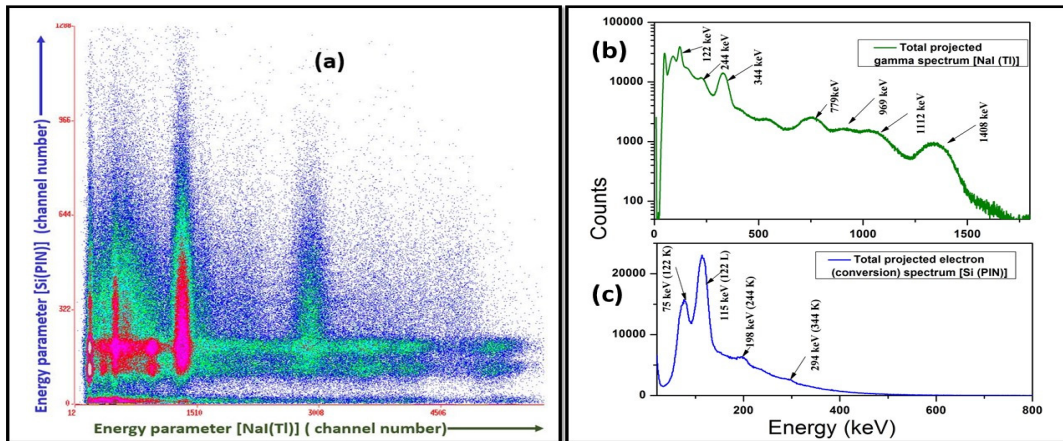


Figure 4.19: (a) The two dimensional energy matrix constructed from coincidence data using *LAMPS* software is represented. The X axis corresponds to the energy spectrum of gamma transitions detected by NaI(Tl). The Y axis represents the electron energy spectrum obtained using Si(PIN) diode. (b) The total projection of gamma spectrum is shown (green colour) indicating the peaks of ^{152}Eu . (c) The internal conversion spectrum is illustrated showing the energy of the peaks.

been further analysed in *LAMPS* software to build up two dimensional matrix (E_{elec} vs. E_{γ} matrix). The two - dimensional matrix is displayed in Fig. 4.19 (a). The projection of the matrix is also shown in 4.19 (b,c). In the full projection of gamma spectrum, intense γ -peaks of ^{152}Eu are identified. Likewise, the conversion electron peaks of 122 keV, 245 keV and 344 keV are also detected. 75 keV and 115 keV correspond to the K and L conversion electron peaks, respectively. Whereas, 198 keV, 294 keV is coming as K shell conversion electron contribution of 245 keV and 344 keV, respectively. In the gated spectrum of 244 keV, the projected electron spectrum shows the peaks at 75 keV and at 115 keV. It is expected as 122 keV is in coincidence with 244 keV. Whereas, 344 keV gamma gated spectrum shows a continuum spectrum. It is noted that 344 keV is the most intense transition of excited ^{152}Gd , that is populated via β^{-} decay. Hence, this continuum spectrum is justified. In the current study, the β^{-} end point energy comes out to be around 800 keV. The maximum

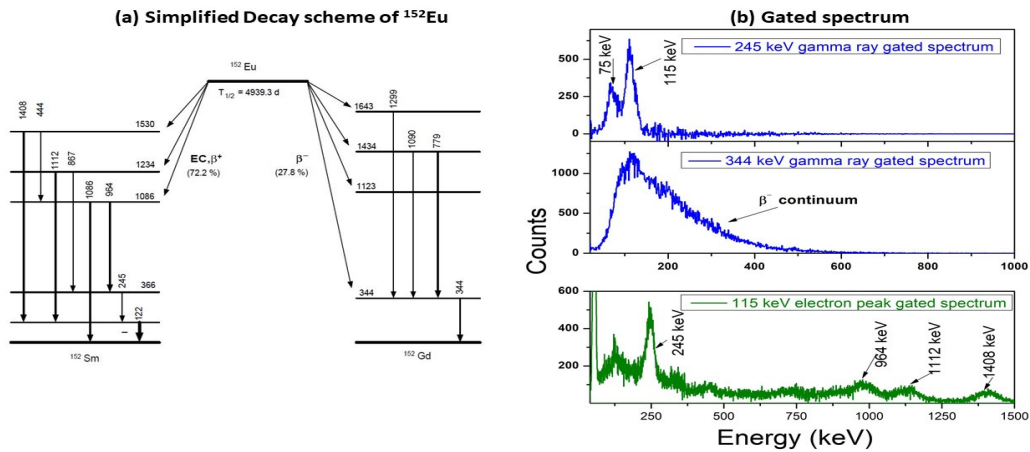


Figure 4.20: (a) A simplified decay scheme of ^{152}Eu is shown in the figure [76]. Approximate energies are presented in keV. (b) The gated spectra is represented. The spectra in blue colour are the projected electron spectra gating the specified gamma transition indicated in box. The spectrum in green colour is the projected gamma spectrum gating 115 keV electron peak.

β^- - decay energy corresponding to 344 keV is noted at 1.474 MeV with 0.574 MeV being the average value [77]. Likewise, the gamma spectrum with gate on the electron peak at 115 keV is also projected. The gamma peak at 244 keV, 964 keV, 1112 keV and 1408 keV are identified in the projected spectrum. All of these are in coincidence with 122 keV.

Thus this setup is successful to detect electrons as well as gamma rays and establish their coincidental relationship.

CHAPTER 5

Theoretical study for Sn isotopes

5.1 Introduction

The long isotopic chain between ^{100}Sn to ^{138}Sn beyond ^{132}Sn offers a rich arena with the available spectroscopic information to test the applicability of different theoretical nuclear models. With the advent of the radioactive ion beam (RIB) and improved experimental tools and techniques, the region far away from the stability line is now accessible. However, there are many nuclei with limited or no experimental information available yet. In such cases, a reliable prediction of the theoretical model is more important. Theoreticians have studied and interpreted the existing experimental data of a few proton (neutron)-rich nuclei and predicted other similar nuclei's structure to provide useful information for more experimental efforts. Additionally, these studies are relevant to understand the evolution of nuclear interaction at extremes of isospin with the increasing neutron (or proton) number.

The isotopic chain of Sn has special significance as it encompasses two doubly magic nuclei ^{100}Sn and ^{132}Sn . The nuclei near doubly closed shells have a

relatively simple structure and provide an opportunity to investigate different components of the nuclear interaction.

5.2 Motivation

There are several exciting physics issues associated with different regions of the isotopic chain of Sn. For neutron number $N < 82$, $sn100pn$ [47] interaction has been reasonably successful in the interpretation of data for heavier isotopes of Sn, Te, I.

The near degeneracy of the energies of $1g_{7/2}$ and $2d_{5/2}$ is an issue of concern for light Sn isotopes. Their relative order is a subject of debate. A monopole optimized effective interaction named as Bonnnew proposed in Ref. [78] could explain the swap of the spin. This interaction has also been applied for lighter Te, and I isotopes with neutron numbers just above $N=50$. However, this interaction generated to tackle the issues in lighter Sn isotopes has not been utilized to explain these heavier isotopes.

The Sn isotopic chain is also interesting as many isomers are present in different Sn isotopes and their neighboring elements. Reproduction of the transition rates is always a crucial test for any theoretical model. The transition probability is a reliable measure to test the two (initial and final) overlapped wave-functions, providing useful information about the interaction.

The nuclei in these regions (^{100}Sn to ^{132}Sn) have been studied by several researchers [47,78]. Our primary objective is to test the applicability of these two

interactions over the region from $N=50$ to $N=82$. We have performed Large Scale Shell model (LSSM) calculation using shell model codes "OXBASH" [46], and "NUSHELLX" [79]. We have also utilized a rudimentary way of changing single-particle energies of the Bonnnewpn interaction and named it Bonnsn.

After reviewing the single-particle energies and TBMEs of these three interactions, for calculations of spectra of one and two-valence particle (hole) nuclei close to the double closed ^{100}Sn and ^{132}Sn , the spectroscopic properties of the heavy Sn isotopes are calculated in unrestricted space and compared with experimental data.

5.3 Model space and effective interactions

In this present endeavour, we have worked with three different effective interactions namely: sn100pn [47], Bonnnewpn (a monopole optimised interaction) [78] and a modified version of Bonnnewpn, which is named as Bonnsn interaction [80]. All of these interactions have the common model space consisting of the orbitals: $1g_{7/2}$, $2d_{5/2}$, $2d_{3/2}$, $3s_{1/2}$ and $1h_{11/2}$ both for protons and neutrons with core ^{100}Sn .

5.3.1 The effective interactions used

5.3.1.1 The sn100pn interaction

The sn100pn Hamiltonian [47] is obtained from G matrix derived from CD-Bonn nucleon-nucleon interaction. The charge dependence (CD) of the inter-

action arises from nucleon and pion mass splitting [81]. The $sn100pn$ interaction is a combination of four parts : $sn100nn$ (neutron (ν) – ν interaction), $sn100pp$ (proton(π) – π interaction), $sn100pn$ (ν – π interaction) and $sn100co$ (Coulomb interaction between protons). All the ν – ν two body matrix elements (TBME) are reduced by a factor of 0.9 to reproduce the experimental spectra of ^{130}Sn .

The neutron single particle energies (spe) ([47]) are chosen to reproduce experimental levels of ^{131}Sn . The spes are -10.6089, -10.2893, -8.7167, -8.6944, -8.8152 (all in MeV) for $\nu 1g_{7/2}$, $\nu 2d_{5/2}$, $\nu 2d_{3/2}$, $\nu 3s_{1/2}$ and $\nu 1h_{11/2}$ orbits, respectively. The proton single particle energies ([47]) tuned to reproduce the experimental excitation spectra of ^{133}Sb , are 0.8072, 1.5623, 3.3160, 3.2238, 3.6051 (all in MeV) for $\pi 1g_{7/2}$, $\pi 2d_{5/2}$, $\pi 2d_{3/2}$, $\pi 3s_{1/2}$ and $\pi 1h_{11/2}$ orbits, respectively.

5.3.1.2 The Bonnnewpn interaction

The Bonnnew interaction is an optimized monopole interaction proposed by Chong Qi and Z. X. Xu [78] for Sn isotopes. The interaction is derived from realistic CD Bonn nucleon-nucleon interaction in isospin formalism. The single-particle energies of a few orbitals and the $T=1$ monopole interactions are determined by fitting to the binding energies of 157 low-lying yrast states in $^{102-132}\text{Sn}$.

Originally, this interaction is in isospin formalism, and neutrons and protons have the same single-particle energies. The isospin formalism is useful when

neutrons and protons occupy the same orbitals like nuclei near ^{100}Sn . This interaction has been successful in analyzing the origin of spin inversion of ^{101}Sn w.r.t. ^{103}Sn . It is used mainly to illustrate the structure of nuclei near ^{100}Sn region. Though it has also been applied for the isotopes near ^{132}Sn [83]. In the case of some Sn isotopes with $A \simeq 111$, it cannot reproduce the experimental ground states correctly [78]. The nuclei near ^{132}Sn (with $Z = 50-56$ and $N=74-82$) have large differences in neutron and proton numbers. Thus proton-neutron formalism of representing an interaction may help to tune proton and neutron single-particle energies independently. In the present work, we have converted the interaction Bonnnew to pn formalism and named it Bonnnewpn. However, we have kept the spes same as provided in the original interaction. The spes both for neutron and protons are 0, 0.172, 5.013, 0.369, 3.247 (all in MeV) for the $1g_{7/2}$, $2d_{5/2}$, $2d_{3/2}$, $3s_{1/2}$ and $1h_{11/2}$ orbits, respectively.

5.3.1.3 Bonnsn interaction

To initiate the tuning of the spes of Bonnnewpn to make it more applicable near ^{132}Sn , the two body matrix elements of Bonnnewpn and spes of protons and neutrons from sn100pn interaction have been coupled to generate a new interaction named Bonnsn [80].

5.3.2 Reviewing the SPEs and TBMEs

To test the choice of single-particle energies and the TBMEs of these three interactions, excitation spectra of one and two valence particle (hole) nuclei

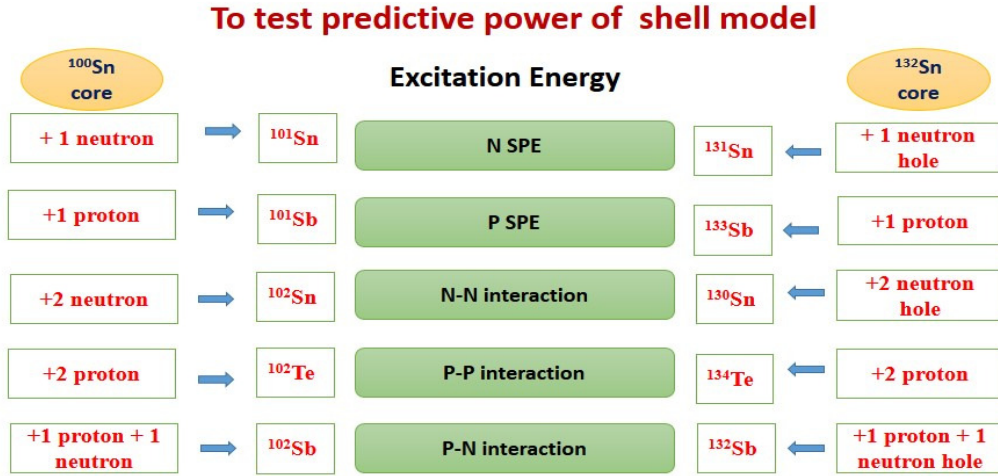


Figure 5.1: The excitation energies of this enlisted nuclei are calculated to understand different ingredients of the effective interaction.

near ^{100}Sn (^{132}Sn) have been calculated and compared with the experimental data (Fig. 5.1).

5.3.2.1 Neutron single-particle energies

To test the choice of the neutron single-particle energies, we have calculated the excitation spectra of ^{101}Sn and ^{131}Sn with the three interactions. We have compared with experimental data [18]. ^{101}Sn can be expressed as ^{100}Sn core with a single neutron particle ($^{100}\text{Sn} + 1\nu$ particle) in the valence shell. On the other hand, ^{131}Sn can be expressed as ^{100}Sn core with 31 neutron particles, or a single neutron hole in $^{132}\text{Sn} + 1\nu$ hole).

In the case of ^{101}Sn , experimental information [7] is available only for the two states, ground state ($7/2^+$), and first excited state ($5/2^+$). Each of the interaction reproduces the ground state. For $5/2^+$ state, results with sn100pn and Bonnsn

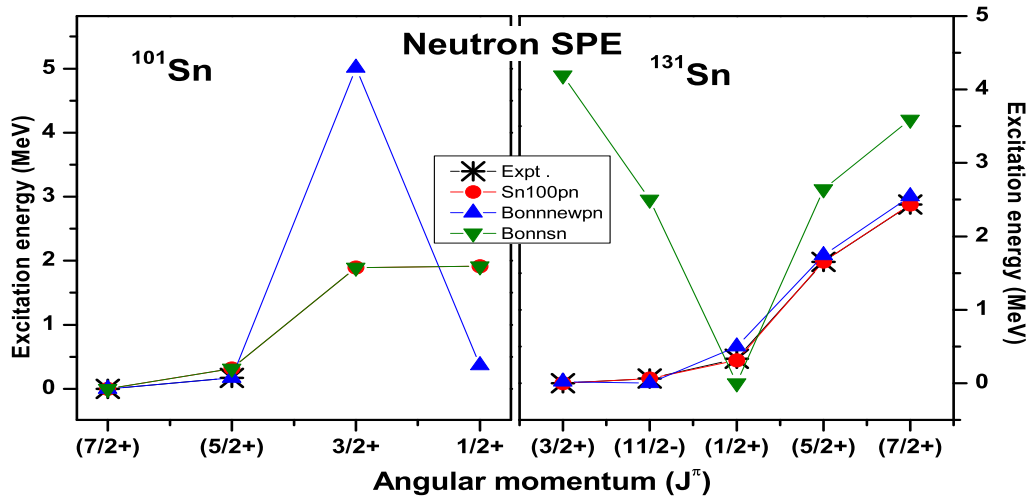


Figure 5.2: The theoretically calculated excitation energies of ^{101}Sn (left panel) and ^{131}Sn (right panel) are shown using different interactions. The experimental data [18] are also plotted wherever available.

show higher values (Fig. 5.2) compared to experimental data.

For ^{131}Sn , the excitation energies calculated using sn100pn and Bonnnewpn match quite well with the experimental values [18]. The results with Bonnsn show deviation, which is expected as the tuning between SPE and TBME is critical (Fig. 5.2).

5.3.2.2 Proton single-particle energies

Similarly, the proton single-particle energies' choice has been tested by calculating the spectra of ^{101}Sb and ^{133}Sb . ^{101}Sb is equivalent to $^{100}\text{Sn} + 1\pi$ particle. ^{133}Sb is expressed as ^{100}Sn core with 32 ν particles and 1 π particle, or ^{132}Sn core with a 1 π particle in valence space.

No experimental data is available for ^{101}Sb . The results using sn100pn are in good agreement with the experimentally observed low-lying states of ^{133}Sb (Fig. 5.3). For 3/2⁺ and 11/2⁻ states, Bonnnewpn interaction overpredicts the

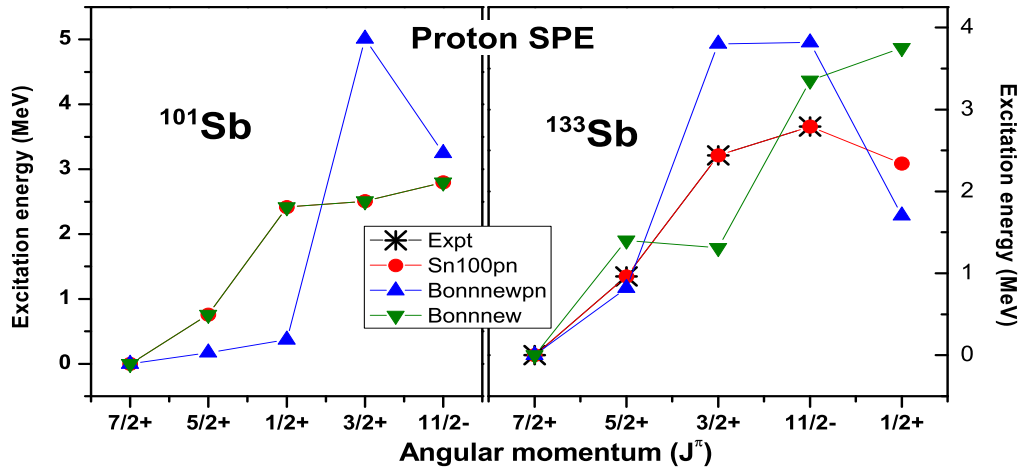


Figure 5.3: The theoretically calculated excitation energies of ^{101}Sb (left panel) and ^{133}Sb (right panel) are shown using different interactions. The experimental data [18] are also compared wherever present.

excitation energies.

5.3.2.3 Neutron-neutron two body matrix elements (TBME)

To test the $\nu - \nu$ TBMEs, the excitation spectra of ^{102}Sn and ^{130}Sn have been calculated. ^{102}Sn can be represented as ^{100}Sn core with two neutron (2ν) particles in the valence orbits. ^{130}Sn has 30 neutrons with ^{100}Sn core or has two neutrons (2ν) holes with ^{132}Sn core.

For ^{102}Sn (Fig. 5.4), the experimental trend is reproduced by all the interactions. Though, Bonnnewpn results overpredict the excitation energies. Moreover, results with all the interactions predict higher energy for 4^+ state than 6^+ state.

For ^{130}Sn , results with sn100pn and Bonnnewpn interactions agree with experimental data reasonably well. But, Bonnnewpn results show gross mismatch (Fig. 5.4).

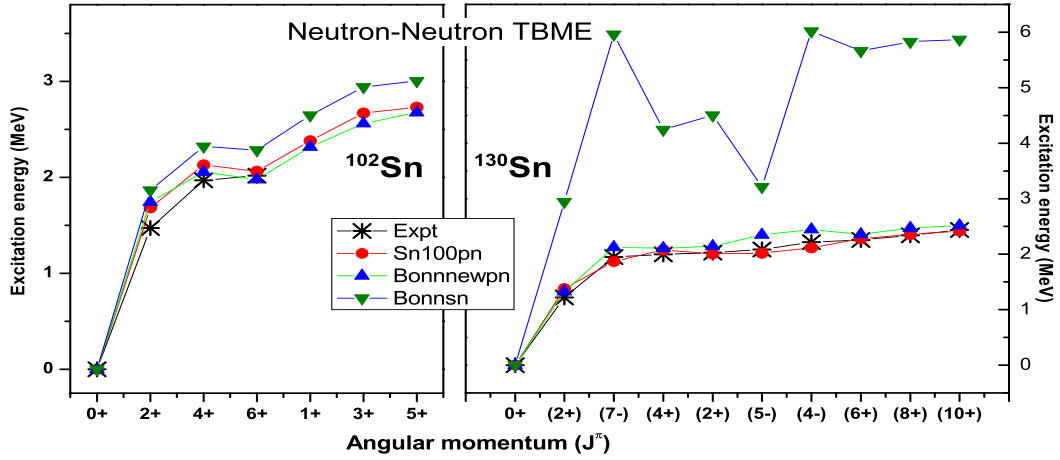


Figure 5.4: The theoretically calculated excitation energies of ¹⁰²Sn (left panel) and ¹³⁰Sn (right panel) are shown using different interactions. The experimental data [18] are also plotted wherever available.

5.3.2.4 Proton-proton two body matrix elements (TBME)

The proton-proton TBMEs have been tested by calculating the energy spectra of ¹⁰²Te and ¹³⁴Te. In the case of ¹⁰²Te, there is no valence neutron outside ¹⁰⁰Sn core, and only two proton (2π) particles occupy the proton shells. On the opposite side, ¹³⁴Te can be expressed as filled neutron orbitals with ¹⁰⁰Sn core, with two proton (2π) particles in the proton valence shells.

For ¹⁰²Te, no experimental information is available. The same trend is predicted by all three interactions (Fig. 5.5). In the case of ¹³⁴Te, the best agreement with experimental data is obtained for sn100pn interaction. However, it predicts a higher value for 8⁺ state similar to the other interactions. The other interactions could predict the trend of variation of energy with increasing angular momentum (Fig. 5.5).

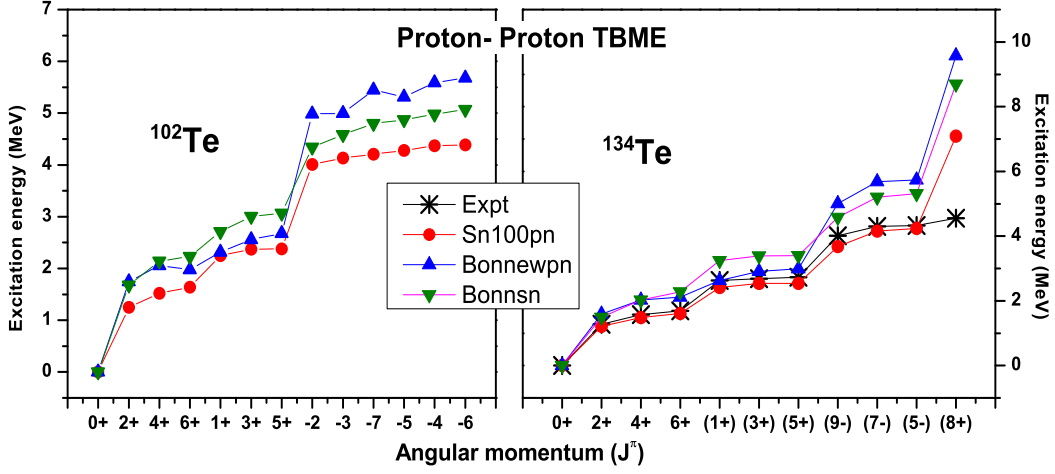


Figure 5.5: The theoretically calculated excitation energies of ^{102}Te (left panel) and ^{134}Te (right panel) are shown using different interactions. The experimental data [18] are also plotted wherever available.

5.3.3 Neutron-proton two body matrix elements (TBME)

To test the $(\nu - \pi)$ TBMEs, the results for ^{102}Sb ($^{100}\text{Sn} + 1\nu + 1\pi$) and ^{132}Sb ($^{100}\text{Sn} + 31\nu$ particle + 1π or $^{132}\text{Sn} + 1\nu$ hole + 1π hole) have been shown in Fig. 5.6. No experimental information is available for ^{102}Sb . We have compared the theoretically predicted values in the figure. The results with sn100pn is totally different from those predicted by other two interactions. For ^{132}Sb , large deviations from data are observed for Bonnsn results, as expected. It is also interesting that although Bonnnewpn fails for ^{133}Sb (Fig. 5.3), good agreement for ^{132}Sb with both Bonnnewpn and sn100pn is noted. This indicates that in Bonnnewpn, $(\pi - \nu)$ TBMEs are better tuned to work near $N=82$.

The results mentioned above indicate that, despite their limitations, both sn100pn and Bonnnewpn can be utilized to study the Sn isotopes over the entire range of masses. However, Bonnsn interaction needs more tuning to be

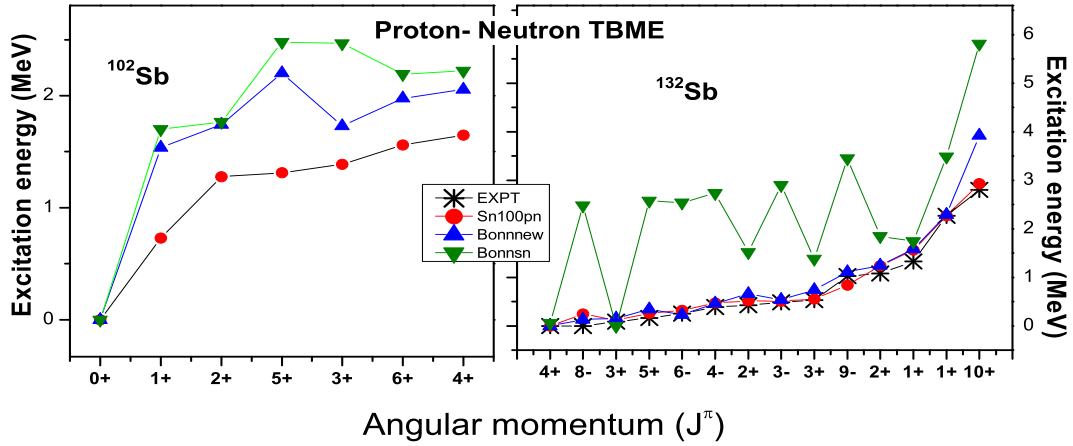


Figure 5.6: The theoretically calculated excitation energies of ^{102}Sb (left panel) and ^{132}Sb (right panel) are shown using different interactions. The experimental data [18] are also plotted wherever available.

used for further calculations. For heavier Sn isotopes, sn100pn interaction is expected to provide better results.

5.4 Isomers in even and odd Sn isotopes

In this current section, we have studied the structure of the isomers observed in even and odd Sn isotopes from mid-shell to the neutron-rich region as presented in Fig. 5.7. The excitation energies and lifetimes of different yrast states mentioned in the figure are extracted from Ref. [18,21,84–86]. Only the lifetimes of 5^- and 7^- states of ^{118}Sn have been quoted from the present work.

The main objective is to investigate their structural changes with the increasing neutron number by analyzing their wave-functions calculated using the shell model approach. The theoretical calculations have been performed with sn100pn and Bonnnewpn interactions. Full-scale calculations can be done with the available computational facility only for $^{124-131}\text{Sn}$. For lighter isotopes, unrestricted calculations become computationally difficult, if not impossible.

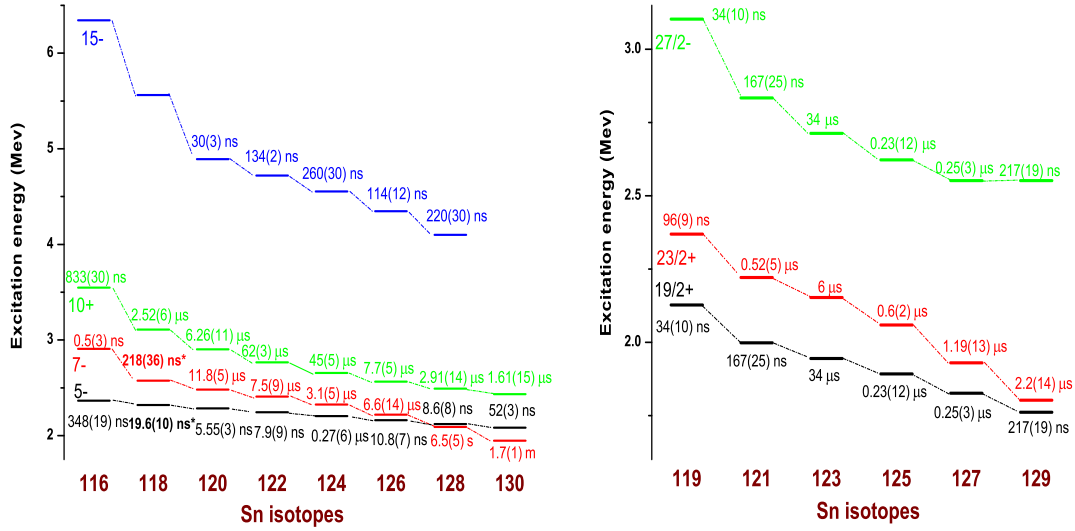


Figure 5.7: The variation of excitation energy and half-lives of different isomers observed in even (left panel) and odd (right panel) isotopes of Sn are shown. Data are taken from Refs. [18, 21, 84–86]. The half-lives of 5^- and 7^- states of ^{118}Sn have been determined in the present work.

Hence, we shall discuss only the structure of $^{124-131}\text{Sn}$ isotopes. A comparison of theoretical results obtained using two interactions with experimental data has been discussed below. At first, the excitation energies are calculated using the two interactions and compared with available experimental data. Then, the transition rates, as well as the composition of wave-functions, are studied.

5.4.1 Calculations and Results

The excitation spectra of even isotopes of Sn, $^{124-130}\text{Sn}$, have been calculated with sn100pn and Bonnnewpn interactions as shown in Fig. 5.8.

From the excitation spectra of $^{124,126,128,130}\text{Sn}$, an overall good agreement with experimental data is observed for both interactions. The results with sn100pn interaction agree with the experimental data relatively better than that with

Bonnnewpn interaction. In general, for positive parity states, the theoretically estimated values are under-predicted with sn100pn interaction. Bonnnewpn interaction causes over-prediction. These deviations are observed in all of these isotopes. In most of the cases, the deviations are within 300 keV.

Even for odd isotopes, $^{125,127,129}\text{Sn}$, the excitation energies are calculated theoretically and compared with experimental data shown in Fig. 5.9. For these three isotopes, the deviation is larger for Bonnnewpn interaction, similar to even isotopes. Bonnnewpn interaction is unable to reproduce the experimentally observed ground state of ^{127}Sn ($11/2^-$). In this interaction, $11/2^-$ state lies at 27 keV. Apart from that, both interactions show overall good agreement with experimental data.

A regularity is seen in the variation of excitation energies of isomeric states in different isotopes of Sn (Fig. 5.7). In heavier even Sn isotopes, yrast 5^- and 7^- states are low spin isomers. It is evident that the level energies of 7^- and 5^- states decrease with increasing neutron numbers, and an inversion of the relative positions of these two states is observed at ^{128}Sn . According to Iskra *et al.* [85], it is an indication that the position of Fermi level with respect to the $3s_{1/2}$ and $2d_{3/2}$ is changed. This configurational change is also reflected through the half-lives of the isomeric states. From $A=120-126$ Sn, the half-lives of 7^- states are of the order of μs . However, in ^{128}Sn , the 7^- state $T_{1/2}=6.5$ (5)s [18], which is about 10^6 orders higher than its nearest neighbour. From $A=114-126$, the isotope excited in the 7^- state primarily decays to the final

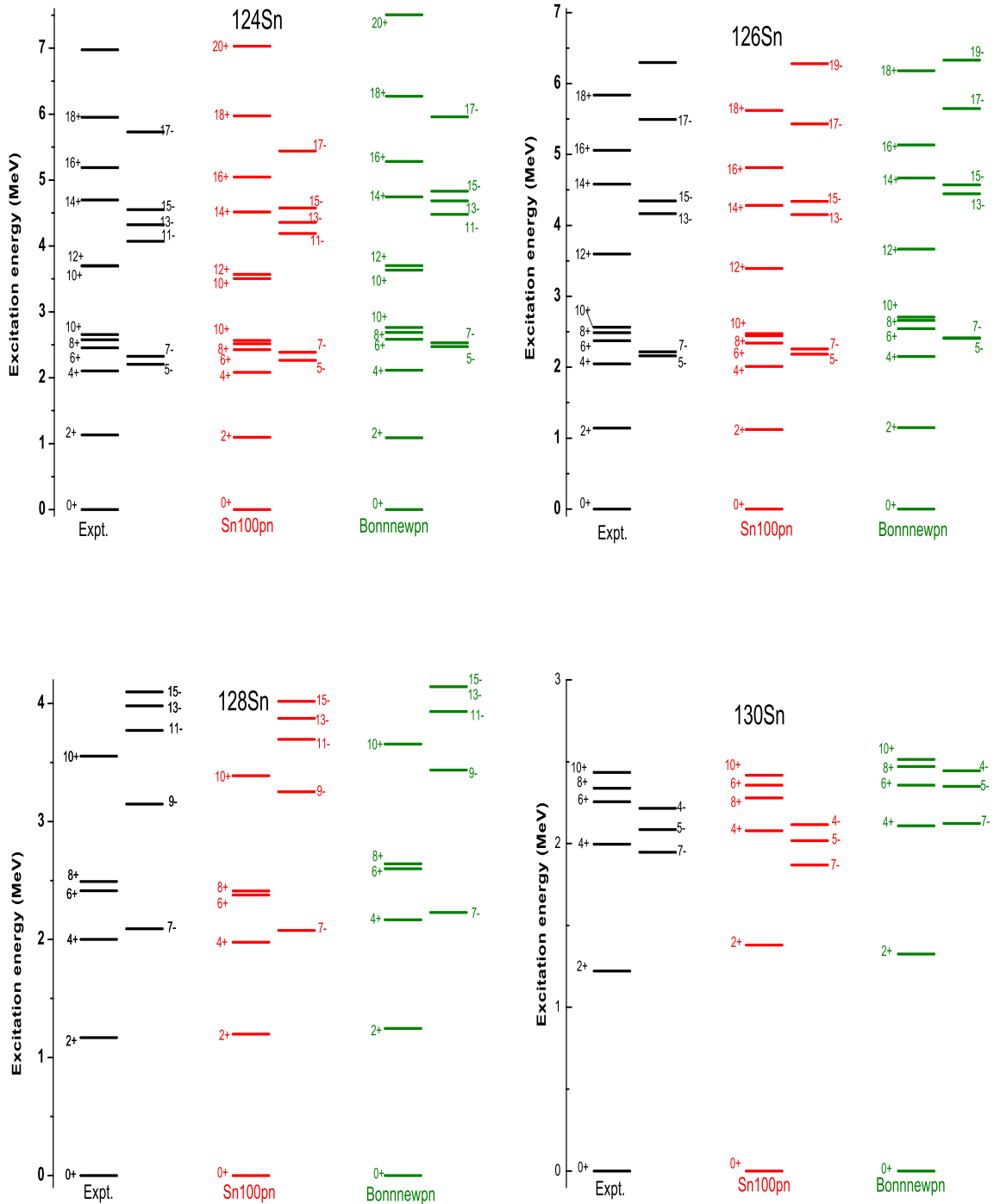


Figure 5.8: Comparison of experimental and calculated (two interactions : sn100pn and Bonnnewpn) excitation spectra of $^{124,126,128,130}\text{Sn}$. Experimental data are obtained from Ref. [18].

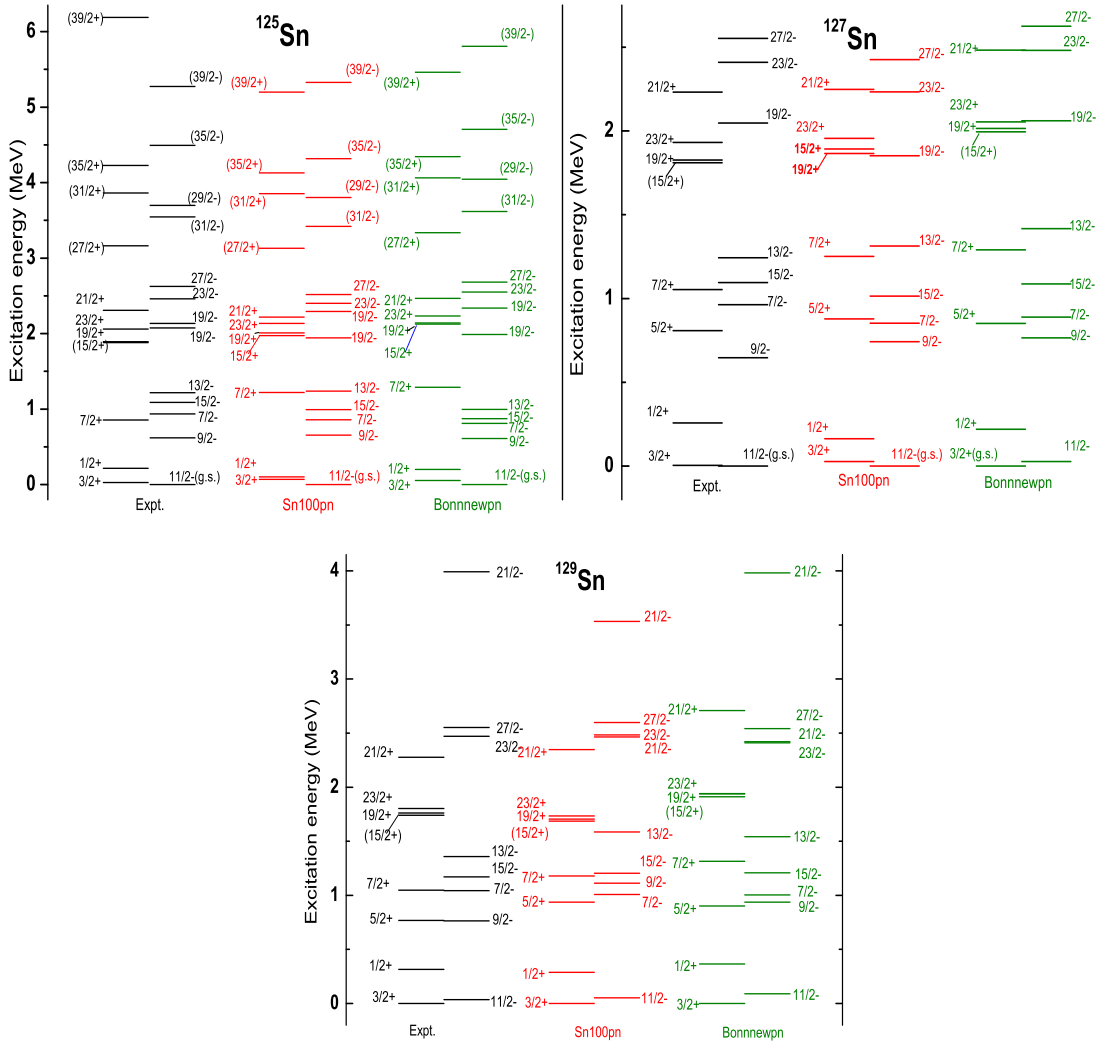


Figure 5.9: Comparison of experimental and calculated (two interactions : sn100pn and Bonnnewpn) excitation spectra of $^{125,127,129}\text{Sn}$. Experimental data extracted from Ref. [18].

state 5^- state via an E2 transition. But, because of change in these two states' positions in ^{128}Sn , the 7^- state has to decay to 4^+ state. This decay is through a higher multipolarity transition ($\Delta J=3$, E3 transition), resulting in a longer half-life of the 7^- state. Similarly, 7^- state of ^{130}Sn has to decay to 2^+ state (or to the 0^+ ground state) through an E5 transition (or higher-order multipole transition) leading to minute order half-life.

Similarly, in the case of odd isotopes, a lot of isomers are observed. Among

them, $19/2^+$ state and $23/2^+$ state are well known. In the formation of these isomers, the role played by intruder $h_{11/2}$ orbital is very important. In the odd mass $A=119-129$ [84, 86] of Sn isotopes, $23/2^+$ and $19/2^+$ isomeric states have been observed. Generally, $23/2^+$ decays to $19/2^+$ state through E2 transition.

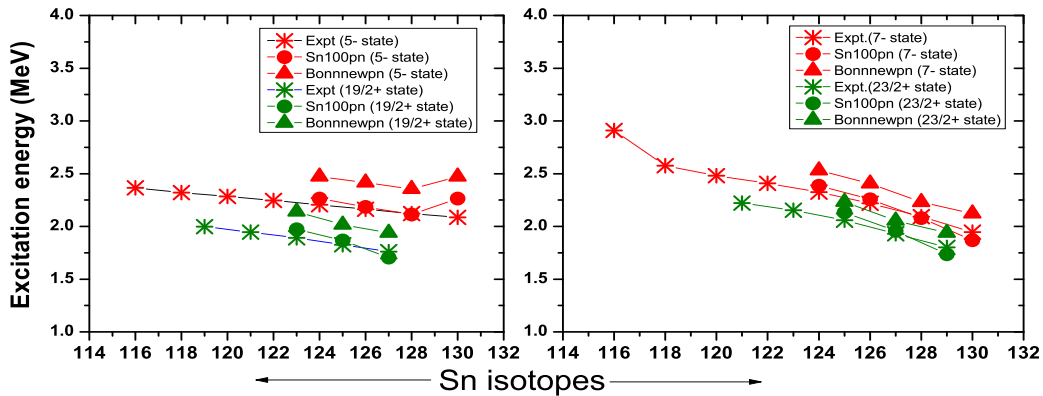


Figure 5.10: The level energies of different isomeric states are shown. The experimental levels (star symbol) are compared with theoretical energies using sn100pn (circle symbol) and Bonnnewpn interaction (up triangle). The left panel shows the excitation energies of 5^- isomeric states of even isotopes and $19/2^+$ states for odd isotopes. The right panel indicates the excitation energies of 7^- isomeric states of even isotopes and $23/2^+$ states for odd isotopes.

In this portion, we have systematically shown (full space theoretical calculation is done only for $A=124-130$ Sn) the excitation energy evolution of yrast 5^- , 7^- states of even Sn isotopes as well as $23/2^+$ and $19/2^+$ states of odd isotopes with increasing neutron number (Fig. 5.10). For both 5^- and 7^- states, an excellent agreement is observed for $A=124-128$ Sn using sn100pn interaction. However, a higher value is predicted at ^{130}Sn . For Bonnnewpn interaction, an over-prediction is observed for both even and odd isotopes.

The regularity in the excitation energies indicates that these states originate from similar configurations, which is also endorsed by the theoretical results. The 7^- state has major contribution from the configuration $\nu h_{11/2}^1 d_{3/2}^1$. The the-

Table 5.1: Two major partitions in terms of their contributions in the wave-functions of isomeric states are shown for both interactions, sn100pn and Bonnnewpn. The partitions are presented in terms of the occupation numbers of neutrons in the following order : $1g_{7/2}$, $2d_{5/2}$, $2d_{3/2}$, $3s_{1/2}$ and $1h_{11/2}$. The table contains the information for yrast 5^- , 7^- states of even isotopes and $19/2^+$, $23/2^+$ states of odd isotopes.

A	5^- (even) / $19/2^+$ (for odd)				7^- (even) / $23/2^+$ (for odd)			
	sn100pn		Bonnnewpn		sn100pn		Bonnnewpn	
	Partition	%	Partition	%	Partition	%	Partition	%
124	[8,6,2,1,7]	23.2	[8,6,2,1,7]	22.0	[8,6,1,2,7]	22.1	[8,6,3,2,5]	31.2
	[8,6,1,2,7]	8.6	[8,6,3,2,5]	12.7	[8,6,3,0,7]	12.8	[8,6,3,0,7]	10.9
125	[8,6,2,1,8]	31.2	[8,6,3,2,6]	30.7	[8,6,1,2,8]	25.3	[8,6,3,2,6]	49.2
	[8,6,1,2,8]	13.7	[8,6,2,1,8]	18.2	[8,6,3,0,8]	18.7	[8,6,3,0,8]	11.7
126	[8,6,2,1,9]	27.8	[8,6,2,1,9]	24.9	[8,6,3,2,7]	24.4	[8,6,3,2,7]	45.2
	[8,6,1,2,9]	13.8	[8,6,3,2,7]	20.1	[8,6,1,2,9]	22.9	[8,6,3,0,9]	14.2
127	[8,6,2,1,10]	25.7	[8,6,3,2,8]	54.0	[8,6,3,2,8]	47.3	[8,6,3,2,8]	66.1
	[8,6,3,2,8]	23.4	[8,6,2,1,10]	10.4	[8,6,3,0,10]	17.2	[8,6,3,0,10]	12.1
128	[8,6,3,2,9]	30.1	[8,6,3,2,9]	36.1	[8,6,3,2,9]	59.8	[8,6,3,2,9]	64.0
	[8,6,4,1,9]	18.5	[8,6,4,1,9]	15.8	[8,6,1,2,11]	11.6	[8,6,3,0,11]	14.3
129	[8,6,3,2,10]	79.0	[8,6,3,2,10]	81.2	[8,6,3,2,10]	96.7	[8,6,3,2,10]	95.4
	[8,6,4,1,10]	17.1	[8,6,4,1,10]	13.2	[8,5,4,2,10]	1.7	[8,5,4,2,10]	2.3
130	[8,6,3,2,11]	57.9	[8,6,3,2,11]	64.8	[8,6,3,2,11]	97.7	[8,6,3,2,11]	96.6
	[8,6,4,1,11]	39.5	[8,6,4,1,11]	31.2	[8,5,4,2,11]	1.4	[8,5,4,2,11]	2.0

oretical calculations performed using both the interactions have similar predictions, as shown in table 5.1. However, the 5^- state is originating from two different configurations: major contribution from $\nu h_{11/2}^1 s_{1/2}^1$ for A=124,126 which changes to $\nu h_{11/2}^1 d_{3/2}^1$ for A=128,130.

Similar to the 7^- state of even isotopes, $23/2^+$ state of odd isotope has the configuration of $\nu 1h_{11/2}^2 2d_{3/2}^1$ and the $19/2^+$ state has contributions from $\nu 1h_{11/2}^2 3s_{1/2}^1$ and $\nu h_{11/2}^2 d_{3/2}^1$ configurations. The average occupancy in each of the orbital for yrast 5^- , 7^- states of even isotopes and $19/2^+$, $23/2^+$ states of odd isotopes are also tabulated in table 5.2.

Table 5.2: Average occupation numbers for neutrons in each orbital of the model space for two different interactions are shown. Details are given for yrast 5^- , 7^- states of even isotopes and $19/2^+$, $23/2^+$ states of odd isotopes.

sn100pn interaction												
A	State	$g_{7/2}$	$d_{5/2}$	$d_{3/2}$	$s_{1/2}$	$h_{11/2}$	State	$g_{7/2}$	$d_{5/2}$	$d_{3/2}$	$s_{1/2}$	$h_{11/2}$
124	5^-	7.49	5.45	2.05	1.17	7.82	7^-	7.50	5.48	2.04	1.26	7.69
125	$\frac{19}{2}^+$	7.69	5.61	2.18	1.28	8.22	$\frac{23}{2}^+$	7.68	5.64	2.25	1.35	8.06
126	5^-	7.71	5.62	2.38	1.32	8.95	7^-	7.50	5.65	2.40	1.48	8.75
127	$\frac{19}{2}^+$	7.85	5.78	2.61	1.48	9.26	$\frac{23}{2}^+$	7.85	5.81	2.69	1.61	9.01
128	5^-	7.86	5.79	2.84	1.50	9.98	7^-	7.86	5.82	2.78	1.75	9.76
129	$\frac{19}{2}^+$	7.98	5.79	3.20	1.82	10.00	$\frac{23}{2}^+$	7.98	5.98	3.03	2.00	10.00
130	5^-	7.99	5.98	3.42	1.60	11.00	7^-	7.99	5.98	3.02	2.00	11.00

Bonnnewpn interaction												
A	State	$g_{7/2}$	$d_{5/2}$	$d_{3/2}$	$s_{1/2}$	$h_{11/2}$	State	$g_{7/2}$	$d_{5/2}$	$d_{3/2}$	$s_{1/2}$	$h_{11/2}$
124	5^-	7.58	5.54	2.32	1.24	7.29	7^-	7.58	5.59	2.49	1.44	6.88
125	$\frac{19}{2}^+$	7.72	5.69	2.62	1.47	7.47	$\frac{23}{2}^+$	7.73	5.73	2.76	1.62	7.14
126	5^-	7.74	5.66	2.57	1.34	8.67	7^-	7.74	5.69	2.75	1.55	8.25
127	$\frac{19}{2}^+$	7.86	5.82	2.93	1.68	8.69	$\frac{23}{2}^+$	7.86	5.83	2.95	1.73	8.60
128	5^-	7.87	5.80	2.92	1.49	9.89	7^-	7.87	5.82	2.94	1.69	9.66
129	$\frac{19}{2}^+$	7.97	5.97	3.18	1.86	10.00	$\frac{23}{2}^+$	7.97	5.97	3.04	2.00	10.00
130	5^-	7.98	5.97	3.35	1.68	11.00	7^-	7.98	5.97	3.03	2.00	11.00

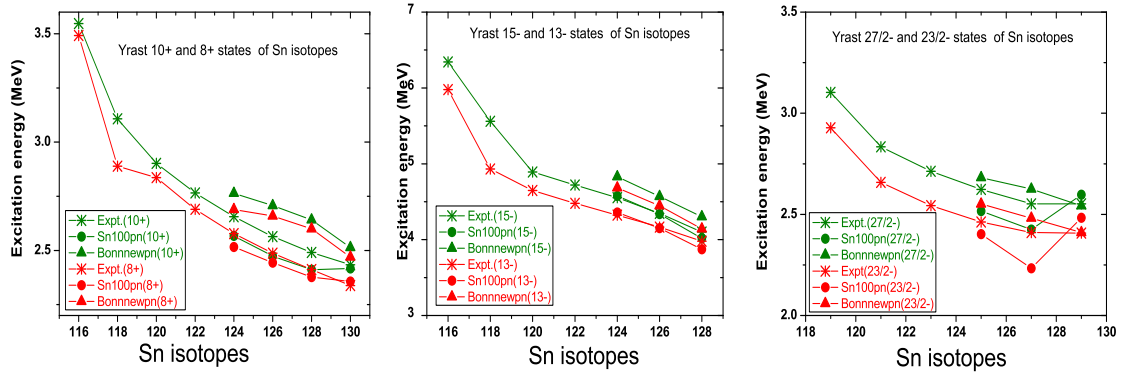


Figure 5.11: The level energies of different isomeric states are shown systematically. The experimental levels (star symbol) are compared with theoretical energies using sn100pn interaction (circle symbol) and Bonnnewpn interaction (up triangle).

It is also noted that, the maximum angular momentum generated by $\nu h_{11/2}^n d_{3/2}^1$ are 7^- and $23/2^+$ for $n=1,2$ respectively. For the values $n=3$, J_{max}^π would be 15^- . In $A=120-128$ Sn [85, 87], 15^- isomeric states are also observed. Usually, this

Table 5.3: Same as table 5.1, except the details are given for yrast 8^+ , 10^+ states of even isotopes and $23/2^-$, $27/2^-$ states of odd isotopes.

A	8_1^+ (even A) / $23/2_1^-$ (for odd A)		10_1^+ (even A) / $27/2_1^-$ (for odd A)		sn100pn		Bonnnewpn	
	Partition	%	Partition	%	Partition	%	Partition	%
124	[8,6,2,2,6]	18.7	[8,6,2,2,6]	26.5	[8,6,2,2,6]	18.5	[8,6,2,2,6]	26.0
	[8,6,2,0,8]	16.3	[8,6,4,2,4]	15.6	[8,6,2,0,8]	16.1	[8,6,4,2,4]	15.9
125	[8,6,2,2,7]	31.8	[8,6,4,2,5]	31.48	[8,6,2,2,7]	34.5	[8,6,4,2,5]	31.6
	[8,6,2,0,9]	13.9	[8,6,2,2,7]	29.0	[8,6,2,0,9]	12.8	[8,6,2,2,7]	29.6
126	[8,6,2,2,8]	37.8	[8,6,4,2,6]	31.1	[8,6,2,2,8]	37.2	[8,6,4,2,6]	29.1
	[8,6,4,0,8]	9.09	[8,6,2,2,8]	28.2	[8,6,4,0,8]	9.07	[8,6,2,2,8]	28.2
127	[8,6,2,2,9]	52.5	[8,6,4,2,7]	53.7	[8,6,2,2,9]	54.4	[8,6,4,2,7]	61.4
	[8,6,4,0,9]	10.4	[8,6,2,2,9]	24.6	[8,6,4,2,7]	12.3	[8,6,2,2,9]	21.0
128	[8,6,2,2,10]	43.8	[8,6,4,2,8]	60.1	[8,6,2,2,10]	45.2	[8,6,4,2,8]	59.0
	[8,6,4,0,10]	11.5	[8,6,2,2,10]	20.3	[8,6,4,0,10]	11.7	[8,6,2,2,10]	21.4
129	[8,6,4,2,9]	99.4	[[8,6,4,2,9]	99.5	[8,6,4,2,9]	100	[8,6,4,2,9]	100
130	[8,6,4,2,10]	100	[8,6,4,2,10]	100	[8,6,4,2,10]	100	[8,6,4,2,10]	100

state decays to the 13^- state via E2 transition. We have calculated the excitation energies of these states and compared with the available experimental data [85] as shown in Fig. 5.11 (middle panel). The results obtained using sn100pn interaction depict a fair agreement. Bonnnewpn interaction results can follow the trend of the excitation energies for both of these states.

We also have analyzed the structure of 10_1^+ and $27/2^-$ states. These isomeric states have the typical configuration $\nu h_{11/2}^n$, where $n=2$ for even isotopes and $n=3$ for odd isotopes (n is the number of broken pair). These isomeric states are observed over the entire mass region of $A=116-130$. It is observed that for $27/2^-$ (table 5.3) the probability of having $h_{11/2}^3$ configuration is 100% (for both interactions) for ^{129}Sn and the purity of this state reduces with the decreasing neutron number (odd isotopes). The $23/2^-$ state is also a member of the above-mentioned multiplet. For ^{129}Sn , $23/2^-$ state has >99% contribution from $h_{11/2}^3$

configuration for both the interaction.

Table 5.4: The reduced transition probabilities $B(E2)$ of different isomeric states observed in even ($A=124-130$) isotopes of Sn. The experimental data extracted from Ref. [18, 85, 88, 89]

A	State $J_i \rightarrow J_f$	Expt.	$B(E2)$ in $e^2\text{fm}^4$							
			sn100pn (e_n^{eff})				Bonnnewpn (e_n^{eff})			
			0.50	0.64	0.70	0.85	0.50	0.64	0.70	0.85
124	$7^- \rightarrow 5^-$	4.01(67)	4.91	8.05	9.63	14.2	0.504	0.826	0.988	1.46
126		11(2)	0.006	0.010	0.012	0.018	3.75	6.14	7.34	10.83
128		-	7.58	12.42	14.85	21.90	9.09	14.89	17.82	26.27
130		41(5)	17.97	29.43	35.21	51.92	17.38	28.48	34.07	50.24
124	$10^+ \rightarrow 8^+$	0.89(11)	3.41	5.59	6.69	9.87	0.014	0.023	0.028	0.041
126		5.6(4)	10.43	17.09	20.45	30.15	3.92	6.43	7.69	11.34
128		14.4(13)	15.88	26.02	31.12	45.89	5.463	8.951	10.71	15.79
130		14.5(14)	5.30	8.69	10.40	15.34	5.30	8.69	10.40	15.34
124	$15^- \rightarrow 13^-$	3.2(4)	36.88	60.42	72.28	147.5	0.665	1.09	1.31	1.92
126		22(2)	15.38	25.2	30.15	44.46	24.55	40.22	48.11	70.94
128		57(8)	29.74	48.73	58.30	85.96	29.36	48.11	57.55	84.85

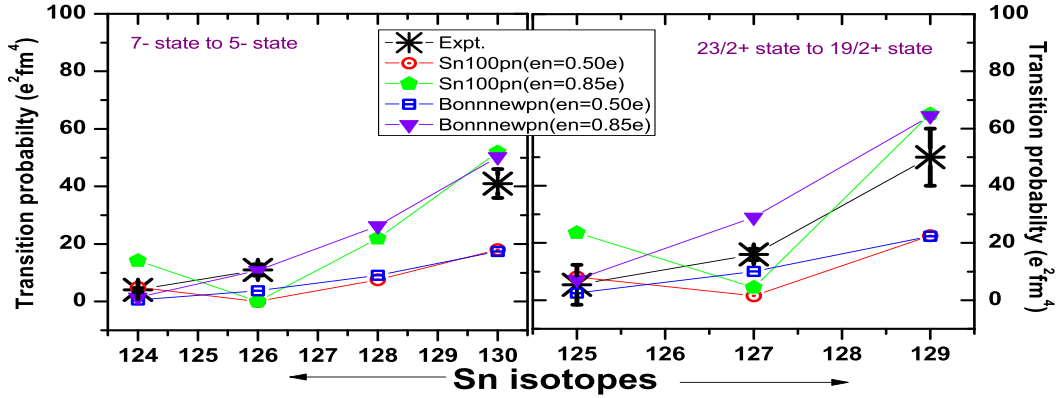


Figure 5.12: The experimental reduced transition probabilities, $B(E2)$ are compared with theoretical results. The calculations are performed for two different effective charges such as $e_n = 0.50e$ and $0.85e$ for both interactions, sn100pn and Bonnnewpn. The results are given for $7^- \rightarrow 5^-$ state for even isotopes (left panel) and $23/2^+ \rightarrow 19/2^+$ state for odd isotopes (right panel).

The reduced transition probabilities related to these isomeric states are also calculated using both the interactions. For theoretical calculation, the transition rates are determined with different neutron effective charges ($e_n^{eff} = 0.50e$,

Table 5.5: The reduced transition probabilities B(E2) of different isomeric states observed in odd (A=125-129) isotopes of Sn. The experimental data extracted from Ref. [84, 86].

A	State $J_i \rightarrow J_f$	Expt.	B(E2) in $e^2\text{fm}^4$							
			sn100pn (e_n^{eff})				Bonnnewpn (e_n^{eff})			
			0.50	0.64	0.70	0.85	0.50	0.64	0.70	0.85
125	$\frac{27^-}{2} \rightarrow \frac{23^-}{2}$	17.7(12)	23.88	39.12	46.80	69.00	7.89	12.94	15.48	22.82
127		26.8(32)	44.27	72.52	86.76	127.9	9.05	14.83	17.74	26.16
129		30.7(122)	11.16	18.29	21.88	32.77	11.18	18.31	21.9	32.3
125	$\frac{23^+}{2} \rightarrow \frac{19^+}{2}$	5.4(7)	8.14	13.34	15.96	23.54	2.51	4.12	4.92	7.26
127		16(2)	1.54	2.53	3.03	4.47	10.02	16.42	19.64	28.97
129		50(10)	22.52	36.9	44.15	65.09	22.29	36.53	43.70	64.43
125	$\frac{19^+}{2} \rightarrow \frac{15^+}{2}$	22(4)	9.70	15.89	19.01	28.03	8.60	14.09	16.86	24.86
127		39(9)	15.51	25.42	30.4	44.83	20.38	33.39	39.95	58.90
129		58(9)	32.61	53.43	63.92	94.24	33.17	54.34	65.01	95.85

0.64e, 0.70e, 0.85e) in order to estimate the effective charge over the mass region.

The transition rate related to $7^- \rightarrow 5^-$ state is estimated for A=124-130 Sn. In the case of $^{128,130}\text{Sn}$, the 7^- state is energetically lower than the 5^- state. For ^{130}Sn , for the sake of completeness, the transition probability of $5^- \rightarrow 7^-$ is converted to $7^- \rightarrow 5^-$ state by including appropriate factor. The B(E2) values for different effective charges are tabulated in table 5.4 and are plotted in Fig.5.12 (left panel).

The transition rate associated with $23/2^+ \rightarrow 19/2^+$ state is plotted in Fig. 5.12 (right panel) and the values are tabulated in table 5.5. Also, the transition rates of $15^- \rightarrow 13^-$ state for even isotopes (left panel) and $19/2^+ \rightarrow 15/2^+$ state for odd isotopes are shown in Fig.5.13. In Fig.5.14, the reduced transition prob-

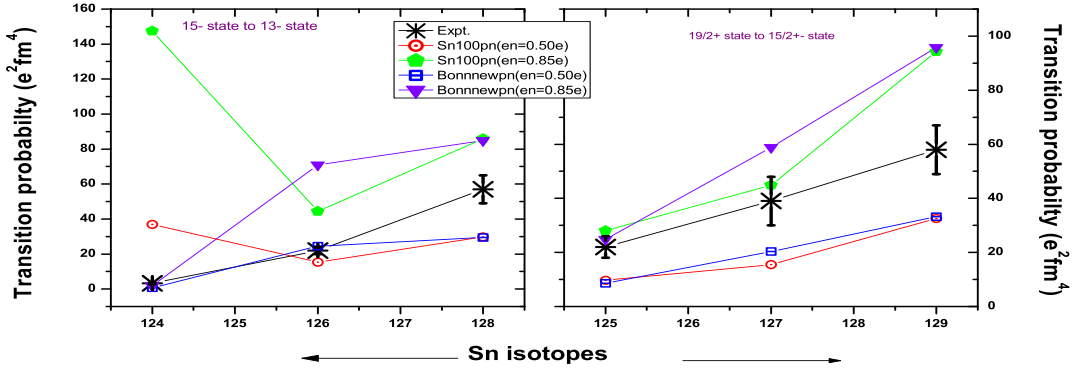


Figure 5.13: The experimental reduced transition probabilities, $B(E2)$ are compared with theoretical results. The calculations are performed for two different effective charges such as $e_n = 0.50e$ and $0.85e$ for both interactions, sn100pn and Bonnnewpn. The results are given for $15^- \rightarrow 13^-$ state for even isotopes (left panel) and $19/2^+ \rightarrow 15/2^+$ state for odd isotopes (right panel).

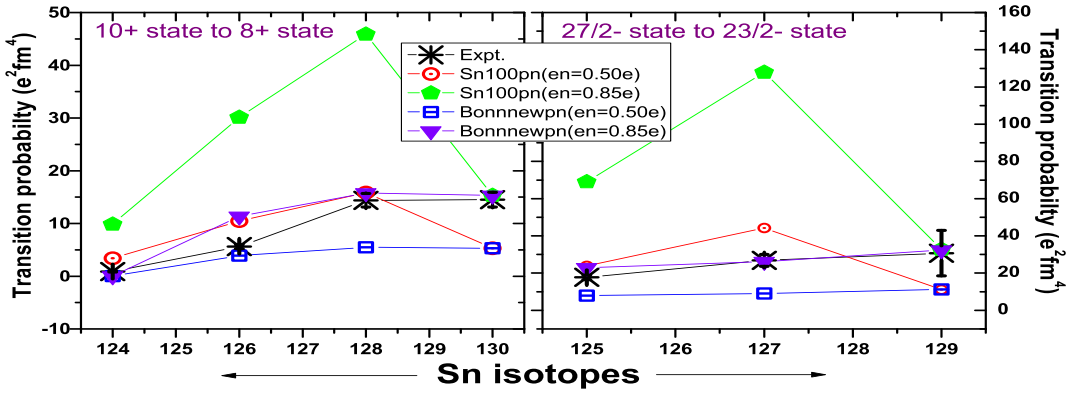


Figure 5.14: Same as Fig.5.12. Here, the results are plotted for $10^+ \rightarrow 8^-$ state for even isotopes (left panel) and $27/2^- \rightarrow 23/2^-$ state for odd isotopes (right panel).

abilities of $10^+ \rightarrow 8^+$ state for even Sn isotopes (left panel) and $27/2^- \rightarrow 23/2^+$ state for odd isotopes are shown. With increasing neutron number, we need to increase the effective charge to reproduce the experimental data. A particular value of effective charge is unable to reproduce the experimental data. For ^{130}Sn , for a fixed effective charge, the estimated rate is same for both the interactions. Because of absence of any mixing, $B(E2)$ values are independent of SPEs and TBMEs of the interaction. Hence we need to exclude this $N=80$ results to fix the effective charge.

The gyromagnetic factors or g factors are also important parameters that provide useful information about the single particle composition of the wavefunctions. We have also calculated the magnetic moments of 2_1^+ state of even isotopes ($^{124-128}\text{Sn}$) along with $3/2_1^+$ and $11/2_1^-$ state of odd isotopes ($^{125-131}\text{Sn}$) [90]. The calculations are performed using free g factor ($g_v^s = -3.826$, $g_v^l = 0$) and also with an effective quenching factor, $q_s = 0.7$. The theoretical results are compared with the experimental data [91]. The figure (Fig.5.15) shows that a better agreement is achieved with the introduction of quenching factor.

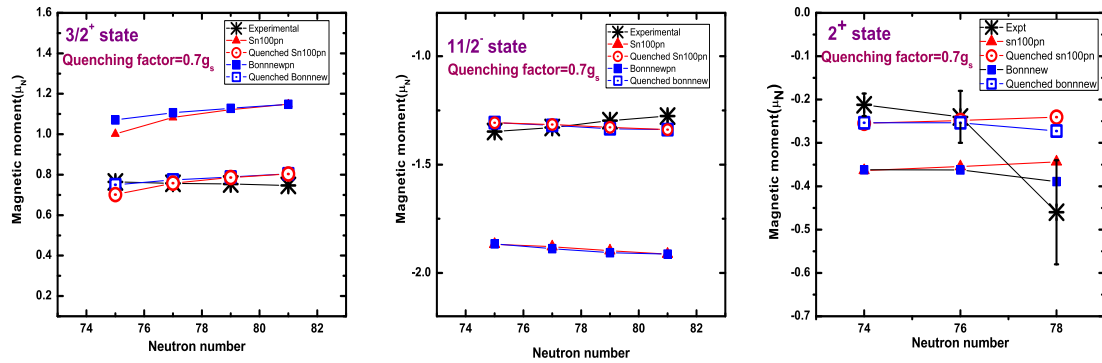


Figure 5.15: The theoretically calculated magnetic moments are compared with the experimental results [91].

CHAPTER 6

Cross-shell excitation near ^{132}Sn

6.1 Introduction

The region near ^{132}Sn holds a significant importance in nuclear structure physics and nuclear astrophysics because of the presence of two shell-closures at $Z=50$ and $N=82$. The structural information of these nuclei are helpful to examine different basic ingredients of different theoretical models.

Typically, the excitation spectra of these nuclei near to shell closure show two different types of excitation mechanisms : the first one is the excitation of valence particles within the specified shell and the other being the excitation involving across the shell gap [94]. Roughly speaking, the low-lying structure can be described by different effective interactions including the nearest intruder orbital from the higher opposite parity shell. Whereas, to characterise the high energy states featuring cross-shell excitation, the involvement of the other orbitals across the shell are mandatory. However, such interaction encompassing over two major shells are not very readily available for heavier

nuclei except for some recent studies [94]. Furthermore, unrestricted calculation over a such large model space is computationally challenging. Hence, one need to put proper truncation to achieve fairly precise results.

To describe near Sn region mainly two different model spaces are adopted for neutrons. In case of $N < 82$, the standard model space (above Z , $N = 50$ shell gap) contains five orbitals namely, $1g_{7/2}$, $2d_{5/2}$, $2d_{3/2}$, $3s_{1/2}$ and $1h_{11/2}$ both for protons and neutrons with ^{100}Sn core. On the other hand, to depict the excitation of nucleus for $N > 82$, the usual model space constitutes with six neutron orbits, viz, $1h_{9/2}$, $1f_{7/2}$, $3p_{3/2}$, $3p_{1/2}$, $1f_{5/2}$, and $1i_{13/2}$ with the same proton orbitals as in $N < 82$. Hence, the core of the model space is ^{132}Sn .

The effective interactions such as, $\text{sn}100\text{pn}$ and CWG [47] are quite successful to describe the low energy states. However, in most of the cases, they can not reproduce higher energy states involving cross-shell excitations. These interactions are not constructed to describe the excitation spectra of a doubly closed shell nucleus, like, ^{132}Sn . Only the ground state can be calculated by such existing standard interactions. Moreover, for its very close neighbours, only a few low energy states can be estimated theoretically.

It is also interesting to point out that such cross-shell excitation is not merely noticeable near the region of doubly magic nucleus to illustrate high spin states. Even, such kind of excitation is also evident in mid-shell nucleus (such as ^{118}Sn) for describing low spin states [95].

Table 6.1: Details of E1 transition from 5^-_1 state to 4^+_1 state of even $^{118-130}\text{Sn}$ isotopes. Experimental data extracted from NNDC [18].

A	Transition energy $5^-_1 \rightarrow 4^+_1$ (keV)	Half-life of 5^-_1 state
118	40.8 (1)	21.7 ns (2)
120	89.87(16)	5.55 ns (3)
122	103.74 (1)	7.9 ns (9)
124	102.91 (2)	0.27 μs (6)
126	111.79 (5)	10.8 ns (7)
128	120.54 (5)	8.6 ns (8)
130	89.23 (3)	52 ns (3)

6.2 Motivation of this work

In the subsection 2.4.3.1, it is noted from the level scheme of ^{118}Sn that 5^-_1 state is an isomer having half-life around 20 ns. With increasing neutron number up to ^{130}Sn , in each even isotope, this 5^-_1 isomer is observed systematically (Table 6.1). This state decays primarily to 4^+_1 state via E1 transition by emitting a low energy gamma ray. In this present work, our goal is to calculate the transition rates related to E1 transition theoretically in the framework of shell model.

In general, electric dipole (E1) transitions are observed with decay probabilities around 10^{-5} to 10^{-9} Weisskopf unit. These transitions rates are retarded because of the organization of nuclear orbitals. Usually, the nuclear orbitals connecting by the dipole operators are at a larger distance in terms of energy. In order to proceed by E1 transition, the connecting orbital must have $\Delta J = 1$ with changing parity. Due to small but finite overlapping between the initial and final wave-function, a slower rate in E1 transition is observed.

Now, in the standard gdsh model space, this E1 transition rate can not be calculated due to the unavailability of opposite parity orbital with $\Delta J = 1$. To probe this particular problem, there is a demand to extend the model space by including opposite parity orbitals with the conventional model space. In the forthcoming sections, a multi-shell interaction has been constructed from two well known interactions. To check the applicability of the newly formed interaction, the excitation energy as well as transition rates are calculated for ^{132}Sn and its neighbouring nuclei. Furthermore, the transition rates related to E1 transition ($5_1^- \rightarrow 4_1^+$) of $^{118-130}\text{Sn}$ have been calculated.

6.3 Formalism

In this current section, we shall describe the derivation of the newly formed interaction. It is referred as sm56 with appropriate suffixes for two different variant interactions, sm56fp and sm56fph.

6.3.1 Model space and choice of single particle energies (spe)

In this newly formed interaction, we have restricted the model space by taking only two proton orbitals ($\pi 1g_{7/2}$ and $\pi 2d_{5/2}$) to tackle the problem of dimensionality. Whereas, the model space for the neutrons are expanded by adding three orbitals ($\nu 1h_{9/2}$, $\nu 2f_{7/2}$, $\nu 3p_{3/2}$) along with the standard gdsh model space. Therefore, the model space is constituted with two proton orbitals ($\pi 1g_{7/2}$ and $\pi 2d_{5/2}$) only and eight neutron orbitals ($\nu 1g_{7/2}$ and $\nu 2d_{5/2}$, $\nu 2d_{3/2}$, $\nu 3s_{1/2}$,

$\nu 1h_{11/2}$, $\nu 1h_{9/2}$, $\nu 2f_{7/2}$, $\nu 3p_{3/2}$) with ^{100}Sn as core.

The new Hamiltonian has been derived mainly from two very widely known interactions of this region: sn100pn and CWG interactions [47]. For the sake of clarity, the proton orbits are expressed by P and the neutron orbitals below $N = 82$ shell (i.e. $1g_{7/2}$, $2d_{5/2}$, $2d_{3/2}$, $3s_{1/2}$, $1h_{11/2}$) are referred as $N1$ and whereas, above $N = 82$ shell ($1h_{9/2}$, $2f_{7/2}$, $3p_{3/2}$) are noted to as $N2$.

The single particle energies (spe) of the neutron orbitals are considered to be -9.74, -8.97, -7.31, -7.62, -7.38 (all in MeV) for $\nu 1g_{7/2}$, $\nu 2d_{5/2}$, $\nu 2d_{3/2}$, $\nu 3s_{1/2}$, $\nu 1h_{11/2}$, respectively, as proposed in Ref. [47]. These spes are chosen to match the experimental spectra of ^{131}Sn [47]. Whereas, for the orbitals above $N = 82$ shell, the spes are considered by adjusting the spe of $\nu 2f_{7/2}$ orbit such that the experimental binding energy (be) of ^{133}Sn with respect to ^{132}Sn are reproduced. In order to calculate the binding energy, all the orbitals below $N = 82$ shell are filled up and only one particle is allowed in the orbit above $N = 82$ shell. Also, the other orbits must follow $3/2_1^-$ and $9/2_1^-$ states of ^{133}Sn . Hence, the chosen spes are 11.06, 5.718 and 8.287 (all in MeV) for $\nu 1h_{9/2}$, $\nu 2f_{7/2}$, $\nu 3p_{3/2}$ orbits respectively.

The proton spes are considered to be 0.8072 and 1.5623 (all in MeV) respectively for $1g_{7/2}$ and $2d_{5/2}$ orbitals respectively following sn100pn interaction.

6.3.2 The two body matrix elements (tbme)

The two-body matrix elements (tbme) have been extracted following the prescribed way.

- The proton-proton tbmes are $\langle P_i P_j | V | P_k P_l \rangle_{I,1}$ where i, j, k, l are the proton orbits. These elements are obtained from sn100pp (i.e. $\pi - \pi$ part of sn100pn interaction) including the Coulomb contribution from sn100co.
- The neutron-neutron tbmes have been categorised into a few groups as follows
 - The tbmes of the intra-shell interaction (i.e. within a particular shell) for neutron orbits below $N = 82$ shell ($\nu 1g_{7/2}, \nu 2d_{5/2}, \nu 2d_{3/2}, \nu 3s_{1/2}, \nu 1h_{11/2}$), $\langle N1_i N1_j | V | N1_k N1_l \rangle_{I,1}$ coupled to I and $T=1$, are taken from sn100nn interaction.
 - The tbmes involving the neutron orbitals $N > 82$, $\langle N2_i N2_j | V | N2_k N2_l \rangle_{I,1}$ (i.e. interaction between $\nu 1h_{9/2}, \nu 2f_{7/2}, \nu 3p_{3/2}$) coupled to I and $T=1$, have been obtained from CWG interaction.
 - Additionally, the $T = 1, \pi - \nu$ tbmes of CWG interaction have been considered as cross-shell neutron-neutron tbmes, viz., $\langle N1_i N2_j | V | N1_k N2_l \rangle_{I,1}$ by following the isospin invariance and charge independence of nuclear interaction.
 - Also, some of neutron-neutron tbmes like $\langle N1_i N2_j | V | N1_k N1_l \rangle_{I,1}$ or $\langle N1_i N2_j | V | N2_k N2_l \rangle_{I,1}$ which are absent in the $\pi - \nu$ tbme set of

CWG interaction have been estimated from zero range delta interaction [96]. The details of this calculation will be discussed in the section 6.3.2.1.

- The proton-neutron tbmes involving the neutron orbits below $N=82$, *viz.*, $\langle P_i N 1_j | V | P_k N 1_l \rangle_{I,1 \text{ and } 0}$ have been deduced from sn100pn and those for neutron orbits above $N = 82$ shell, *viz.*, $\langle P_i N 2_j | V | P_k N 2_l \rangle_{I,1 \text{ and } 0}$ have been considered from CWG interaction.
- Rest of the $\pi - \nu$ tbmes, *viz.*, $\langle P_i N 1_j | V | P_k N 2_l \rangle_{I,1 \text{ and } 0}$ have also been estimated using delta interaction.

This newly formed interaction contains total 1466 two body matrix elements and among them 21 PP elements, 883 NN elements and 562 PN elements. The number of PP, NN, PN elements for a specific I is also tabulated in table 6.2. Moreover, the details of different number of matrix elements with isospin $T=0$ and 1 are categorised for a given set of I as shown in table 6.3.

Apart from that, to reproduce the experimental results of some nuclei, a fine tuning of the tbmes have been done as discussed below.

6.3.2.1 Calculation using Delta interaction

As mentioned in earlier section, some of the unknown tbmes are calculated using ‘zero range delta interaction’ [96]. This is one of the useful and sim-

Table 6.2: Numbers of Proton-Proton (PP), Neutron-Neutron (NN) and Proton-Neutron (P-N) two body matrix elements for different set of I (both positive and negative parity states).

I	PP	NN	PN	Total
0	3	39	5	47
1	1	36	41	78
2	6	191	99	296
3	1	133	129	263
4	6	211	115	332
5	1	114	77	192
6	3	100	51	154
7	0	31	31	62
8	0	21	12	33
9	0	4	2	6
10	0	3	0	3

Table 6.3: Numbers of two body matrix elements $\langle j_\alpha j_\beta | V | j_\delta j_\gamma \rangle$ for different set of I and T (both positive and negative parity states).

	I=0	I=1	I=2	I=3	I=4	I=5	I=6	I=7	I=8	I=9	I=10	Total
T=0	1	25	43	72	51	43	24	16	6	1	0	282
T=1	46	53	253	191	281	149	130	46	27	5	3	1184

ple schematic interactions that generally emphasises the short range nature of nucleon-nucleon interaction. It has the form of

$$V_{eff}(1, 2) = -V_0(1 - \alpha + \alpha \sigma_1 \cdot \sigma_2) \delta(\vec{r}_1 - \vec{r}_2), \quad (6.1)$$

where, V_0 is the strength of the force. The value of parameter α varies between 0 to 1. The calculation has been done using a Fortran program provided in the pioneering book of Kris Hyde [96].

6.3.2.2 Tuning of cross-shell $\nu - \nu$ tbme

As discussed earlier, a set of cross-shell neutron-neutron ($\nu - \nu$) tbmes of particle-hole multiplets have been deduced from the T=1 tbmes of $\nu - \pi$ in-

interaction from CWG Hamiltonian. But, these times are unable to match the low-lying experimental spectra of ^{132}Sn [98]. In Bocchi *et al.*, [99], these states are identified theoretically using RPA calculations as a member of particle-hole multiplets.

Such kind of discrepancy in this collated interaction is expected. This is because though nuclear interaction is assumed to be charge independent; but Pauli exclusion principle (that warrant anti-symmetrization of two wave-function) differentiates between the interaction originating from similar and dissimilar type of nucleons. It is also noted that, though the interaction energies of T=1 parts of $\pi - \pi$, $\nu - \nu$ and $\nu - \pi$ are alike for a pair of nucleons in the same orbit, the interaction between like nucleons are much weaker than those between unlike ones as mentioned in Ref. [100]. The interaction energies are much different for dissimilar orbits. For two like nucleons, the monopole interaction is mainly repulsive. Whereas, it becomes attractive for unlike nucleons.

Therefore, to overcome this, tuning of the neutron–neutron times is important. The relevant multiplets for ^{132}Sn have been extracted following the procedure described in Ref. [100]. The experimental binding energies of ^{131}Sn , ^{132}Sn and ^{133}Sn extracted from Ref. [101] and the excitation energies of different multiplet states from NNDC [18], are used to obtain the diagonal times of corresponding multiplets.

- *The low-lying positive parity states in ^{132}Sn :*

In formation of the low-lying spectra of ^{132}Sn , the two most important

cross-shell positive parity multiplets are $1h_{11/2}^{-1} - 2f_{7/2}$ and $1h_{11/2}^{-1} - 3p_{3/2}$. Whereas, the coupling arising from $1h_{11/2}^{-1} - 1h_{9/2}$ configuration has significance for generation of 8_2^+ state.

1. *Estimation of the $\nu 1h_{11/2}^{-1} - \nu 2f_{7/2}$ tbmes :*

The diagonal tbmes of $1h_{11/2}^{-1} - 2f_{7/2}$ coupling are estimated from the experimental binding energies of ^{131}Sn , ^{132}Sn and ^{133}Sn [101] as well from the excitation energies of ^{132}Sn [18]. In Ref. [99], the states 2_1^+ , 4_1^+ , 5_1^+ , 6_1^+ , 7_1^+ , 8_1^+ , 9_1^+ are predicted to be members of $1h_{11/2}^{-1} - 2f_{7/2}$ multiplet. Since the minimum angular momentum generated by this configuration is 2, the corresponding experimental energy, $E_x(2^+) = 4.041$ MeV is used as reference energy. As most of the tbmes are negative, the interaction is attractive. In the Fig.6.1, the monopole contribution to the interaction energies is noted. Since, the adopted level scheme of ^{132}Sn does not include a 3^+ state, the corresponding tbme remains unaltered. A comparison of the $\pi - \nu$ interaction energies from CWG interaction [47] with the newly modified energies for $\nu - \nu$ has been shown in Fig. 6.1. Similar kind of observation is also mentioned in Ref. [100], for $1h_{11/2}^{-1} - 2f_{7/2}$ coupling. For this, the monopole interaction between neutrons (-0.1374 MeV) is about two times weaker than those between neutron-proton (-0.2317 MeV).

2. *Tuning of $\nu 1h_{11/2}^{-1} - \nu 3p_{3/2}$ tbmes:*

The coupling $\nu 1h_{11/2}^{-1} - \nu 3p_{3/2}$ can generate angular momenta ranging from 4^+ to 7^+ . The experimental level spectrum of ^{132}Sn contains

only two 6^+ and 7^+ at low spins. Due to lack of experimental data, unlike the tbmes of $\nu 1h_{11/2}^{-1} - \nu 2f_{7/2}$ coupling, all tbmes corresponding to $\nu 1h_{11/2}^{-1} - \nu 3p_{3/2}$ could not be determined in systematic way. However, some of relevant tbmes are tuned in order to improve the predictions for 6_2^+ and 7_2^+ states.

3. Tuning of $\nu 1h_{11/2}^{-1} - \nu 1h_{9/2}$ tbmes:

Similarly, from the coupling of $\nu 1h_{11/2}^{-1} - \nu 1h_{9/2}$ angular momenta ranging from 1^+ to 10^+ can be generated. Few relevant tbmes of this coupling have been tuned to improve the predictions of 7_2^+ and 8_2^+ states.

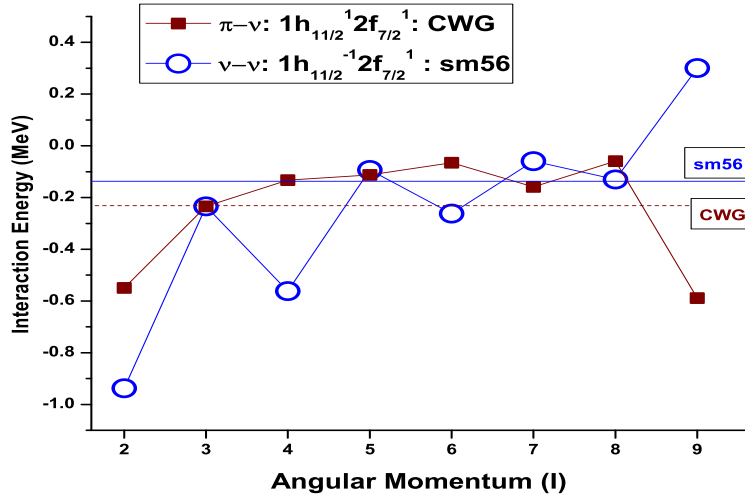


Figure 6.1: The empirical interaction energy between two nucleons is plotted. One of them is in $1h_{11/2}$ orbit and the other in $2f_{7/2}$ orbit. The CWG (sm56: present) tbmes are for $\pi - \nu$ ($\nu - \nu$) interaction. The dashed (solid) line indicates the monopole energy for CWG (sm56: present) interaction.

- *The low-lying negative parity states in ^{132}Sn :*

The negative parity 3_1^- , 4_1^- and 5_1^- states, present in ^{132}Sn , don't have pure multiplet structures. Generally, these angular momenta can be generated from the coupling of $\nu 2d_{3/2}^{-1}$ and $\nu 2f_{7/2}$. Also, the yrast 3^- , 4^- states have

contributions arising from the $\nu 3s_{1/2}^{-1}-\nu 2f_{7/2}$ configuration. The particle in $\nu 1g_{7/2}$ state can be coupled to the holes in $\nu 2d_{5/2}$ and $\nu 1g_{7/2}$ to generate these -ve parity spin states. Hence, these tbmes have not been modified.

6.3.2.3 Tuning of inter-shell tbmes

The present newly modified interaction doesn't include the full proton model space as considered in sn100pp and CWG interactions. Also, the neutron model space for $N > 82$ has been truncated from the one proposed in CWG interaction. Therefore, the corresponding $\pi - \pi$ and $\nu - \nu$ tbmes of this newly formed truncated space are needed the following modifications.

1. *The tuning $\pi - \pi$ tbmes:*

The diagonal two body matrix element for $\pi 1g_{7/2}-\pi 1g_{7/2}$ coupled to $I=0$ is tuned to reproduce the binding energy of ^{134}Te .

2. *The tuning $\nu - \nu$ tbmes:*

The $\nu 2f_{7/2}-\nu 2f_{7/2}$ are tuned to reproduce the binding energy and excitation energies of 2_1^+ to 6_1^+ levels of ^{134}Sn . Additionally, the tbme $\nu 2f_{7/2}-\nu 1h_{9/2}$ corresponding to $I=8^+$ has been adjusted to match experimental 8_1^+ excitation energy.

6.3.2.4 The center of mass correction

It is noted that when a nucleus with A nucleons are studied, out of A coordinates (momenta), only $A-1$ are linearly independent as the wave-functions

can not depend on the center-of-mass (c.m.) coordinates. The nuclear excited states correspond to excitation of the internal degrees of freedom. Hence, the wave-functions should be factorized into relative and c.m. parts. Otherwise, it may give rise to spurious states [102–104] corresponding to c.m. excitation. The c.m. excitation operator has the tensorial rank $J^\pi T=1^-0$. However, the approaches suggested in Refs. [102, 103] in order to resolve the c-m problem become exponentially more difficult with the increasing active nucleons. In case of heavy nuclei, as in the present case, two consecutive complete oscillator shells are not used. Thus, as reported in Hagen *et al.* [104], it is not analytically guaranteed that these wave-functions could be successful in factorization. Therefore, it is evident that in $0\hbar\omega$ and *extruded – intruded (EI)* (as defined in [103]) spaces (like in sn100pn and CWG interactions), in which no $J^\pi T=1^-0$ states existed, the low-energy c.m. spuriousities are absent. In the *extended – extruded – intruded (EEI)* (as defined in [103]) valence spaces, as in the current work, c.m. spuriousness is present due to the presence of orbitals with opposite parity and $\Delta J=1$. Although, Caurier *et al.* [103] demonstrated that for *EEI* space, the spuriousities are strongly suppressed because the main contributor pairs with the largest j 's in each shell, like $(1g_{9/2}, 1h_{11/2})$ and $(1h_{11/2}, 1i_{13/2})$ are always excluded. Hence, in the present work, as well as in earlier studies for heavy nuclei [94, 105] c.m. corrections have been ignored. It is also noted in Ref. [106] that the neglect of the c.m. motion will result into errors of order $1/A$ in calculations of different experimental observables. Therefore, these corrections are much important for very light nuclei.

6.3.3 The interactions

In this work, we have used two different versions of this interaction. The first version, named as ‘sm56fp’ includes only the modifications in $\nu - \nu$ tbmes (without those corresponding to $\nu 1h_{11/2}^{-1} - \nu 1h_{9/2}$) of the collated interaction. Whereas, all modifications in $\nu - \nu$ and $\pi - \pi$ tbmes, the final version of the interaction has been named as ‘sm56fph’.

6.4 The calculation I: Excitation spectra of ^{132}Sn and its neighbour

We have calculated excitation energies and transition probabilities (including B(E1) values) of doubly magic ^{132}Sn . Also, to understand applicability power of the new shell-model Hamiltonian, the excitation spectra of a few neighbouring nuclei around ^{132}Sn with neutron numbers 80, 81 and 82 are calculated.

These are $^{130-134}_{50}\text{Sn}_{80-84}$, $^{131-134}_{51}\text{Sb}_{80-83}$, $^{133-135}_{52}\text{Te}_{81-83}$ and $^{135}_{53}\text{I}_{82}$.

The calculations have been performed using the shell-model code OXBASH [46] and NUSHELLX@MSU [79].

In order to calculate, the excitation spectra of these nuclei, we have put no restriction for $N < 82$ orbitals. In case of nuclei with $N \leq 82$ neutrons, the allowed excitation modes are: (i) no neutron (0p0h) beyond $N > 82$ orbits, or, (ii) at least one neutron excited in any of the three orbits (1p1h), (iii) 2p2h and (iv) maximum one neutron excited in each of the three orbits (i.e. 3p3h). Therefore,

Z = 53		^{135}I 2p2h	
Z = 52	^{133}Te 1p1h	^{134}Te 2p2h	^{135}Te 1p1h
Z = 51	^{132}Sb 2p2h	^{133}Sb 2p2h	^{134}Sb 2p2h
Z = 50	^{131}Sn 3p3h	^{132}Sn 3p3h	
	N = 81	N = 82	N = 83

Figure 6.2: The list of nuclei for which theoretical calculations have been done. The maximum nph excitation mode which was computationally possible in the present calculation has been indicated in the chart.

from no neutron in $N > 82$ orbits (i.e. $0p0h$), $1p1h$, $2p2h$ and $3p3h$ excitations are possible in this choice. For nuclei with neutrons more than 82, $1p1h$, $2p2h$ and $3p3h$ excitation modes are allowed (apart from the neutrons already in $N > 82$ orbitals). However, during the calculation of some of the nuclei, all options were not possible due to our limited computational facilities. Hence, we had to restrict ourselves to $2p2h$ or even $1p1h$ excitations only. The nuclei, for which calculations have been performed, is shown in the chart (Fig. 6.2). For each nuclei, the computationally possible maximum nph excitation mode has also been indicated.

6.5 Results and Discussion - I

6.5.1 Binding Energies

The binding energies (with respect to that of ^{132}Sn) are calculated theoretically in $1p-1h$ option for neutrons (in which case, maximum one neutron can

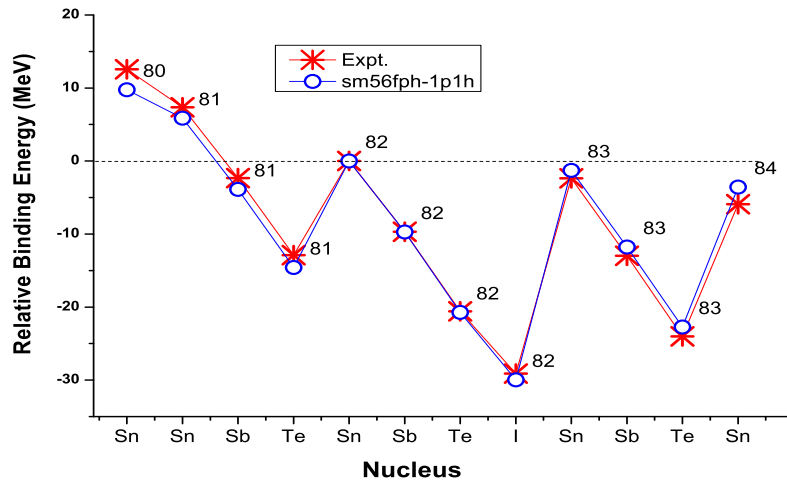


Figure 6.3: Comparison of theoretically calculated and experimental binding energies with respect to ^{132}Sn .

be excited to the orbitals above $N=82$ and with no restriction in the orbits below $N=82$). These are compared with experimental values and a very good agreement is observed as shown in Fig. 6.3. The results are mainly shown for sm56fph interaction.

6.5.2 Excitation Energies

• Calculations for $N=82$ isotones

6.5.2.1 $^{132}_{50}\text{Sn}_{82}$

The excitation energies of ^{132}Sn have been calculated in such a way that there is no restriction for $N < 82$ orbitals and at best one particle (neutron) can be excited up to each of the three orbits for $N > 82$ ($2f_{7/2}$, $1h_{9/2}$ and $3p_{1/2}$). Therefore, with no neutron in $N>82$ orbits i.e. $0p0h$ to $3p-3h$ excitations are allowed. The first excited state 2^+ of ^{132}Sn lies at higher energy (~ 4 MeV) relative to

its neighbouring nuclei as neutron/s has/have to excite across the $N=82$ shell closure. Since the excitations involve a few particle and hole states, the structure of individual states should mostly possess pure multiplet structure. Thus, the low-lying excited states can be described well by particle-hole (p-h) excitations.

P. Bhattacharyya *et al.* [98] have pointed out that the yrast 2^+ , 4^+ , 5^+ , 6^+ , 7^+ , 8^+ , 9^+ states are arising as members of $\nu 1h_{11/2}^{-1}2f_{7/2}$ multiplet. A very good agreement is observed in energy values as shown Fig. 6.4 for 3p3h excitation modes with both the versions, sm56fp and sm56fph interactions. Although, a deviation is also seen for the 8_2^+ state with experimental data.

The positive parity 6_2^+ , 8_2^+ , and 7_2^+ states near 5.4 MeV have been identified as members of $\pi 1g_{9/2}^{-1}1g_{7/2}$ multiplet in the work of Fogelberg *et al.* [107]. But, the $\pi 1g_{9/2}$ orbital is not included in this proposed valence space. Though, 6_2^+ , and 7_2^+ are reproduced well with sm56fp interaction in the present study and these are originating from $\nu 1h_{11/2}^{-1}2p_{3/2}$ multiplet. The 8_2^+ arising from $\nu 1h_{11/2}^{-1}1h_{9/2}$ multiplet shows gross mismatch for results with sm56fp interaction with experimental data. In case of sm56fph, the corresponding *tbmes* relevant for 6_2^+ , 8_2^+ , and 7_2^+ states are adjusted to reproduce them. So, experimental energies of these states show better agreement with sm56fph interaction as depicted in Fig. 6.4.

The level present at the energy 4.352 MeV is identified to be a 3^- state as reported by B. Fogelberg *et al.* [107]. It is expected that the yrast negative

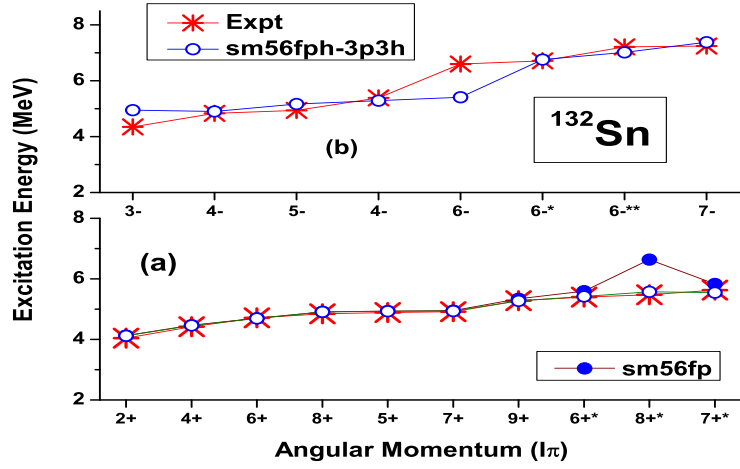


Figure 6.4: Comparison of (a) positive parity and (b) negative parity states in the experimental spectra of ^{132}Sn with theory with 3p3h excitations. The results with *sm56fp* are shown with filled blue bullets and those with *sm56fph* are indicated with open blue bullets. The number of asterisks (N) appearing as superscript in the value of angular momentum in the x-axis label indicate it as the (N+1)th state of that spin.

parity 3_1^- , 4_1^- and 5_1^- states are originating from configuration $\nu 2d_{3/2}^{-1}2f_{7/2}$. Theoretically calculated energies of 4_1^- and 5_1^- states match with experimental data within 100-200 keV for *sm56fph* interaction, without any tuning of the relevant *tbmes*. Whereas, the 3_1^- state is over predicted by ≈ 600 keV compared to experimental level. However, 4_1^- state is arising from the partition $\nu 2d_{3/2}^{-1}2f_{7/2}$ (96%). 5_1^- state has dominant contribution from $\nu 2d_{3/2}^{-1}1h_{9/2}$ (88%) for *sm56fph* interaction. The 5_2^- state calculated at 5.299 MeV is proposed to be a member of the $\nu 2d_{3/2}^{-1}2f_{7/2}$ multiplet. In Ref. [107], the inability of shell model approach to replicate the energy of 3_1^- state has also been discussed. It is stated that, 3_1^- and 5_1^- levels of ^{132}Sn should be present within about 100 keV from each other. The experimental level energy of 5_1^- state is 4.942 MeV. The experimental energy of 3_1^- is around 600 keV lower than other members of the $\nu 2d_{3/2}^{-1}2f_{7/2}$ multiplet. This is a signature of collective nature of this state. It is generated from a coherent superposition of many p-h

configurations. The failure of this present calculation (to be discussed in Sec. 6.5.3) to reproduce the enhanced E3 transition from this state also supports the possible collective nature of this state.

The 6_1^- state, which is arising from the configuration $\nu 2d_{3/2}^{-1}1h_{9/2}$, is also under-predicted in theory. However, 6_2^- , 6_3^- and 7_1^- states coming primarily from $\nu 2d_{5/2}^{-1}2f_{7/2}$ (99%), $\nu 2d_{5/2}^{-1}1h_{9/2}$ (98%) and $\nu 2d_{5/2}^{-1}1h_{9/2}$ (95%) partitions, respectively, are in well agreement with experimental data.

6.5.2.2 $^{133}_{51}\text{Sb}_{82}$

The immediate neighbour of ^{132}Sn , ^{133}Sb , offers an excellent opportunity to examine the single proton states beyond $Z=50$. In low energy excitation region of this nucleus, relatively higher spin states are observed. Those are primarily arising due neutron hole-particle excitation across the shell gap at $N=82$. A few experimental groups [108–112] have studied to extract the experimental data for ^{133}Sb . A high spin, core excited isomeric state of this nucleus was first directly identified at $E_x = 4.56(10)$ MeV with measured half-life of $17 \mu\text{s}$ [113] using the facility isochronous mass spectrometry at GSI. They have estimated a limiting value of half-life for the fully ionized ^{133}Sb nucleus corresponding to a totally disabled internal conversion decay mode. Eventually, in 2016, the informations about the core-excited states of ^{133}Sb above the isomer $21/2^+$ state had been extracted from the cold neutron induced fission of ^{241}Pu and ^{235}U in an experiment performed at ILL reactor in Grenoble [99]. The properties of such core excited states, provide a chance to test our newly formulated shell

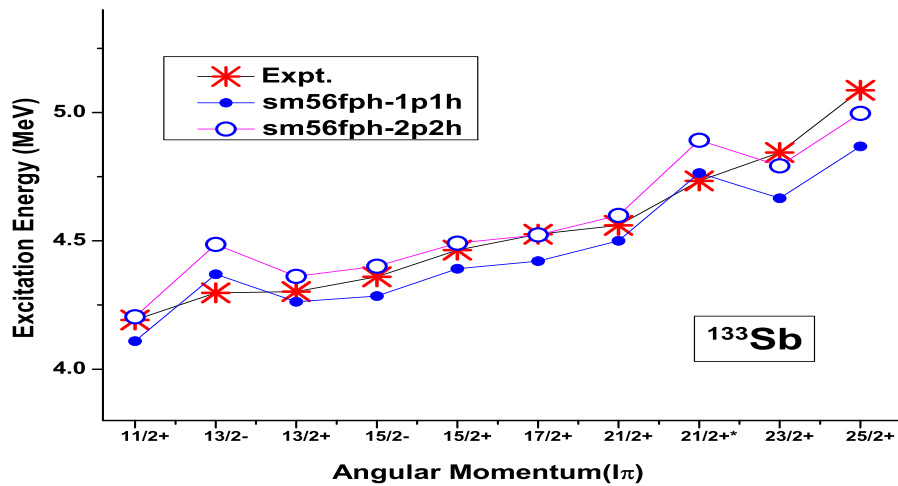


Figure 6.5: Comparison of experimental spectra of high spin states in ^{133}Sb with theory. More details are included in the legend, caption of Fig. 6.4 and the text.

model interaction.

In case of ^{133}Sb , the calculations have been done for both 1p1h and 2p2h excitation options with sm56fph interaction. Similarly, in this case also, no restriction has been put for the neutrons $N < 82$ orbitals. The 3p3h excitations can not be calculated due to limitation in available computational facilities. In Fig. 6.5, results for both 1p1h as well as 2p2h are shown.

In the present calculation, $3/2^+$ and $11/2^-$ at the energy 2.44 MeV and 2.792 MeV respectively, can not be reproduced as these states are arising from single proton excitation to $\pi 2d_{3/2}$ and $\pi 1h_{11/2}$ orbitals respectively. However, these orbits are not included in our proposed model space. Therefore, these states are not included in the Fig. 6.5.

Although, the positive and negative parity states observed in higher energy region (> 4 MeV) mainly arising from core-excitation show good agreement in 2p2h excitation mode in current calculation as shown in Fig. 6.5. The positive

parity yrast states, such as $11/2^+$, $13/2^+$, $15/2^+$, $17/2^+$ and $21/2^+$ states originated mainly from the configuration $\pi 1g_{7/2}-\nu 1h_{11/2}^{-1}2f_{7/2}$ with 90-94% major contribution. The $21/2_2^+$, $23/2_1^+$ and $25/2_1^+$ have leading contribution (96%, 89% and 97% respectively) from the partition $\pi 1g_{7/2}-\nu 1h_{11/2}^{-1}1h_{9/2}$.

Whereas, the negative parity $13/2_1^-$ and $15/2_1^-$ states have major contributions (86% and 70% respectively) from partition $\pi 1g_{7/2}-\nu 2d_{3/2}^{-1}2f_{7/2}$. In present calculation, the 2p2h option can successfully replicate experimental excitation energy of all core excited states except for the $13/2_1^-$ and $21/2_2^+$ states, where 1p1h option shows better agreement.

6.5.2.3 $^{134}_{52}\text{Te}_{82}$

^{134}Te can be described as two valence protons outside the doubly closed ^{132}Sn core. Most of the experimental information have been extracted from coincidence measurements of prompt and delayed gamma ray cascades of fission fragments emitted following spontaneous fission using large arrays of γ -detector [114–118].

At low excitation near up to $\simeq 3$ MeV, the states are primarily originating from proton excitations within the shell. In this energy region, the two most important partitions are $\pi 1g_{7/2}^2$ and $\pi 1g_{7/2} - 2d_{5/2}$. As shown in Fig. 6.6 (lower panel), results obtained from this work with 2p2h excitations of sm56fph interaction show a very good agreement with experimental data, even for these low spins. Now, above 3 MeV (but < 4.5 MeV), a few negative parity states are also observed. It is expected that these -ve states are coming from the mul-

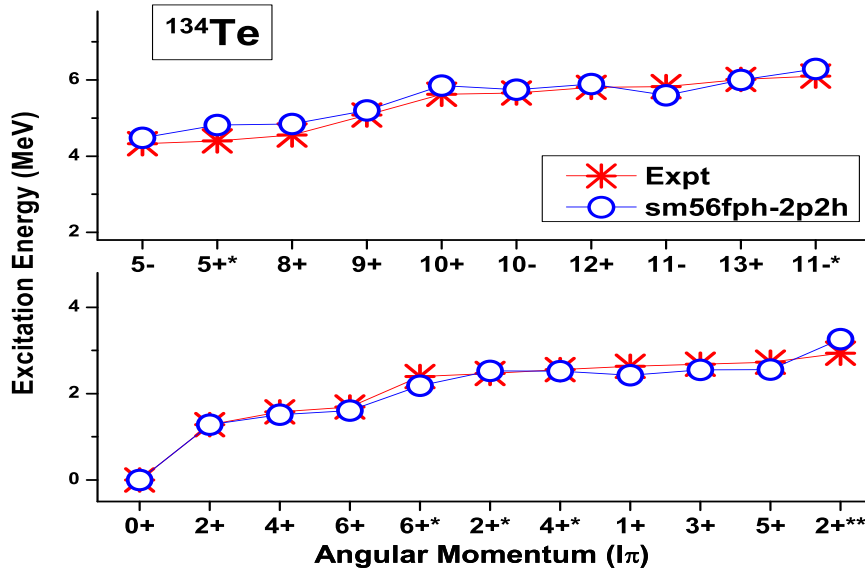


Figure 6.6: Comparison of experimental spectra of ^{134}Te with theory.

triplets of $\pi 1g_{7/2}1h_{11/2}$. Since the present model space does not include $\pi 1h_{11/2}$ orbit, these states are not reproduced. As, in our present model space to create a negative parity state, a neutron has to be excited beyond the shell gap, the energies of these states resulted in the higher excitation energy. In Fig. 6.6 we have not included these states.

At excitation energy 4.558 MeV [118], 8^+ state is the first excited state that involves excitations across the neutron core. These positive parity states are considered to be members of the multiplets of $\pi 1g_{7/2}^2 - \nu 1h_{11/2}^{-1}2f_{7/2}$. Results obtained for 2p2h excitation mode for smfph interaction are shown in the Fig. 6.6. In present calculation, 8_1^+ state at an energy 4.843 MeV, has this particular configuration with around 90% amplitude. The 9_1^+ state is arising from $\pi 1g_{7/2}^2 - \nu 1h_{11/2}^{-1}1h_{9/2}$ with nearly 70% amplitude. The 10_1^+ state, which is theoretically predicted at 5.85 MeV ($E_{\text{expt}} = 5.621$ MeV), has a mixed configuration with

$\pi 1g_{7/2}^2 - \nu 1h_{11/2}^{-1} 2f_{7/2}$ ($\simeq 59\%$), $\pi 1g_{7/2} 2d_{5/2} - \nu 1h_{11/2}^{-1} 2f_{7/2}$ ($\simeq 36\%$). The yrast 12^+ (13^+) state has major contribution of $\simeq 45\%$ (31%) $\pi 1g_{7/2}^2 - \nu 1h_{11/2}^{-1} 2f_{7/2}$ and $\simeq 48\%$ (65%) $\pi 1g_{7/2} 2d_{5/2} - \nu 1h_{11/2}^{-1} 2f_{7/2}$ partition.

The negative parity state 10_1^- ($E_{\text{expt}}=5.658$ MeV) predicted to be at 5.746 MeV has mixed composition with 45% contribution from the partition $\pi 1g_{7/2}^2 - \nu 2d_{3/2}^{-1} 2f_{7/2}$ and 24% from $\pi 1g_{7/2} 2d_{5/2} - \nu 2d_{3/2}^{-1} 2f_{7/2}$. The 11_1^- has 77% contribution arising from $\pi 1g_{7/2}^2 - \nu 2d_{3/2}^{-1} 1h_{9/2}$. On the other hand, 11_2^- has 72% contribution from the partition $\pi 1g_{7/2} 2d_{5/2} - \nu 2d_{3/2}^{-1} 1h_{9/2}$. So, the theoretical calculation is showing a overall good agreement with available experimental data.

6.5.2.4 $^{135}_{53}\text{I}_{82}$

The experimental information about the excited states of this odd nucleus, ^{135}I have been mainly gathered from the decay [119] of ^{135}Te and the prompt γ -ray spectroscopy of the spontaneous fission fragments of ^{248}Cm [116, 118].

Three valence protons outside the $Z=50$ core are primarily responsible for the low-lying yrast excitations. The low-lying states, observed within 1.5 MeV (such as, $7/2_1^+$, $9/2_1^+$, $11/2_1^+$, $15/2_1^+$) have dominant configuration of $\pi 1g_{7/2}^3$. Theoretical results, represented in Fig. 6.7 show good agreement with available data. On the other hand, the $5/2_1^+$ and $17/2_1^+$ states show major participation of $\pi 1g_{7/2}^2 2d_{5/2}$ partition. Also, a few negative parity states are seen at excitation energies within 3.5 MeV to 4 MeV. Such -ve parity states are expected to originate from the multiplets of $\pi 1g_{7/2}^2 1h_{11/2}$. This is beyond the scope of this

present calculation due to absence of $\pi 1h_{11/2}$ orbit. So, these particular states are not included in the Fig. 6.7.

In ^{135}I , the states arising from the neutron core excitations have been observed after 4 MeV. Results calculated with 1p1h excitations and 2p2h excitations for sm56fph interaction are shown in Fig. 6.7. With 2p2h excitations mode of sm56fph, the positive parity states ($19/2_1^+$, $21/2_1^+$, and $23/2_1^+$) are reproduced better. The yrast $19/2^+$, $21/2^+$ states have $\approx 55\%$ and 42% (57% and 45%) contributions arising from $\pi 1g_{7/2}^2 2d_{5/2} - \nu 1h_{11/2}^{-1} 2f_{7/2}$ and $\approx 36\%$ and 48% (35% and 46%) from $\pi 1g_{7/2}^3 - \nu 1h_{11/2}^{-1} 2f_{7/2}$ partitions with 2p2h (1p1h) modes. For yrast $23/2^+$ state, both the modes of excitations (i.e. 1p1h and 2p2h) estimate $\approx 75\%$ contribution from $\pi 1g_{7/2}^3 - \nu 1h_{11/2}^{-1} 2f_{7/2}$ partition. Also, for yrast $25/2^+$ state, a deviation of around 130 keV is observed for both the modes. They have common major structure of $\pi 1g_{7/2}^3 - \nu 1h_{11/2}^{-1} 1h_{9/2}$ with $\approx 83\%$ contributions. In Fig. 6.7, the limitation of sn100pn interaction to predict the core-excited states is depicted.

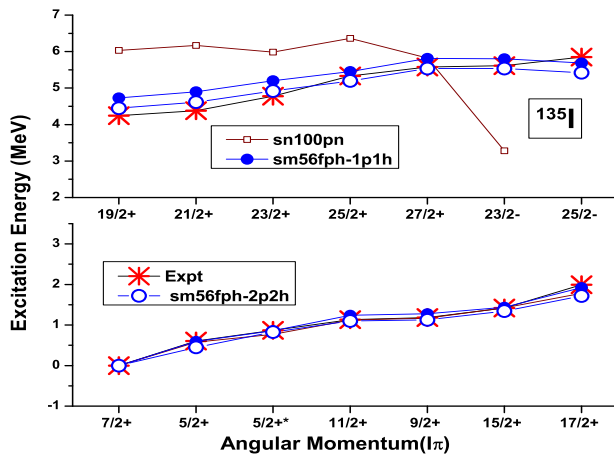


Figure 6.7: Comparison of experimental spectra of ^{135}I with theory.

After excitation energy of 5.7 MeV, core excited negative parity states $23/2_2^-$ ($25/2_1^-$) are noticed [118]. The $23/2_2^-$ state matches better with theoretical prediction for 2p2h excitation. The composition of the state has $\simeq 53\%$ (50%) contribution from $\pi 1g_{7/2}^2 2d_{5/2} - \nu 2d_{3/2}^{-1} 2f_{7/2}$ for 1p1h (2p2h excitation). Experimentally observed $25/2^-$ state at $E_x=5.849$ MeV matches with $25/2_1^-$ state with $\simeq 67\%$ contribution from $\pi 1g_{7/2}^2 2d_{5/2} - \nu 2d_{3/2}^{-1} 1h_{9/2}$ for 1p1h excitation. Whereas, for 2p2h mode, an deviation in excitation energy around 400 keV is noted while the state has $\simeq 57\%$ contribution from $\pi 1g_{7/2}^2 2d_{5/2} - \nu 2d_{3/2}^{-1} 2f_{7/2}$ partition.

- **Calculations for N=81 isotones**

6.5.2.5 $^{131}_{50}\text{Sn}_{81}$

This odd A nucleus has a single neutron hole coupled to the doubly closed ^{132}Sn . Hence, one can gather information about the single hole states. These informations are important parameters for nuclear shell model calculations. Experimentally, the information about the single hole states ($1g_{7/2}$, $2d_{3/2}$, $3s_{1/2}$) in ^{131}Sn have been obtained from β -decay experiments performed by De Geer and Holm [120]. There is some uncertainties regarding the relative position of the $11/2_1^-$ state. This particular state is a β -decaying isomer. Several experiments have been performed for precise determination of the excitation energy of $11/2_1^-$ state [121–123]. The most recently adopted data as obtained from NNDC site, reports the energy obtained from the β spectrum is 69 (14) keV,

whereas it is 65.1 (3) keV from the level scheme [18]. In the present work, this energy is predicted at 36 keV for 3p3h mode of excitation with sm56fph interaction. The trend of other excited states in low energy region, such as, $1/2_1^+$, $5/2_1^+$, $7/2_1^+$ at 0.332 MeV, 1.655 MeV, 2.434 MeV, respectively, as determined from the decay studies [120, 123] are in good agreement with the calculated spectra as shown in Fig. 6.8. However, the theoretically estimated values do not exactly match with the experimental data for $1/2_1^+$ and $7/2_1^+$ states.

The higher core excited states are observed within the energy range 4-5 MeV. These excited states are populated from the spontaneous fission of ^{248}Cm and it had been studied via prompt-delayed gamma spectroscopy as described in Ref. [98]. The positive parity states $13/2_1^+$, $15/2_1^+$, $17/2_1^+$ and $19/2_1^+$ are majorly originating from the configuration of $\nu 2d_{3/2}^{-1} 1h_{11/2}^{-1} 2f_{7/2}$ with the purity gradually increasing ranging from $\simeq 82\%$ to 95% . The $15/2_2^+$ state, although emerging from the similar configuration has much less purity ($\simeq 61\%$). The $17/2_2^+$ arises from $\nu 2d_{3/2}^{-1} 1h_{11/2}^{-1} 1h_{9/2}$ partition with 82% contribution.

The $15/2_1^-$, $17/2_1^-$, $19/2_1^-$, $21/2_1^-$, and $23/2_1^-$ states are originating with leading structure $\nu 1h_{11/2}^{-2} 2f_{7/2}$ with 94% , 83% , 96% , 88% and 94% parentage, respectively. These states have been compared with theoretical prediction by considering the excitation energy of the $11/2_1^-$ isomer as zero.

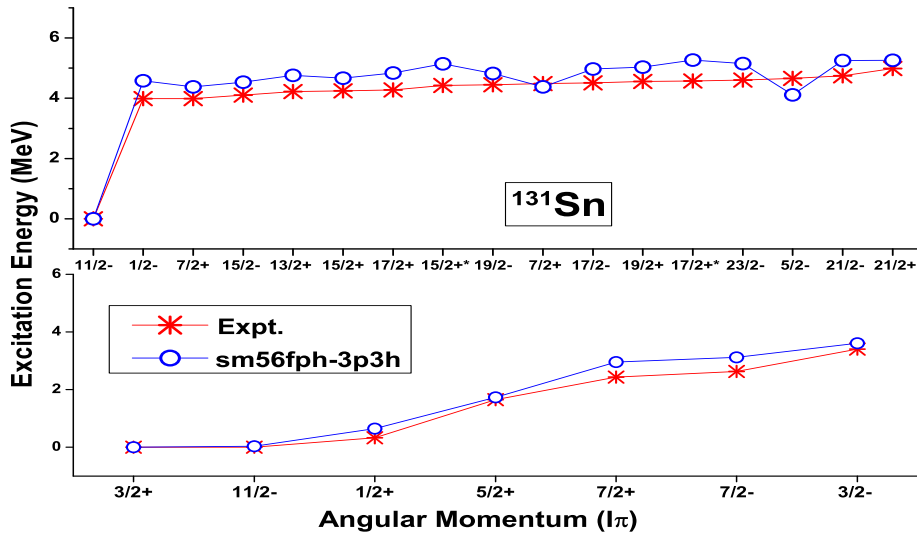


Figure 6.8: Comparison of experimental spectra of ^{131}Sn with theory.

6.5.2.6 $^{132}_{51}\text{Sb}_{81}$

This odd-odd isotope is described as one proton particle and one neutron hole outside the doubly closed ^{132}Sn . The low-lying states are arising primarily from the interaction between the single proton and the single neutron hole. Several experimental findings about this nucleus are reported in Refs. [124–126].

From earlier works, the 4^+ (ground state) as well as 3_1^+ state have been identified to be composed via coupling between $\pi 1g_{7/2} - \nu 2d_{3/2}^{-1}$. The present calculations are also able to reproduce the sequence as well the composition following earlier reports as shown in Fig. 6.9. The 3_1^+ state, which is predicted theoretically at an energy of 135 keV, is observed at experimental level of 85.55(6) keV. This particular state is also an isomer having $T_{1/2} = 15.62(13)$ ns [18].

The low-lying 8_1^- isomer, whose experimental level energy is yet to be determined precisely, is produced at 193 keV in the current calculations. It is originating with a major configuration of $\pi 1g_{7/2} - \nu 1h_{11/2}^{-1}$. This state is identified to be a beta decaying isomer with half-life of 4.10(5) min. As found in NNDC site [18], its excitation energy is not determined properly but it is predicted to be around 150-250 keV above the ground state [125]. Also, this level is specified at 200 keV with an uncertainty of 30 keV in the atomic mass database [127]. The other members of $\pi 1g_{7/2} - \nu 1h_{11/2}^{-1}$ multiplet such as, $I = 3_1^-, 4_1^-, 6_1^-, 9_1^-$ are also experimentally observed. As per calculation, in most of the cases, the purity of this structure is more than 95%.

After 2.5 MeV, as mentioned by P. Bhattacharyya *et al.*, two positive parity states 10^+ , 11^+ states are observed and these are populated from the fission of ^{248}Cm [128]. These two are originated from coupling of $\pi 1h_{11/2} - \nu 1h_{11/2}^{-1}$ at energies 2.8 and 3.2 MeV, respectively. Due to absence of $\pi 1h_{11/2}$ orbit, we are unable to reproduce these states.

Above 4 MeV, a few more positive (11^+ , 12^+ , 13^+) and also negative (12^- , 13^- , 14^- , 15^-) parity levels are noted. In order to generate spin more than 11, the core has to be excited. That means, at least one neutron has to be excited to orbitals across the N=82 shell gap. These high spin states have been observed to decay to 8^- isomer. As the energy is not well known, we have compared theoretical estimations considering the 8_1^- (theory) state (i.e. 193 keV) to be zero. Now, the 11^+ state is arising majorly from the multiplet $\pi 1g_{7/2} - \nu 1h_{11/2}^{-1} 2d_{3/2}^{-1} 2f_{7/2}$ having 84% contribution. However, the other states,

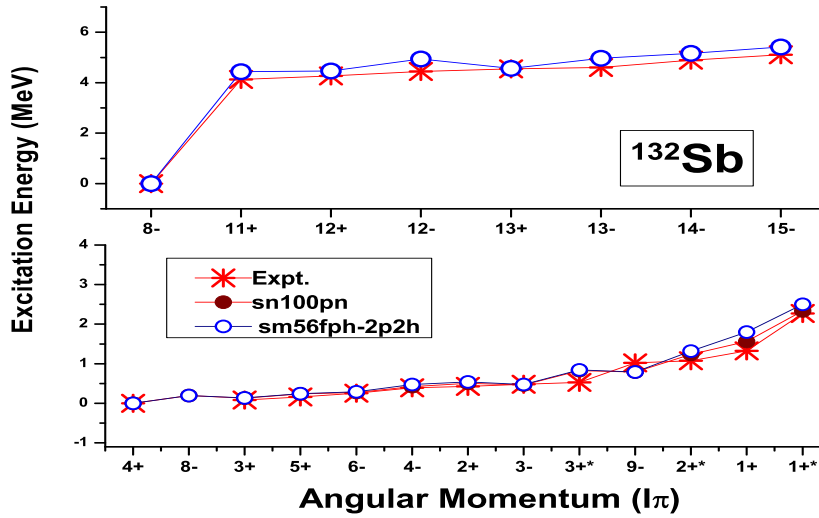


Figure 6.9: Comparison of experimental spectra of ^{132}Sb with theory.

like 12^+ and 13^+ have structure of $\pi 1g_{7/2} - \nu 1h_{11/2}^{-1} 2d_{3/2}^{-1} 1h_{9/2}$ with 86% and 90% parentage. However, the negative parity states (12^- to 15^-) have leading contribution around 90-96% from $\pi 1g_{7/2} - \nu 1h_{11/2}^{-2} 2f_{7/2}$ partition.

6.5.2.7 $^{133}_{52}\text{Te}_{81}$

^{133}Te can be characterised as ^{132}Sn with additional two proton particles and one neutron hole. The second excited state ($11/2^-$) of this nucleus ($E_x = 0.334$ MeV) is a beta decaying isomer with half-life, $T_{1/2} = 55.4$ (4) min. Theoretically, it is predicted to be at energy of 413 keV. The experimental details of $3/2^+$ (ground state), $1/2^+$ state below this isomer and other low-spin states have been gathered from β^- decay of ^{133}Sb [18].

The theoretical results predicted using sm56fph interaction are compared with experimental data as shown in Fig. 6.10. A comparison with sn100pn interaction is also presented. The positive parity yrast states $3/2^+$, $5/2^+$ are

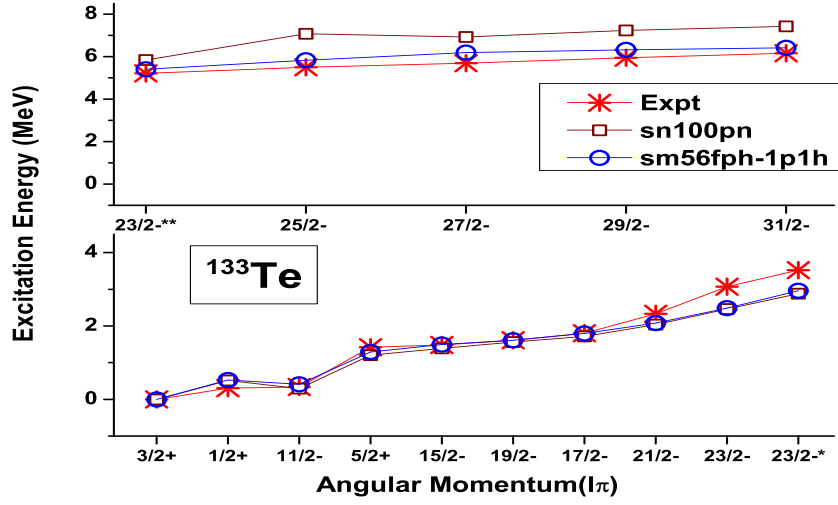


Figure 6.10: Comparison of experimental spectra of ^{133}Te with theory.

originating from the dominant configuration $\pi 1g_{7/2}^2 - \nu 2d_{3/2}^{-1}$ with contributions 93% and 74%, respectively. On the other hand, $1/2^+$ state is arising with major partition $\pi 1g_{7/2}^2 - \nu 3s_{1/2}^{-1}$ of 74% amplitude.

The yrast isomer $11/2^-$ state and other members of this sequence, such as, $15/2_1^-$, $17/2_1^-$, $19/2_1^-$, $23/2_1^-$ have been originated with the configuration $\pi g_{7/2}^2 - \nu h_{11/2}^{-1}$ with more than 90% parentage. The $21/2_1^-$ state has a mixed structure with 52% contribution from the partition arising from $\pi g_{7/2}^2 - \nu h_{11/2}^{-1}$ and 46% from $\pi 1g_{7/2} 2d_{5/2} - \nu 1h_{11/2}^{-1}$. The second $23/2^-$ state has leading partition from $\pi 1g_{7/2} 2d_{5/2} - \nu 1h_{11/2}^{-1}$ (98%), as also proposed in the study of Hwang *et al.* [129].

The excitation energies of +ve parity states observed near 4 MeV, (such as, $21/2^+$, $25/2^+$, $23/2^+$, $27/2^+$) can not be calculated properly in the current calculations. Hwang *et al.* [129] have pointed out that these states are arising from $\pi 1g_{7/2} 1h_{11/2} - \nu 1h_{11/2}^{-1}$. So, these energies can not be reproduced in our

calculations due to the unavailability of the proton $1h_{11/2}$ orbit in the model space.

Hwang *et al.* [129] also suggested that the sequence of states, starting at 5.2 MeV in ^{133}Te are arising from the particle-hole excitation from the ^{132}Sn core. In our calculation, the $23/2_3^-$ and $25/2_1^-$ have leading contribution (around 86% and 71% respectively) from the configuration $\pi 1g_{7/2}^2 - \nu 1h_{11/2}^{-2} 2f_{7/2}^{-1}$. However, the other members, such as, $27/2_1^-$, $29/2_1^-$ and $31/2_1^-$ have mixed structure arising from both $\pi 1g_{7/2} 2d_{5/2} - \nu 1h_{11/2}^{-2} 2f_{7/2}^{-1}$ (61-75%) and $\pi 1g_{7/2}^2 - \nu 1h_{11/2}^{-2} 2f_{7/2}^{-1}$ (30-21%). The results obtained using *sn100pn* interaction show a substantial deviation from experimental data, as expected.

- **Calculations for N=83 isotones**

6.5.2.8 $^{134}_{51}\text{Sb}_{83}$

^{134}Sb consists of one proton and one neutron particle outside the doubly closed ^{132}Sn core. The theoretical calculations are performed with CWG interaction as well as with 1p1h and 2p2h excitations modes of *sm56fph* interaction. It is compared with experimental data as shown in Fig. 6.11. Both of the modes are able to replicate the experimental findings for higher spin states much better than those estimated by CWG interaction.

From the adopted decay scheme, it is noted that ^{134}Sb has a beta decaying isomer having $T_{1/2} = 10.07$ (5)s at spin 7^- . The details of low-lying struc-

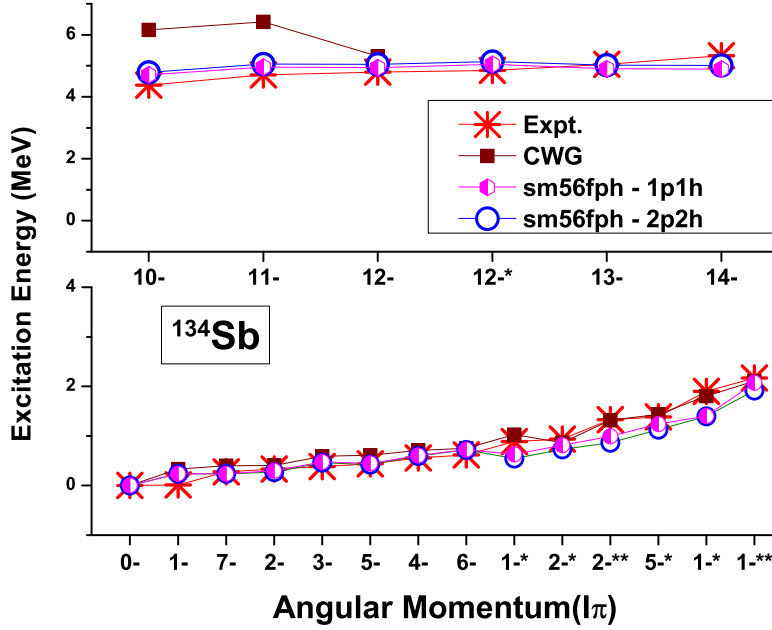


Figure 6.11: Comparison of experimental spectra of ^{134}Sb with theory.

ture are extracted from β^- and β^-n decay of $^{134,135}\text{Sn}$, respectively mentioned in Ref. [130]. There is an experimentally observed 1^- state, which is almost degenerate to 0^- at an energy 13 keV. Both, CWG and sm56fph interactions are failed to match the low-lying 1^- state. The yrast ranging from spin 0^- to 7^- states are majorly coming from the partition $\pi 1g_{7/2} - \nu 2f_{7/2}$. Whereas, the second 1^- state is originating from the partition $\pi 1g_{7/2} - \nu 1h_{9/2}$. Also, the 2_2^- and 2_3^- states have around 70% contributions arising from $\pi 1g_{7/2}$ coupled with neutron in $1h_{9/2}$ and $3p_{3/2}$, respectively. The 5_2^- state has a dominant contribution 59% from the partition $\pi 1g_{7/2} - \nu 3p_{3/2}$. Now, near excitation energy of 2 MeV, 1_3^- and 1_4^- are mainly formed via coupling of proton at $2d_{5/2}$ with neutron in $2f_{7/2}$ (94%) and $3p_{3/2}$ (95%), respectively.

After the excitation energy of 2 MeV, 9^+ and 10^+ states are observed. In theory, these are originated with leading contribution from the partitions $\pi 1h_{11/2} - \nu 2f_{7/2}$ and $\pi 1g_{7/2} - \nu 1i_{13/2}$, respectively, as proposed in Ref. [131]. But, our calculation predicts these particular states to be at higher energies due to absence of proton $1h_{11/2}$ and neutron $1i_{13/2}$ orbits in the assigned model space.

The high spin negative parity states are generally, originated from the neutron excitation through the $N=82$ shell gap. For, $2p2h$ mode with $sm56fph$ interaction, the yrast 10^- state has the structure of $\pi 1g_{7/2} - \nu 1h_{11/2}^{-1} 2f_{7/2}^2$ with 73% parentage. The other negative parity yrast, such as, 11^- to 14^- states have originated from the partition $\pi 1g_{7/2} - \nu 1h_{11/2}^{-1} 2f_{7/2} 1h_{9/2}$ gradually increasing contribution spanning over 49% to 92%. This structure is different from the partition $(\pi 1g_{7/2} - \nu 1h_{11/2}^{-1} 2f_{7/2}^2)$ mentioned by Fornal *et al.* in Ref. [131].

6.5.2.9 $^{135}_{52}\text{Te}_{83}$

The nucleus, ^{135}Te can be described to be composed of two proton particles and one neutron particle outside doubly magic ^{132}Sn nucleus. The information about the low-lying states of this nucleus have been obtained from Hoff *et al.* [132]. Much more information about the isomeric state are mentioned in Kawade *et al* [133]. Additionally, the information about high spin states can be collected from the Ref. [131, 134, 135]. The theoretically calculated results using CWG interaction and $1p1h$ excitations mode with $sm56fp$ and $sm56fph$ interactions are compared with existing experimental results as shown in Fig. 6.12. It is noted that, both $sm56fp$ and $sm56fph$ interactions reproduce the

experimental result better than the predictions made using CWG interaction in case of high spin states.

Now, low-lying states ($7/2^-$, $11/2^-$, $15/2^-$) are originating majorly from the partition $\pi 1g_{7/2}^2 - \nu 2f_{7/2}$ with contributions approximately 94%, 91% and 82% respectively for sm56fp interaction. Similarly, for sm56fph interaction these state are predicted to arise from the same leading configuration along with approximately 93, 87 and 82%, respectively, amplitude. The yrast $3/2^-$ state is originated from the partition $\pi 1g_{7/2}^2 - \nu 3p_{3/2}$ with 75% contribution for sm56fp and 73% for sm56fph interaction. In case of, $1/2^-$ and $5/2^-$ states, the leading configuration is $\pi 1g_{7/2}^2 - \nu 2f_{7/2}$. These states have 78% (77%) and 71% (65%), respectively amplitude for sm56fp (sm56fph) interaction. The $9/2_1^-$ state has major contribution 95% from the partition $\pi 1g_{7/2}^2 - \nu 1h_{9/2}$, for sm56fph interaction.

Also, yrast $19/2^-$ state is arising from mixed structure $\pi 1g_{7/2}^2 - \nu 2f_{7/2}$ with 47%(48%) and $\pi 1g_{7/2}2d_{5/2} - \nu 2f_{7/2}$ with 53%(50%) contributions for sm56fp (sm56fph) interaction. The $19/2_2^-$ has dominant part of $\pi 1g_{7/2}^2 - \nu 2f_{7/2}$ partition with 53%(50%) and $\pi 1g_{7/2}2d_{5/2} - \nu 2f_{7/2}$ with 47%(48%) for sm56fp (sm56fph) interaction. The $19/2_3^-$ has leading contribution of 78% from the partition $\pi 1g_{7/2}^2 - \nu 1h_{11/2}^{-1}2f_{7/2}^2$ for sm56fp. On the contrary, in case of sm56fph it has a contribution of 98% coming from $\pi 1g_{7/2}^2 - \nu 1h_{9/2}$ partition. The yrast $21/2^-$ is originated from $\pi 1g_{7/2}^22d_{5/2} - \nu 1h_{11/2}^{-1}2f_{7/2}^2$ partition with 52% contribution as estimated by sm56fp interaction. But, in case of sm56fph interaction, the leading contribution is arising from $\pi 1g_{7/2}^2 - \nu 1h_{9/2}$ (86%). It is noted that,

the $21/2^-$ state has $\pi 1g_{7/2}^2 - \nu 1h_{11/2}^{-1} 2f_{7/2}^2$ with 52% along with competing contribution of 36% from $\pi 1g_{7/2} 2d_{5/2} - \nu 1h_{11/2}^{-1} 2f_{7/2}^2$ for *sm56fp*. For *sm56fph*, this state arises from $\pi 1g_{7/2} 2d_{5/2} - \nu 1h_{9/2}$ with 86% contribution.

It is also analysed that the $23/2^-$, $25/2^-$, $27/2^-$, $29/2^-$, $31/2^-$, $33/2^-$ and $35/2^-$ states have contributions from $\pi 1g_{7/2}^2 - \nu 1h_{11/2}^{-1} 2f_{7/2}^2$ and $\pi 1g_{7/2} 2d_{5/2} - \nu 1h_{11/2}^{-1} 2f_{7/2}^2$ with amplitudes ranging from 41% - 13% and 31% - 86% for *sm56fp* interaction.

For *sm56fph* interaction, the negative parity states, such as, $23/2^-$, $25/2^-$, $27/2^-$, $29/2^-$, $31/2^-$, $33/2^-$ and $35/2^-$ are originating from a mixed structure of configurations of $\pi 1g_{7/2}^2 - \nu 1h_{11/2}^{-1} 2f_{7/2} 1h_{9/2}$ and $\pi 1g_{7/2} 2d_{5/2} - \nu 1h_{11/2}^{-1} 2f_{7/2} 1h_{9/2}$ with contributions ranging from 86%-25% and 2-74%.

Some of the +ve parity states (such as, $21/2^+$, $25/2^+$, $27/2^+$ etc.) can not be matched with experimental data with these two specified interactions because of unavailability of proton $1h_{11/2}$ orbital in the model space, as described earlier.

6.5.3 Transition Probabilities in ^{132}Sn and its neighbours

In this section, the transition probabilities of yrast states, which are originating from cross-shell excitations in ^{132}Sn , ^{131}Sn , ^{133}Sb and ^{134}Te isotopes have been calculated (Table 6.4) for *sm56fph* interaction and compared with experimen-

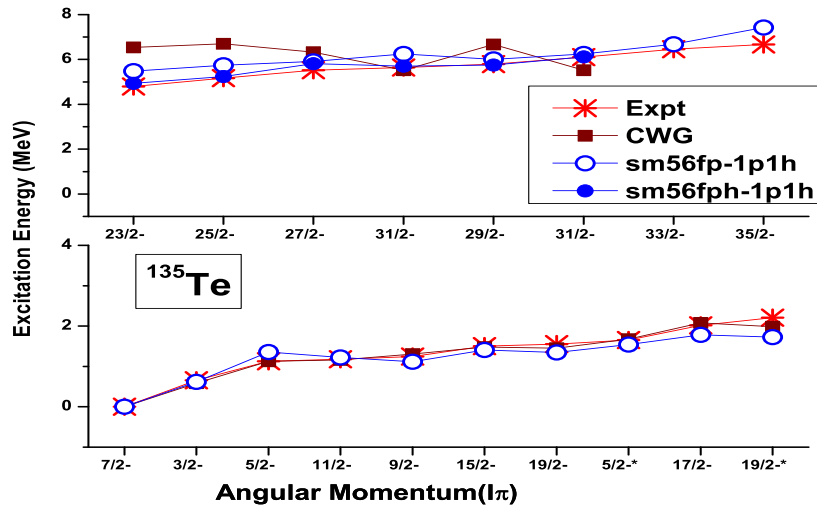


Figure 6.12: Comparison of experimental spectra of ^{135}Te with theory.

tal data wherever available [18].

6.5.3.1 Effective charges

In a restricted model space, the electromagnetic properties of the many nucleon system are reproduced by introducing model operators, effective charges and effective gyromagnetic factors [96, 136]. If the motion of protons and neutrons associated with recoil effects is considered, both nucleons must acquire effective charges. These charges depend on the multipolarity of the transition and also on the nature of the associated single-particle wave-functions. This effect is particularly important in case of electric dipole (E1) transitions. Both neutron and proton effective charges are important for reproducing the experimental values of $B(E1)$, even for nuclei having no valence proton (such as for Sn isotopes in the current work). Although, transition rate of higher multipolarity $B(E1)$ (i.e. $l > 1$), absence of valence proton (neutron) make the calculated

values independent of effective proton (neutron) charges. For nuclei having no valence proton, the $B(E1)$ values increase with increasing e_n^{eff} . But, for nuclei having both active valence protons and neutrons, increase in proton (neutron) effective charge increases (decreases) $B(E1)$ values.

6.5.3.2 Comparison with experimental data

- *Nuclei with only valence neutrons:*

Hence, for $^{131,132}\text{Sn}$, except for $B(E1)$ results, only neutron effective charges, e_n^{eff} are mentioned in Table 6.4. In case of $E\lambda$ ($\lambda=2-4$) the neutron effective charge is taken as $1.2e$. Due to the limitation in computational facilities, only a few cross-shell neutron excitations are considered. Therefore, a higher neutron effective charge has to be used to reproduce the experimental data. The results for all modes of excitation are shown in the table. The results reproduce data reasonably well for ^{132}Sn , except in a few cases (for 8^+ to 6^+ and those involving the 3^- state). In case of magnetic transitions, quenched intrinsic neutron g -factor (g_n^s) by a factor of 0.7, improves the results considerably.

In case of $E3$ transition from the 3_1^- state, a gross mismatch is observed. It has been already noted that this particular state (3_1^- state) possibly has a collective structure. Hence, its energy as well as transition rates are not reproduced with such limited options for excitations in this present calculation.

During the calculation of $E1$ transition, effective charge has been taken as $e_n^{eff} = 0.35e$ and $e_p^{eff} = 1.64e$ (Table 6.4). However, the theoretically pre-

dicted values are underestimated compared to experimental data by one order of magnitude in most of the cases. On the other hand, for E1 transitions from $5_1^- \rightarrow 4^+$ state, the $B(E1)$ value is well reproduced. Whereas, the $B(E1)$ value for $5_1^- \rightarrow 6^+$ state shows over-prediction relative to the experimental data.

In the present model space, the $2f_{5/2}$, $3p_{1/2}$, and $1i_{13/2}$ orbits have been excluded. These orbitals are not usually significant for reproduction of excitation energies or transition probabilities (except for E1) of the nuclei which are being discussed in this work. However, this argument does not hold for E1 transition probabilities, *i.e.* for $B(E1)$ values. These transitions occur due to (very) small but finite contributions of the orbitals originating in higher shells in the wave-function. Hence, this small overlap in wave-functions has significance for proper reproduction of experimental $B(E1)$ values, which are generally at least 5-6 orders of magnitude slower than the single particle estimate.

For ^{131}Sn , the $B(E2:23/2^- \mapsto 19/2^-)$ has been reproduced with the same effective charge ($e_n^{eff} = 1.2e$) to a reasonable extent. However, the $B(E1)$ and $B(E4)$ values are under-predicted. A similar mismatch of theoretical $B(E1)$ value with experimental data has been reported for ^{133}Ba in a recent work by Kaya *et al.* [137].

- *Nuclei with both valence protons and neutrons:*

For ^{133}Sb , with one valence proton along with neutrons, the calculated $B(E2)$

value of the $21/2^+ \rightarrow 17/2^+$ transition from the microsecond $21/2^+$ isomer (without the internal conversion correction) also yields a milli-second half-life of the isomer as reported in the work of B. Sun *et al.* [113]. For exact reproduction of the B(E2), effective proton charge needs to be greater than 2. Although, the sharp difference between experimental B(M1) values extracted for the $15/2^+ \rightarrow 13/2^+$ and $13/2^+ \rightarrow 11/2^+$ transitions could not be reproduced for the calculated yrast states for both 1p1h and 2p2h modes of excitation. However, a better reproduction in excitation energy is observed for 2p2h mode. A similar kind of observation is reported in Wang *et al.* [94]. In ^{134}Te , with two valence protons along with neutrons, calculated B(E2) for 12^+ is also under-predicted in present calculation. It indicates a need for higher proton effective charge.

Thus, calculation of B(E2)s in two of these nuclei, even with neutron effective charge as zero with effective charge of proton as 2, the B(E2) values are under-predicted. Possibly availability of only two active orbitals for protons in the model space is responsible for the need of large effective proton charge.

6.6 The calculation II: Determination of B(E1: $5^-_1 \rightarrow 4^+_1$) of Sn isotopes

As proposed in the section 6.2, we want to evaluate the B(E1) values theoretically. Now, full space of calculation in mid-shell is very difficult due to large

Table 6.4: The comparison of theoretical transition rates of yrast states which arise from cross-shell excitations in ^{132}Sn , ^{131}Sn , ^{133}Sb and ^{134}Te isotopes with experimental data [18]. The B(M1) values are quoted in μ_n^2 . The B(E λ) values are quoted in unit of $e^2 fm^{2\lambda}$. The B(E1) values are quoted in the unit of $10^{-6} e^2 fm^2$.

$^A X$	J_i	J_f	Type	Expt. (Error)	Effective charges		Theory		
					e_p	e_n	1p1h	2p2h	3p3h
^{132}Sn									
	2 ⁺	0 ⁺	E2	224.6 (6)	-	1.2	235.3	232.8	232.9
	4 ⁺	2 ⁺	E2	16.3 (10)	-	"	3.4	3.3	3.0
	6 ⁺	4 ⁺	E2	11.9 (4)	-	"	8.1	8.3	8.0
	8 ⁺	6 ⁺	E2	4.2 (1)	-	"	0.49	0.48	0.26
	5 ⁻	3 ⁻	E2	24.9(3)	-	"	0.09	0.041	0.05
	3 ⁻	0 ⁺	E3	>7348.4	-	1.2	82.3	81.5	71.5
	4 ⁺	0 ⁺	E4	227.1(4) $\times 10^3$	-	1.2	153 $\times 10^3$	154 $\times 10^3$	149 $\times 10^3$
	3 ⁻	2 ⁺	E1	> 284	1.64	0.35	-	0.31	0.83
	4 ⁺	3 ⁻	E1	4.45(55)	"	"	-	0.055	0.12
	4 ⁻	4 ⁺	E1	4.85(48)	"	"	-	0.19	0.23
	5 ⁻	6 ⁺	E1	4.90(53)	"	"	-	25.3	26.4
	5 ⁻	4 ⁺	E1	140(15)	"	"	-	113.8	120.1
	7 ⁺	8 ⁺	M1	0.042(5)		$0.7g_n^s$	0.019	0.034	0.033
	7 ⁺	6 ⁺	M1	0.066(7)		$0.7g_n^s$	0.029	0.046	0.045
	5 ⁻	4 ⁻	M1	0.123(14)		$0.7g_n^s$	0.028	0.023	0.020
^{131}Sn									
	19/2 ⁻	17/2 ⁺	E1	> 333	1.64	0.35	-	0.25	0.40
	23/2 ⁻	19/2 ⁻	E2	14.7 (10)	-	1.2	9.39	9.55	9.13
	19/2 ⁻	11/2 ⁻	E4	> 1.891 $\times 10^6$	-	1.2	1.059 $\times 10^5$	1.069 $\times 10^5$	1.030 $\times 10^5$
^{133}Sb									
	21/2 ⁺	17/2 ⁺	E2	~ 10.48	2.0	0.0	4.86	4.86	-
	15/2 ⁺	13/2 ⁺	M1	> 0.43	$0.7g_p^s$ and $0.7g_n^s$		0.25	0.23	-
	13/2 ⁺	11/2 ⁺	M1	0.0075 (27)	"		0.65	0.67	-
^{134}Te									
	12 ⁺	10 ⁺	E2	133 (12)	2.0	0.0	36.8	41.1	-

dimension of Hamiltonian matrices. The difficulty increases while working with this new interaction in the expanded model space. Thus, suitable truncations schemes have been adopted. Since, the $\nu 1h_{9/2}$ orbital is at relatively higher energy, no neutron is allowed to be excited to this orbital. The truncation schemes adopted are:

- for $^{118-126}\text{Sn}$, $\nu 1g_{7/2}$ and $\nu 2d_{5/2}$ orbits are totally filled up and rest of the neutrons are free to access any one of the $\nu 2d_{3/2}$, $\nu 3s_{1/2}$, $\nu 1h_{11/2}$ orbits, only one particle is allowed to be excited to orbits beyond N=82, i.e., $\nu 2f_{7/2}$ and $\nu 3p_{3/2}$ orbits, and
- for ^{128}Sn , only $\nu 1g_{7/2}$ orbit is fully occupied and the rest is same as above,
- there is no restriction in N < 82 orbits and maximum one neutron excitation is allowed to each orbit in case of ^{130}Sn .

6.7 Results and Discussion - II

Because of these severe truncations, the calculated excitation energies do not match well with the experimental data for these isotopes.

The $B(E1:5_1^- \rightarrow 4_1^+)$ values have been calculated with effective charges ($e_p^{eff} = 1.64e$, $e_n^{eff} = 0.35e$) for $^{118-126}\text{Sn}$ (Table 6.5). Near the N=82 shell closure, for $^{128,130}\text{Sn}$, where minimum truncation in the model space was opted for calculation, the B(E1) values ($e_p^{eff} = 1.35e$, $e_n^{eff} = 0.35e$) match well with the reported data. Maximum deviation is observed for ^{126}Sn . The deviations are

Table 6.5: Details of E1 transitions ($5^-_1 \rightarrow 4^+_1$) in even $^{118-130}\text{Sn}$ isotopes. The B(E1) values are extracted from experimental half-lives [18] of 5^- states after incorporating the corrections for branching ratios and conversion coefficients, wherever needed. The B(E1) values are quoted in the unit of $10^{-5} e^2\text{fm}^2$. Theoretical transition probabilities are calculated with $e_p^{eff} = 1.64e$ and $e_n^{eff} = 0.35e$, unless mentioned otherwise.

A	Transition energy $5^-_1 \rightarrow 4^+_1$ (keV)	$T_{1/2}$ ns	B(E1)	
			Expt.	Theory
118	40.8 (1)	21.7 (2) 19.6 (10) ¹	8.84 (109)	0.04345
			9.10 (465)	
120	89.87(16)	5.55 (3)	8.63 (78)	0.03781
122	103.74 (1)	7.9 (9)	4.12 (63)	0.01102
124	102.91 (2)	270 (6)	0.0705 (17)	0.001753
126	111.79 (5)	10.8 (7)	2.54 (37)	0.00001758
128	120.54 (5)	8.6 (8)	2.62 (24)	0.3569 ²
130	89.23 (3)	52 (3)	0.595 (82)	0.4377 ²

¹ Present work, ² $e_p^{eff} = 1.35e$ & $e_n^{eff} = 0.35e$

in 2-3 orders of magnitude. This deviation possibly arises due to the severe truncations adopted in the calculations.

CHAPTER 7

Summary and future outlook

In this present thesis, extensive experimental as well as theoretical studies of Sn isotopes have been accomplished. The low-lying structures of mid-shell Sn isotopes ($^{117,118}\text{Sn}$) have been studied from off-line decay spectroscopy experiment. These nuclei are populated in irradiation experiment performed at Variable Energy Cyclotron Center (VECC). The main populated nuclei are $^{117g,118m}\text{Sb}$, ^{117m}Sn . The data have been acquired using conventional analog electronics as well as utilizing digital techniques. We have remeasured the decay half-lives of parent nuclei $^{117g,118m}\text{Sb}$, that decay to $^{117,118}\text{Sn}$. The values extracted with the help of both techniques are in well agreement with previous literature values [18]. Some of the ambiguities present in the placement of some transitions in the excitation spectra of ^{118}Sn have been resolved in this current work. Moreover, the level scheme of ^{118}Sn has been modified by eliminating a γ -ray (984 keV) that was previously assigned to ^{118}Sn . Using two different experimental setups, we have attempted to remeasure the level lifetime of $3/2_1^+$ state of ^{117}Sn .

Moreover, the decay half-lives of parent nuclei $^{117g,118m}\text{Sb}$ are also measured from the digital data. In this part of work, the list mode data of digitiser have been employed to evaluate decay half-lives of different nuclei ranging from few min to several hrs using a novel technique. In this current technique, spectra have been generated after a constant number of decay events instead of an equal time interval. As a consequence, good statistics is maintained even at the end of the decay that induces less statistical error. Two different experiments (an off-line experiment and an in-beam experiment) have been performed at VECC.Kolkata to test the effectiveness of the present technique. It is observed that, the applied method is quite successful to estimate the half-life and the obtained values match with previous experimental results. Even, we can provide minute details of different beam parameters from these digital data. In future, we would like to apply this technique to determine half-lives ranging in the order of ns, which is not perused in this work.

In the part of developmental activities, we have attempted to study the coincidence relation between X-rays and internal conversion electron using cost effective photodiodes or PIN diodes. To start with, we have tested different photodiodes and PIN diodes (BPW34, BPW21, VTB8440BH, BEL PIN diode) with alpha-emitting radioactive sources. Among them, the best performance is achieved with the PIN diode procured from Bharat Electronics Limited (BEL). This particular diode is able to detect X-rays, conversion electron and low en-

ergy gamma-rays quite efficiently. Finally, a set up comprising of NaI(Tl) and BEL PIN diode is made to investigate the coincidence relation between X-rays and internal conversion electron. We are able to test this setup using commonly used radioactive source ^{152}Eu successfully. We have struggled to test the setup with long-lived isotope of Sn region prepared from irradiated foil. The strength of these source was very weak to detect conversion electron. Therefore, in future, we intend to overcome this difficulty and test the setup with such sources.

In the theoretical part, large basis shell model calculations have been performed in order to describe the experimental findings. This work has been started with the objective to reconstruct an effective nucleon-nucleon interaction, that will be able to explore all the physical issues encompassing over the whole isotopic chain. As a starting point of the work, existing interactions (sn100pn and Bonnnewpn) are used to figure out the strength and weakness of these interactions. Overall, sn100pn and Bonnnewpn are quite able to reproduce the experimental data for the nuclei near the shell closures ($^{100,132}\text{Sn}$).

By putting proper restrictions, using sn100pn interaction, the transition probabilities (mainly E2 transition probability) associated with different isomeric states present in $^{117,118}\text{Sn}$ isotopes are well reproduced. However, these standard interactions fail to describe E1 isomers because of the conventional model space specified. In this present work, we have expanded the neutron model space and reconstructed a new cross-shell interaction by recombining two commonly used interactions: sn100pn and CWG interactions. Some of the missing

TBMES have been calculated using zero range Delta interaction. Also, a few TBME are estimated empirically and tuned further to reproduce the low-lying multiplet states of ^{132}Sn . To check the applicability of this newly formed interaction, the excitation spectra as well as the transition probabilities are calculated for ^{132}Sn and its neighbouring nuclei. This is the first shell model study of ^{132}Sn energy spectra and transition probabilities within an extended space. This interaction is capable to account the low energy states as well as high energy states showing very good agreement with the available experimental data. Moreover, we also have calculated the transition rates associated with E1 transitions of $^{118-130}\text{Sn}$ systematically. In most of the cases, theoretically predicted $B(E1)$ values are underpredicted. It is an indication that we need to include other higher orbitals for correct reproduction of experimental values.

Summary

In this doctoral thesis, mainly the nuclear structure of Sn isotopes and their neighbours has been explored by means of experimental and theoretical investigation. In the experimental part, we have performed two irradiation experiments at Variable Energy Cyclotron Centre (VECC), Kolkata to pursue decay spectroscopy of $^{117g,118m}\text{Sb}$ and ^{117m}Sn . The experimental data have been accumulated utilizing two different experimental setups employing analog and digital techniques. In the current work, we have resolved some of the ambiguities present in the adopted level scheme of ^{118}Sn . The level lifetimes of some of the yrast states of $^{117,118}\text{Sn}$ are also remeasured using the slope and deconvolution methods. The digital data as well as analog singles data have been considered to extract the decay half-lives of parent nuclei, $^{117g,118m}\text{Sb}$. During the estimation of half-life from digital data, a different technique has been considered to evaluate lifetime ranging from a few min to several hrs. Moreover, these digital data are able to provide minute details of different beam parameters. In the part of developmental activities, we have tested cost effective rugged photodiodes and PIN diodes with some standard radioactive sources. Among them, the best performance is achieved using the PIN diode procured

from Bharat Electronics Limited (BEL). This particular diode is able to detect X-rays, conversion electron and low energy gamma-rays quite efficiently.

In the theoretical part, large basis shell model calculations have been performed in order to describe the experimental findings. By putting proper restrictions, commonly available interactions are tested to estimate the excitation energies and transition probabilities associated with different isomeric states present in $^{117,118}\text{Sn}$. However, these standard interactions are unable to describe E1 isomers because of the conventional model space specified for these interactions. We have reconstructed a new multi-shell interaction to describe the cross-shell excitation by recombining two commonly used interaction: sn100pn and CWG interactions. Some of the missing two body matrix elements have been calculated using 'zero range Delta interaction'. Also, a few tbmes are estimated empirically and tuned further to reproduce experimental data. To check the applicability of this newly formed interaction, the excitation spectra as well as the transition probabilities are calculated for ^{132}Sn and its neighbouring nuclei. This is the first shell model study of ^{132}Sn in an extended space. This interaction is capable to account for the low energy states as well as high energy states showing very good agreement with the available experimental data. Moreover, we also have calculated the transition rates associated with E1 transitions of $^{118-130}\text{Sn}$ systematically.

APPENDIX A

Activation analysis

It is an analytical method in which the stable nuclei are made radioactive by the process of irradiation. In this process, both uncharged (neutron) and charged particles (such as proton, alpha particles) can be used as a projectile.

This kind of radioisotopes can be created using a reactor or cyclotron. There are several advantages of using accelerator to produce radioisotope over that produced via reactor [138]. One of the main reasons is that higher specific activity, that can be achieved in case of bombardment by proton and alpha particle. Also, it produces lesser amount of radioactive waste that is primarily generated from reactions associated with charged particles.

In case of charged particle activation process (depending on the type and energy of the bombarding particle), different radionuclide can be formed from a specific target isotope. In this process, in general, neutron-deficient isotopes are formed and these decay preferentially by the emission of β^+ particle or by the process of electron capture [139]. If we consider a situation, where a stable target (N_t) is bombarded by a projectile that produces a radioactive element (N_m : number of nuclei of present in target) (say, at a rate of M). At the same time, that radioactive product decays with a decay constant λ_m and produces stable nucleus (N_d : number of nuclei of present in daughter nucleus). So, the net activity during the irradiation will be balance between the rate of production of radionuclide and the spontaneous decay of it. The equation for

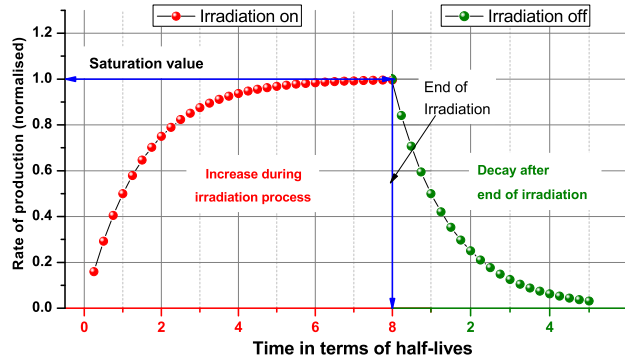


Figure A.1: Schematic figure of activity building and decaying of daughter nucleus during the irradiation and after the irradiation.

the rate of production of N_m over a small time dt can be written as,

$$\frac{dN_m}{dt} = M - \lambda_m N_m. \quad (\text{A.1})$$

In general, the rate of production of radioactive nuclide is priorly dependent on some important factors like, reaction cross-section as a function of energy (σ), thickness of the target or number of atoms present in target (N_t), flux of incident projectile (ϕ). The production rate can be expressed as,

$$M = N_t \sigma \phi. \quad (\text{A.2})$$

So the equation A.1 turns out to be,

$$\begin{aligned} \frac{dN_m}{dt} &= N_t \sigma \phi - \lambda_m N_m \\ \text{or, } N_m(t) &= \frac{N_t \sigma \phi}{\lambda_m} (1 - e^{-\lambda_m t}). \end{aligned} \quad (\text{A.3})$$

As, the equation A.3 contains a saturation term $(1 - e^{-\lambda_m t})$, the production rate is also influenced by the radioactive decay of resultant nuclide. If the half-life is short, then after a long irradiation time, the activity build up will reach a saturation limit. For irradiation time equals to two times of half-life, the activity would be 3/4 of the maximum activity and for three times of half life it would be 7/8 of the maximum activity. So, in general, the irradiation time is not kept longer than 2 -3 half-life periods [140].

APPENDIX B

Gamma decay and Internal conversion

B.1 Gamma decay

The electromagnetic transition rate is an important parameter that gives structural information. The transition probability or the transition rate is given by,

$$T_{fi}(\sigma L) = \frac{l}{\tau} = \frac{8\pi(L+1)}{\hbar L[(2L+1)!!]^2} \left(\frac{E_\gamma}{\hbar c}\right)^{2L+1} B(\sigma L : I_i \rightarrow I_f), \quad (\text{B.1})$$

where, $B(\sigma L)$ is known as the reduced transition probability with multipolarity σ .

$$B(\sigma L : I_i \rightarrow I_f) = \frac{1}{2I_i + 1} | \langle I_f || O(\sigma L) || I_i \rangle |^2, \quad (\text{B.2})$$

where $O(\sigma, L)$ represents the multipole operator. Here, double bar ($||$) represents the reduced matrix element. For a reverse transition (such as in coulomb excitation) ($I_f \rightarrow I_i$), we can write

$$B(\sigma L : I_f \rightarrow I_i) = \frac{2I_i + 1}{2I_f + 1} B(\sigma L : I_i \rightarrow I_f). \quad (\text{B.3})$$

Experimentally, one can measure the lifetime τ of the level. Now, considering the branching ratio as well as the internal conversion correction, the partial lifetime of a particular gamma transition can be compared with τ by the relation.

$$\tau_\gamma = \tau \frac{1 + \alpha}{B.R.}, \quad (\text{B.4})$$

where, $B.R.$ is the branching ratio for that particular γ -transition and α is the

Table B.1: The total transition rate of electric and magnetic type of transition. T is expressed in sec^{-1} and E_γ is in MeV. B (EL) and B (ML) are in the units of e^2fm^{2L} and $\mu_n^2\text{fm}^{2L-2}$ [141].

Electric	Magnetic
$T(E1) = 1.59 \times 10^{15} E_\gamma^3 B(E1)$	$T(M1) = 1.76 \times 10^{13} E_\gamma^3 B(M1)$
$T(E2) = 1.22 \times 10^9 E_\gamma^5 B(E2)$	$T(M2) = 1.35 \times 10^7 E_\gamma^5 B(M2)$
$T(E3) = 5.67 \times 10^2 E_\gamma^7 B(E3)$	$T(M3) = 6.28 \times 10^0 E_\gamma^7 B(M3)$
$T(E4) = 1.69 \times 10^{-4} E_\gamma^9 B(E4)$	$T(M4) = 1.87 \times 10^{-6} E_\gamma^9 B(M4)$

internal conversion coefficient. Now the total transition rate is reciprocal of the level life-time. The transition rates associated with electric and magnetic type are given in the table B.1.

- In general, an excited nuclear state may have more than one decay branch. Therefore, the total decay constant λ_{total} Or T_{total} must be sum of all decay constants or transition rates.
- Generally, for a given type of transition lowest permitted multipole more dominant.
- For a single branch decay, more than one kind of multipole radiations can be observed. In order to conserve parity selection rule, the competitive transitions must be $E(L+1)$, ML or $M(L+1)$, EL . In such cases, one can find the mixing ratio δ^2 . For mixed $E2 + M1$ transition or for $M2 + E1$ transition, the mixing ratio δ^2 can defined as

$$\begin{aligned} \delta^2(E2/M1) &= \frac{T(E2)}{T(M1)}, \\ \delta^2(M2/E1) &= \frac{T(M2)}{T(E1)}. \end{aligned} \tag{B.5}$$

- In general, for a fixed multipole, the transition rate or probability is more for electric transition than the magnetic one, in case of medium and heavy nuclei.

B.2 Internal conversion

Internal conversion is a deexcitation mode, which is complementary to gamma transition. It arises due to electromagnetic interaction. In this process, the de-

excitation energy is transmitted to an extranuclear electron and that particular electron is ejected from the atomic orbital. The kinetic energy of the ejected electron is given by,

$$T_{elec} = E_{\gamma} - B, \quad (\text{B.6})$$

where, E_{γ} is the transition energy and B is the binding energy of the orbital shell from which the electron is emitted.

In case of electromagnetic decay with a transition less than 1.022 MeV, gamma ray emission and internal conversion compete with each other. The ratio of transition probability of internal conversion to γ -ray emission is termed as internal conversion coefficient (ICC) denoted by α .

Let us assume that, λ_e and λ_{γ} be the transition probability of internal conversion and gamma ray emission respectively. Then, the total transition probability λ_t is defined as,

$$\lambda_t = \lambda_e + \lambda_{\gamma} = \lambda_{\gamma}(1 + \alpha), \quad (\text{B.7})$$

where ICC is defined as ,

$$\alpha = \frac{\lambda_e}{\lambda_{\gamma}} \quad (\text{B.8})$$

The total ICC (α) is the sum of conversion coefficients related to all sub shells.

$$\alpha = \alpha_K + \alpha_L + \alpha_M + \dots \quad (\text{B.9})$$

Non-relativistically, the electric and magnetic multipole can be estimated as [142]

$$\begin{aligned} \alpha(EL) &\approx \frac{Z^3}{n^3} \left(\frac{L}{L+1} \right) \left(\frac{e^2}{4\pi\epsilon_0\hbar c} \right)^4 \left(\frac{2m_e c^2}{E_{\gamma}} \right)^{L+5/2}, \\ \alpha(ML) &\approx \frac{Z^3}{n^3} \left(\frac{e^2}{4\pi\epsilon_0\hbar c} \right)^4 \left(\frac{2m_e c^2}{E_{\gamma}} \right)^{L+3/2}. \end{aligned} \quad (\text{B.10})$$

Here, Z is the atomic number of that particular atom from which the electron is knocked out and n represents the quantum number (principal) of bound elec-

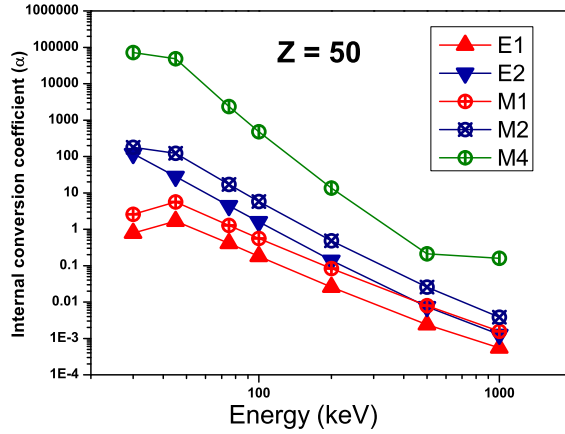


Figure B.1: The internal conversion coefficient is plotted with increasing energy for Sn element. It is calculated theoretically using BRICC code [74].

tron. The multipolarity of the transition is denoted by L and m_e is the electron rest mass.

- From equation B.10, it is observed that α is proportional to Z^3 . Hence, for heavier nuclei the process is more significant.
- α is inversely proportional to E_γ . So, in case of lower transition energy it is more dominant.
- α is proportional to multipolarity. Therefore, for higher multipolarity transition the conversion coefficient is larger.

Hence, in general, it can be said that for low energy and higher multipolarity transitions of heavier nucleus, the process has greater importance. Theoretically, this ICC can be calculated using the available computer code "BRICC" [74].

APPENDIX C

Measurement of lifetime from time difference spectrum

Let us consider a nuclear excited state, which is populated by the gamma transition γ_2 and de-excited by emitting an transition of energy γ_1 (as shown in Fig. C.1). We want to measure the half-life of this excited state, τ . At first, time difference spectrum is obtained by projecting the total TAC by gating the feeding gamma γ_2 (say photo-peak P_2 region $P_{21}P_{22}$ here) in one detector and the decaying gamma γ_1 (say, photo-peak P_1 region $P_{11}P_{12}$). From the figure, we can observe that obtained time difference spectrum (say, T_1) contains the gating region the photo-peak as well as the contributions from the background. And, we want solely the contribution related to photo-peak. So, we need to eliminate the background part. Let us consider, B_1 (region $B_{11}B_{12}$) is the background region of photo-peak P_1 and B_2 (region $B_{21}B_{22}$) is of photo-peak P_2 . The background region is considered in the right of the photo peak to avoid the part coming from the Compton scattering.

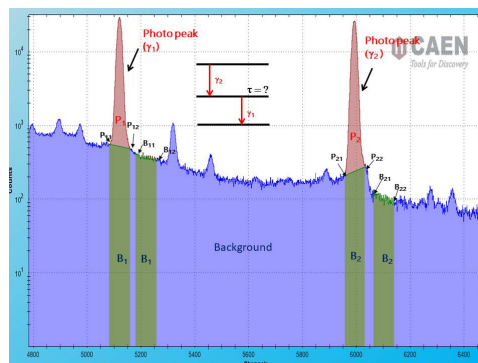


Figure C.1: A typical gamma ray spectrum indicating photopeaks and their neighbouring background.

Now,

$$(P_1 + B_1) * (P_2 + B_2) = P_1 * P_2 + P_1 * B_2 + P_2 * B_1 + B_1 * B_2. \quad (\text{C.1})$$

So, the first term of the equation C.1, will give the desired contribution. The equation C.1 can be re-written as,

$$P_1 * P_2 = (P_1 + B_1) * (P_2 + B_2) - [(P_1 + B_1) * B_2 + (P_2 + B_2) * B_1 - B_1 * B_2]. \quad (\text{C.2})$$

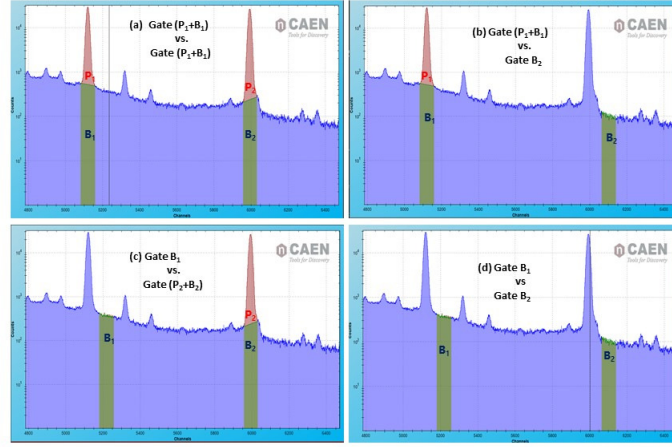


Figure C.2: These four spectra illustrate the regions in which the photo-peaks or their backgrounds are selected as gating region. The gating regions have been specified in each of the spectrum.

Therefore, we need to subtract the bracketed term from the T_1 spectrum. The first part of the bracketed term (say T_2) can be picked up by gating the $(P_1 + B_1)$ in one detector and B_2 in another detector. Similarly, applying the same procedure, second part (say T_3) of the bracketed term is calculated. The third term (say T_4) is obtained by projecting the tac spectra under the condition such that in one detector the background region of γ_1 and in another detector the background region of γ_2 is selected. So the resultant background corrected time difference spectrum (T_{total}) has been calculated using the relation,

$$T_{total} = T_1 - T_2 - T_3 + T_4 \quad (\text{C.3})$$

Applying the proper method depending upon the time resolution of the experimental setup, the level lifetime can be measured.

Bibliography

- [1] M. G. Mayer, Phys. Rev. **1948**, 74, 235-239 ; *ibid* **1949**, 75, 1969-1970.
- [2] O. Haxel, J. H. D. Jensen and H. E. Suess, Phys. Rev. **1949**, 75, 1766-1766.
- [3] R. Schneider *et al.*, Nucl. Phys. A **1995**, 588, c191-c196 ; Z Phys. A **1994**, 348, 241-242.
- [4] M. Lewitowicz *et al.*, Phys. Lett. B **1994**, 332, 20-24.
- [5] T. Faestermann, M. Gorska and H. Grawe, Prog. Part. Nucl. Phys. **2013**, 69, 85-130.
- [6] D. Seweryniak *et al.*, Phys. Rev. Lett. **2007**, 99, 022504, 1-4.
- [7] I. G. Darby *et al.*, Phys. Rev. Lett. **2010**, 105, 162502, 1-4.
- [8] C. Vaman *et al.*, Phys. Rev. Lett. **2007**, 99, 162501, 1-4.
- [9] P. Doornenbal *et al.*, Phys. Rev. C **2008**, 78, 031303(R) 1-5.
- [10] T. Togashi *et al.*, Phys. Rev. Lett. **2018**, 121, 062501, 1-6.
- [11] R. F. Casten, B. M. Sherrill, Prog. Part. and Nucl. Phys. **2000**, 45, S171-S233, and references therein.
- [12] S. Sarkar, M. Saha Sarkar, Phys. Rev. C **2010**, 81, 064328, 1-6.
- [13] M. Saha Sarkar, S. Sarkar, Pramana, J Phys. **2015**, 85, 403-413.
- [14] S. Sarkar *et al.*, J. Phys. Conf. Ser. **2011**, 267, 012040, 1-6.

- [15] H. H. Bolotin, A. C. Li, and A. Schwarzschild, Phys. Rev. **1961**, 124, 213-223.
- [16] O. Rahmouni, J. Phys. **1968**, 29, 550-562.
- [17] J. Hattula, E. Liukkonen, J. Kantele, Z. Phys. **1970**, 231, 203-215.
- [18] <http://www.nndc.bnl.gov>.
- [19] A. Jungclaus *et al.*, Phys. Lett. B **2011**, 695, 110-114.
- [20] S. Y. Wang *et al.*, Phys. Rev. C. **2010**, 81, 017301, 1-4.
- [21] A. Astier *et al.*, Phys. Rev. C. **2012**, 85, 054316, 1-19.
- [22] K. Ortner *et al.*, Phys. Rev. C. **2020**, 102, 024323, 1-11.
- [23] S. Das *et al.*, Proc. DAE-BRNS Symp. Nucl. Phys. **2017**, 62, 84-85.
- [24] "Study of Deuteron Induced Transfer Reactions on ^{27}Al " V. Srivastava, Ph.D. thesis, VECC, HBNI, **2008**. <http://hdl.handle.net/10603/289068>.
- [25] J. K. Tuli, Nuclear wallet cards, 8th ed. Brookhaven National Laboratory, USA (last accessed on 08-06-2019).
- [26] A. Gavron *et al.*, Phys. Rev. C **1980**, 21, 230-236.
- [27] <http://lise.nscl.msu.edu/pace4.html>.
- [28] P. T. Callaghan, M. Shott and N. J. Stone, Nucl. Phys. A **1974**, 221, 1-12.
- [29] E. Hagebo, J. Inorg. Nucl. Chem. **1967**, 29, 2515-2532.
- [30] T. Domingo *et al.*, Applied Radiation and Isotopes **2017**, 119, 101-104.
- [31] A. Chatterjee, K. Ramachandran, Proc. DAE-BRNS Symp. Nucl. Phys. (India) **2003**, 46B, 474-475.
- [32] R. Bhowmik, S. Muralithar, R.P. Singh, INGASORT, Proc. of DAE-BRNS Symp. on Nucl. Phys. (India) **2001**, 44B, 422-423.

- [33] K. E. G. Löbner, ed. W. D. Hamilton (North-Holland. New York) **1975** 173-236.
- [34] L. Boström, B. Olsen, W. Schneider and E. Matthias., Nucl. instr. and meth. **1966**, 44, 61-64.
- [35] A. Schwarzschild, Nucl. instr. and meth. **1963**, 21, 1-16.
- [36] K. L. Wang *et al.*, Phys. ReV. C **2016**, 94, 044316 1-4.
- [37] B. Olsen and L. Boström, Nucl. instr. and meth. **1966**, 44, 65-72.
- [38] P. John, Z. Phys. **1972**, 254, 142-147.
- [39] M. Schmorak *et al.*, Phys. Rev. **1963**, 130, 727-730.
- [40] F. Metzger *et al.*, J. Franklin Inst. **1960**, 270, 138-142.
- [41] S. K. Dey *et al.*, Proc. DAE-BRNS Symp. Nucl. Phys. **2015**, 60, 992-993.
- [42] H. Mach *et al.*, Nucl. Instrum. Methods. Phys. Res. A **1989**, 280, 49-72.
- [43] H. Engel, P. John, B. Reuse, Z. Naturforsch. A **1972**, 27, 1368-1369.
- [44] R. Burn, F. Rademarkers., Nucl. Instrum. Methods. Phys. Res. A **1997**, 389, 81-86.
- [45] S. S. Alam *et al.*, Nucl. Instr. and Meth. A **2017**, 874, 103-112.
- [46] B. A. Brown, A. Etchegoyen, N. S. Godwin, W. D. M. Rae, W. A. Richter, W. E. Ormand, E. K. Warburton, J. S. Winfield, L. Zhao and C. H. Zimmerman, MSU-NSCL report **2004**, 1289(unpublished).
- [47] B. A. Brown *et al.*, Phys. ReV. C **2005**, 71, 044317, 1-6.
- [48] X. Flécharde *et al.*, Phys. Rev C **2010**, 82, 027309, 1-4.
- [49] C. Fontbonne *et al.*, Phys. Rev. C **2017**, 96, 065501, 1-10.
- [50] V. T. Jordanov, G. F. Knoll *et al.*, Nucl. Instrum. Meth. A **1994**, 353, 261-264.

- [51] C. Tintori, WP2081 Digital Pulse Processing in Nuclear Physics, Rev. 2.1, (2011); UM2606 DT5780 Dual Digital MCA User Manual, Rev. 4.
- [52] P. Mutti, M. Jentschel *et al.*, Proc. of ICALEPCS 2011, Grenoble, France 2011, 935-938.
- [53] <https://www.caen.it/products/mc2analyzer/>
- [54] MATLAB and Statistics Toolbox Release 2015a, The MathWorks, Inc., Natick, Massachusetts, United States.
- [55] S. Das *et al.*, Proc. DAE-BRNS Symp. Nucl. Phys. (India) 2018, 63, 1144-1145.
- [56] SRIM-2012.03 <http://www.srim.org/>
- [57] C. E. Cox *et al.*, IEEE Nucl. Sci. Symp. Conf. Rec. (2011).
- [58] Data accessed from https://henke.lbl.gov/optical_constants/atten2.html
- [59] https://www.hamamatsu.com/resources/pdf/ssd/e10_handbook_for_high_energy.pdf
- [60] https://www.hamamatsu.com/resources/pdf/ssd/e09_handbook_xray_detectors.pdf
- [61] BPW34 Si PIN photodiode Data-sheet, available online from <https://www.vishay.com/docs/81521/bpw34.pdf> (accessed on 01-08-2020).
- [62] BPW21 Si PIN photodiode Data-sheet, available online from https://dammedia.osram.info/media/resource/hires/osram-dam-5984961/BPW%2021_EN.pdf (accessed on 01-08-2020).
- [63] VTB8440BH photodiode Data-sheet, available online from https://media.digikey.com/pdf/Data%20Sheets/Excelitas%20PDFs/VTB8440BH,_8441BH.pdf (accessed on 01-08-2020).

- [64] BEL Si-PIN diode, Data-sheet available through private communication.
- [65] "Radiation detection and measurements", G. F. Knoll, 3rd Edition, John Wiley & Sons. Inc. New York.
- [66] "Application circuit examples of Si photodiode", available online from http://educyclopedia.karadimov.info/library/si_pd_circuit_examples.pdf
- [67] E. Barberis *et al.*, Nucl. Instr. and Meth. A , **1993**, 326, 373-380.
- [68] <https://www.tec-microsystems.com/faq/thermoelectric-coolers-intro.html>
- [69] <https://peltiermodules.com/peltier.datasheet/TEC1-12706.pdf>
- [70] S. Das *et al.*, Proc. DAE-BRNS Symp. Nucl. Phys. (India) **2015**, 60, 978-979.
- [71] F. Camargo, Braz. J. Phys. **2004**, 34, 936-938.
- [72] S. Das *et al.*, Proc. DAE-BRNS Symp. Nucl. Phys. (India) **2015**, 60, 976-977.
- [73] P. N. Mukherjee *et al.*, Physica **1960**, 26, 179-190.
- [74] T. Kibédi ,Nucl. Instr. and Meth. A **2008**, 589, 202-229. <http://bricc.anu.edu.au/>
- [75] S. Das *et al.*, Proc. DAE-BRNS Symp. Nucl. Phys. (India) **2019**, 64, 988-989 .
- [76] T. S. Park, J. M. Lee, H. Y. Hwang, App. Rad. Isot. **2002**, 56, 275-280.
- [77] http://www.nucleide.org/DDEP_WG/Nuclides/Eu-152_tables.pdf
- [78] C. Qi, Phys. ReV. C **2012**, 86, 044323, 1-11. .

- [79] B.A. Brown, W.D. M. Rae, Nucl. Data sheets **2014**, 120, 115-118.
- [80] S. Das *et al.*, Proc. DAE-BRNS Symp. Nucl. Phys. (India) **2015**, 60, 108-109.
- [81] R. Machleidt, F. Sammarruca, and Y. Song, Phys. Rev. C **1996**, 53, R1483-R1487.
- [82] A. Holt *et al.*, Nucl. Phys. A **1997**, 618, 107-125.
- [83] C. Qi, Phys. Rev. C **2016**, 94, 034310, 1-6.
- [84] R. L. Lozeva *et al.*, Phys. Rev. C **2008**, 77, 064313, 1-15.
- [85] Ł. W. Iskra *et al.*, Phys. Rev. C **2014**, 89, 044324, 1-21.
- [86] Ł. W. Iskra *et al.*, Phys. Rev. C **2016**, 93, 014303, 1-20.
- [87] S. Pietri *et al.*, Phys. Rev. C **2011**, 83, 044328, 1-6.
- [88] R. Broda *et al.*, Phys. Lett. **1992**, 68, 1671-1674.
- [89] C. T. Zhang *et al.*, Phys. Rev. C **2000**, 62, 057305, 1-3.
- [90] S. Das *et al.*, Proc. DAE-BRNS Symp. Nucl. Phys. (India) **2016**, 61, 228-229.
- [91] J. M. Allmond *et al.*, Phys. Rev. C **2013**, 87, 054325, 1-7.
- [92] J. Blomqvist, Proc. of 4 th Int. Conf. on Nuclei far away from Stability, Denmark, **1981**, 536-541.
- [93] K. L. Jones *et al.*, Nature **2010**, 465, 454-457.
- [94] H. -K. Wang *et al.*, Phys. Rev. C **2017**, 96, 054313, 1-11.
- [95] S. Das, M. Saha Sarkar, Proc. DAE-BRNS Symp. Nucl. Phys. (India) **2019**, 64, 70-71.
- [96] "The Nuclear Shell Model", Kris L. G. Heyde Springer, Heidelberg, **1990**, 375.

- [97] "Structure of the Nucleus", M. A. Preston and R. K. Bhaduri, Addison-Wesley Publishing Company, U.S.A., **1975**.
- [98] P. Bhattacharyya *et al.*, Phys. Rev. Lett. **2001**, 87, 062502, 1-4.
- [99] G. Bocchi *et al.*, Phys. Lett. B **2016**, 760, 273-278.
- [100] O. Sorlin, M. -G. Porquet, Prog. Par. Nucl. Phys. **2008**, 61, 602-673.
- [101] G. Audi, W. Meng, Atomic Mass Evaluation 2013: Private Communication April **2011**.
- [102] D. H. Gloeckner and R. D. Lawson, Phys. Lett. B **1974**, 53, 313-318.
- [103] E. Caurier *et al.*, Rev. Mod. Phys. **2005**, 77, 427-488, and references therein.
- [104] G. Hagen, T. Papenbrock, D. J. Dean, Phys. Rev. Lett **2009**, 103, 062503, 1-4.
- [105] N. A. F. M. Poppelier and P. W. M. Glaudemans, Z. Phys. A - Atomic Nuclei **1988**, 329, 275-287.
- [106] S. Gartenhaus, C. Schwartz, Phys. Rev. **1957**, 108, 482-490.
- [107] B. Fogelberg *et al.*, Phys. Rev. Lett. **1994**, 73, 2413-2416.
- [108] S. Borg, G.B. Holm, B. Rydberg, Nucl. Phys. A **1973**, 212, 197-206.
- [109] K. Sistemich *et al.*, Z. Phys. A **1978**, 285, 305-313.
- [110] W. Urban *et al.*, Phys. Rev. C **2000**, 62, 027301, 1-4; *ibid* **2009**, 79, 037304, 1-4.
- [111] J. Blomqvist, A. Kerek, B. Fogelberg, Z. Phys. A **1983**, 314, 199-204.
- [112] J. Genevey *et al.*, Eur. Phys. J. A **2000**, 7, 463-465.
- [113] B. Sun *et al.*, Phys. Lett. B **2010**, 688, 294-297.

- [114] B. Fogelberg *et al.*, Phys. Rev. C **1990**, 41, R1890-R1894.
- [115] J. P. Omtvedt *et al.*, Phys. Rev. Lett. **1995**, 75, 3090-3093.
- [116] C. T. Zhang *et al.*, Phys. Rev. Lett. **1996**, 77, 3743-3746.
- [117] P. J. Daly *et al.*, Z. Phys. A **1997**, 358, 203-204.
- [118] S. K. Saha *et al.*, Phys. Rev. C **2001**, 65, 017302, 1-4.
- [119] M. Samri *et al.*, Z. Phys. A **1985**, 321, 255-263.
- [120] L. -E. De Geer, G. B. Holm, Phys. Rev. C **1980**, 22, 2163-2177.
- [121] B. Fogelberg, J. Blomqvist, Phys. Lett. B **1984**, 137, 20-22.
- [122] B. Fogelberg, J. Blomqvist, Nucl. Phys. A. **1984**, 429, 205-217.
- [123] B. Fogelberg *et al.*, Phys. Rev. C **2004**, 70, 034312, 1-7.
- [124] A. Kerek *et al.*, Nucl. Phys. A. **1972**, 195, 159-176.
- [125] C.A. Stone, S. H. Faller, W. B. Walters, Phys. Rev. C **1989**, 39, 1963-1971.
- [126] H. Mach *et al.*, Phys. Rev. C **1995**, 51, 500-508.
- [127] G. Audi *et al.*, Nucl. Phys. A. **2003**, 729, 3-128.
- [128] P. Bhattacharyya *et al.*, Phys. Rev. C **2001**, 64 054312, 1-4.
- [129] J. K. Hwang *et al.*, Phys. Rev. C. **2002**, 65, 034319, 1-4.
- [130] J. Shergur *et al.*, Phys. Rev. C. **2005**, 71 064321, 1-9.
- [131] B. Fornal *et al.*, Phys. Rev. C **2001**, 63, 024322, 1-6.
- [132] P. Hoff, B. Ekström, B. Fogelberg, Z. Phys. A. **1989**, 332, 407-411.
- [133] K. Kawade *et al.*, Z. Phys. A. **1980**, 298, 273-278.
- [134] P. Bhattacharyya *et al.*, Phys. Rev. C **1997**, 56 R2363-R2367.

- [135] Y. X. Luo *et al.*, Phys. Rev. C **2001**, 64, 054306, 1-4.
- [136] J. M. Eisenberg, W. Greiner, Nuclear Theory, Vol. 2, North-Holland Publishing Company, Amsterdam, New York, Oxford. 1976.
- [137] L. Kaya *et al.*, Phys. Rev. C **2019**, 100, 024323, 1-18
- [138] "Cyclotron produced Radionuclide : Principles and Practice", Technical reports number 465, International Atomic Energy Agency, Vienna **2008**.
- [139] H. Erramli, O. E. Bounagui, Encyclopedia of Analytical Chemistry, R.A. Meyers (Ed.)John Wiley & Sons, Ltd **2000** .
- [140] "Basic ideas and concepts in nuclear physics: an introductory approach (second edition)", K. Heyde, IOP publishing LTD **1999**.
- [141] "Emission of gamma radiation and nuclear structure(ch. 2)" in "The electromagnetic interaction in nuclear spectroscopy", K. Alder and R. M. Steffen, ed. W. D. Hamilton(North-Holland. New York) **1975**, 173-236.
- [142] "Introductory Nuclear Physics", K. S. Krane, John Wiley and Sons, New York, **1987**.
- [143] "Shell model applications in nuclear spectroscopy", P.J. Brussaard and P. W. M. Glaudemans, (North-Holland. New York) **1977**.
- [144] W. D. M. Rae, **2007**, unpublished, <http://knollhouse.org>.

Thesis Highlight

Name of the Student: **Sangeeta Das**

Name of the CI/OCC: **Saha Institute of Nuclear Physics** Enrolment No.: **PHYS05201504004**

Thesis Title: **Study of Nuclear Structure near Shell Closure**

Discipline: **Physical Sciences**

Sub-Area of Discipline: **Nuclear Structure**

Date of viva voce: **11-02-2021**

The doctoral thesis is based on the experimental and theoretical investigation of nuclear structure of Sn isotopes between two doubly magic nuclei ^{100}Sn and ^{132}Sn and their neighborhood. In the experimental part, two irradiation experiments have been performed at Variable Energy Cyclotron Centre (VECC), Kolkata to pursue decay spectroscopy of $^{117g;118m}\text{Sb}$ and ^{117m}Sn . The experimental data have been accumulated utilizing two different experimental setups employing analog (with Clover-Clover-LEPS detectors) and digital techniques (using single HPGe detector).

Some of the ambiguities present in the adopted level scheme of ^{118}Sn have been resolved. The half-life of $3/2^+$ state of ^{117}Sn (which is of ps order) has been measured using the setup of

VENTURE array at VECC. Additionally, the decay half-lives of parent nuclei, $^{117g;118m}\text{Sb}$ have been extracted from both analog and digital data.

During the estimation of half-life from digital data, a different technique has been considered to evaluate lifetime ranging from a few min to several hrs. Moreover, these digital data are able to provide minute details of different beam parameters. In the part of developmental activities, we have tested cost effective rugged photodiodes and PIN diodes with some standard radioactive sources. Among them, the best performance is achieved using the PIN diode procured from Bharat Electronics Limited (BEL). This particular diode is able to detect X-rays, conversion electron and low energy γ -rays.

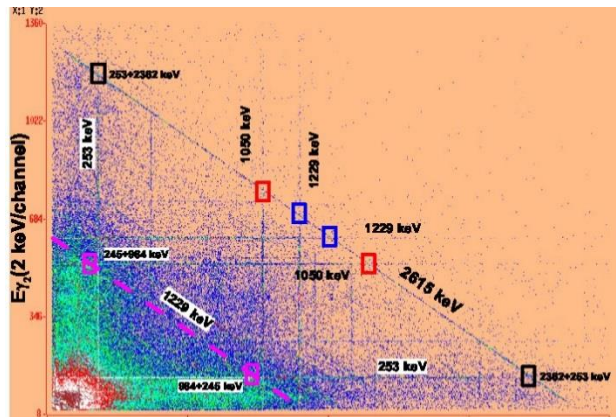


Figure 1. $E_{\gamma} - E_{\gamma}$ matrix obtained from two Clover data is shown. The Compton lines ($E_{\gamma 1} + E_{\gamma 2} = E_{\gamma}$) corresponding to $E = 1229 \text{ keV}$ and 2615 keV are shown. This correlation data is important to resolve uncertainties present in adopted data of ^{118}Sn .

In the theoretical part, large basis shell model calculations have been performed in order to interpret the experimental findings. By putting proper restrictions, commonly available interactions are tested to estimate the excitation energies and transition probabilities associated with different isomeric states present in $^{117;118}\text{Sn}$. A new multi-shell interaction is reconstructed to describe E1 isomers observed in this region by recombining two commonly used inter-actions: sn100pn and CWG interactions. This interaction is capable to account for the low energy states as well as high energy states showing very good agreement with the available experimental data. Moreover, we have calculated the transition rates associated with E1 transitions of $^{118-130}\text{Sn}$ systematically.